BEN-GURION UNIVERSITY OF THE NEGEV
FACULTY OF ENGINEERING SCIENCES
DEPARTMENT OF NUCLEAR ENGINEERING

Energy-resolved fast-neutron imaging via time resolved optical readout

THESIS SUBMITTED IN PARTIAL FULFILLMENT OF THE REQUIREMENTS FOR THE M.Sc DEGREE

By: Ilan Mor

Supervised by: Dr. David Vartsky, Soreq NRC, Yavne, Israel
and Dr. Itzik Orion, Ben-Gurion University, Beer-Sheva, Israel

Author's signature: …….. Date: ……..

Supervisors signatures: …… Date: ……..

…… Date: ……..

Signature of the chairperson of the education committee: ……. Date: ……

March, 2006

Abstract

Pulsed Fast Neutron Transmission Spectroscopy (PFNTS) is a radiography technique that exploits characteristic cross-section energy-variations for the purpose of element-specific imaging. In this method, a broad energy-spectrum fast-neutron beam (0.8-10 MeV) transmitted through an inspected object is modified according to cross-section fluctuations ("resonances") for light elements, such as C, N and O, present in it. Using the time-of-flight (TOF) technique, the spectrum of the transmitted neutrons is measured by a position-sensitive neutron detector and the attenuation at pre-selected time-intervals (neutron energies) is determined.

Consequently, PFNTS holds promise for detecting a broad range of conventional and improvised explosives.

Hitherto, the PFNTS detectors built by the University of Oregon and Tensor Technology operated in event-counting mode and defined a pixel size no better than ~10 cm^2. These limitations ruled out operation at high flux intensities and did not permit reliable detection of objects that are smaller than the pixel size.

The presently-described TRION system (Time Resolved Integrative Optical (readout for) Neutrons) is an efficient, large-area fast-neutron detector that incorporates the combined capabilities of sub-mm spatial imaging and Time-of-Flight spectrometry. It is also designed for loss-free operation in mixed, high-intensity neutron-gamma fields. Thus, it can be considered as a next-generation PFNTS detector, since it provides superior performance capabilities than previous detectors in all the important figures-of-merit.

The present work describes several rounds of development, construction and testing of the detector using accelerator-produced fast-neutron pulses (employing, among others, the $^{9}Be(d,n)$ reaction using a deuteron beam, pulsed in ~1 ns bursts at 1-2 MHz repetition rate).

The central topic of this work dealt with the determination of the factors that govern the spatial and timing resolution of TRION. Specifically, these are: screen type, response of the optical system and the various sources of noise that the system is susceptible to. Within this context, particular attention was focused on the following investigations:

a. A comparison between a fiber scintillating screen and plain scintillating slabs of different thicknesses was made, with respect to light output and *Contrast-Transfer Function* (*CTF*). In addition, TRION's spatial resolution dependence on neutron energy was simulated and measured.

b. The purely optical performance of TRION, excluding neutron influence, was measured and compared to its overall performance. The influence of the image intensifier (I-I) on TRION's *CTF* was isolated and systematically studied, as was the resulting behaviour of the variance/pixel, which was modeled and compared to measured values.

c. The temporal resolution (which defines the neutron energy resolution) directly affects the contrast ratio between "on-resonance" neutrons and "off-resonance" ones. As part of the experimental evaluation of TRION's TOF spectrometry, it was shown that the temporal resolution is limited by the minimal achievable I-I gate width and scintillation decay time. Despite the spatial resolution being somewhat degraded by the I-I and dominant noise sources such as *photon shot noise* and *I-I thermal noise*, excellent (sub-mm) spatial resolution was nevertheless obtained.

d. As a culminating experiment, element-specific radiography of several graphite rods was performed, resulting in a projected image of the carbon areal-density map, the quality of which was unprecedented with this technique.

In conclusion, the improvements that TRION has already demonstrated in spatial-resolution, element-specificity and count-rate capability (compared to the Oregon & Tensor PFNTS detectors), holds out the promise that this detector will eventually meet the appropriate performance characteristics required for security screening scenarios.

Acknowledgements

Many people have participated in this project. First and fore most, I would like to express my gratitude to my primary thesis advisor and head of this Soreq NRC project, Dr. David Vartsky. For his patient and open minded guidance throughout which made me an equal partner and left me scope to express my independence while making mistakes and learning from them. I have benefited immensely from his vast knowledge and expertise.
I also want to thank my secondary thesis advisor, Dr. Itzik Orion from the Ben-Gurion University, who was always available to help with any academic issues that arose on occasion and willingly shared his knowledge and expertise in Monte-Carlo simulations.

As an important member of this Soreq research group, Dr. Mark Goldberg contributed from his extensive knowledge and expertise during numerous discussions with David and myself at various stages of development and testing. I found those discussions most educative. In addition, this thesis would not be as eloquent and well structured as it is without Mark's assistance.

Image acquisition and data collection were controlled via a special computer program written by Doron Bar, who also wrote some useful MATLAB scripts for image processing. For these I am grateful. I would also like to acknowledge the contribution of Dr. Gennadi Feldman in the image processing field. His work transcends the scope of this thesis but is tightly bound to it and helped promoting our understanding of a variety of topics concerning our system.

Much of my knowledge in writing GEANT 3.21 simulations can be accounted to Dr. Israel Mardor, who made himself available to help with any question or problem and also ran several simulations that are referenced in this work.

The detailed engineering design of the system was done by David Katz with the supervision of Eli Sayag, from the drawing-board to the workshop at Soreq, with the active supervision and participation of Shaul Levy and many of the workers there.

Our lab technicians, Shaul Levy and Zion Vagish, found creative solutions for the continuous technical development of our system.

The large lens was specially designed by Dr. Oded Arnon, who was most cooperative in helping with various optical questions we encountered along the way. Its final assembly was done by Avi Meir.
The electronic wiring of the system was done with the kind assistance of Yair Cohen.

I would specially like to thank Dr. Volker Dangendorf (PTB, Germany), who was the first to suggest the idea on which this system is based. Volker is a key member of this project and is involved in all stages of the development. I have benefited greatly from his broad knowledge, experience and creative ideas. Volker has played a major role in the success of this project.
Moreover, Volker and his family gladly opened their home to me during our Braunschweig runs and made me feel a member of the household. His efforts on my behalf are immensely appreciated.
Many thanks are due to the PTB group headed by Volker. I want to thank the group members: Kai Tittelmeier, Mathias Weierganz, Wilfred Wendt, Gabor Laczko, Ronald Lauck and the accelerator team for their tremendous support and involvement in this project.

Last but not least, I would like to thank my dear wife Liat, who coped with a part time husband during these long months of writing. Liati, your support during this time was invaluable.

Table of contents

Table of figures

List of tables

Chapter 1

1.1 Fast neutron radiography

Fast neutron radiography (FNR) is a powerful method for non-destructive testing (NDT) due to the excellent matter-penetration characteristics of fast neutrons. A schematic drawing of a typical neutron radiography setup is shown in fig.1.1. A (point) neutron source can be either isotopic or accelerator-based. In several applications a parallel fast neutron beam from a reactor has been used. The neutrons are collimated toward the inspected object and the transmitted neutrons are detected by a position-sensitive neutron detector.

FNR is especially suitable for the inspection of items too thick or dense to be inspected by conventional thermal neutron or X-ray radiography. The main advantage of fast neutron radiography is that, except for hydrogen, it is not strongly dependent on the atomic number of the inspected material. Thus it is possible to observe details in hydrogenous materials beyond large thickness of heavier materials. In FNR the spectrum of the source neutrons can be either mono-energetic or a broad continuum. Inspection applications include: explosive devices [1], turbine blades, nuclear materials, electronic devices, aircraft components, composite armor laminates [2], fluid flow and other dynamic investigations [3, 4].

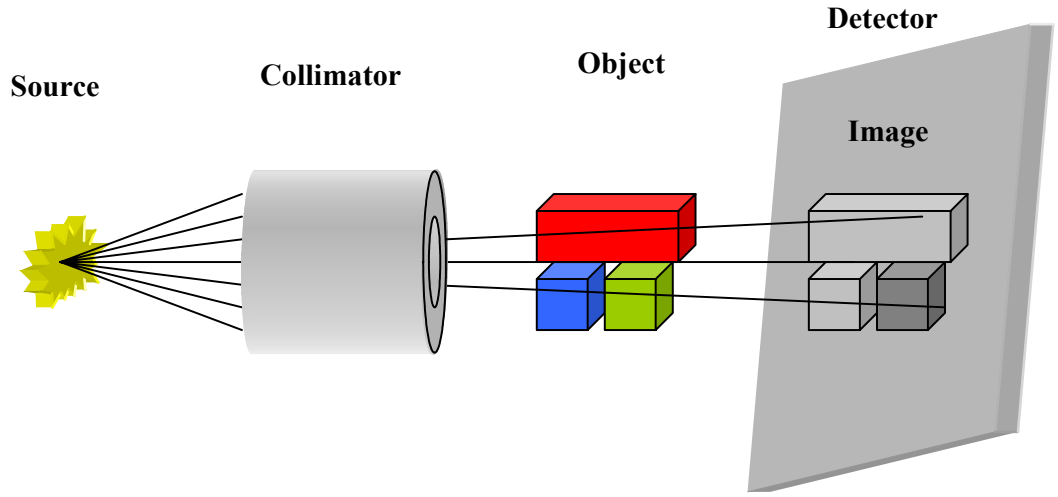

Fig. 1.1: Simplified radiography setup

A particular case for fast neutron radiography is resonant neutron radiography. Here the characteristic resonant structure of the fast-neutron cross-section energy-curves is exploited and has led to the development of an element-specific, fast neutron radiography and tomography method [5] - *Pulsed Fast-Neutron Transmission Spectroscopy* (*PFNTS*).

Proposed and first studied by Oregon University in 1985 [6-9] and subsequently refined by Tensor-Technology Inc. [10-12], PFNTS holds promise for detecting a broad range of conventional and improvised explosives, by determining the identity and density distribution of light elements such as C, N, and O within the inspected object. In this method a broad fast-neutron energy spectrum (0.8-10 MeV) transmitted through an object is modified according to the resonant features present in the cross-section of this element. Using the time-of-flight (TOF) technique, the spectrum of the transmitted neutrons is measured by a position-sensitive neutron detector and the attenuation at particular neutron energies that correspond to the resonances of C, N, and O is measured [13-15].

In the above-mentioned systems a large two-dimensional matrix of individual plastic scintillation detectors, 4×4 cm^2 in dimensions have been used [16] for contraband detection. The spatial resolution and count rate capability achievable there could neither ensure reliable detection of sheet explosives nor short inspection times.

The aim of this work was to overcome these shortcomings and to develop and characterize a novel, large-area imaging detector for sub-mm spatial imaging and few-ns-timing of fast neutrons, capable of loss-free operation at very high neutron flux.

1.2 Neutron interaction with matter

When neutrons collide with atomic nuclei, a variety of energy-dependent nuclear reactions can occur. Generally, a distinction is made between scattering processes, in which a neutron makes an elastic or inelastic collision with a nucleus, and absorption processes, in which the neutron is assimilated into the nucleus, causing the emission of various secondary radiations. The interaction cross section is used for the quantitative characterization of neutron interactions.

Neutrons are usually divided into three groups according to their kinetic energy:

- Slow or thermal neutrons ($E < 0.04$ eV)
- epithermal neutrons (0.05 eV$<E<10$ eV)
- Fast neutrons ($E > 1$ keV)

The following reactions may occur [17]:

1.2.1 Indirect reactions or compound-nucleus reactions

The incident neutron merges with the target nucleus, forming a relatively long-lived ($\geq 10^{-17}$s) compound nucleus whose excitation energy equals the sum of the center-of-mass kinetic energy and the binding energy of the captured neutron.

The compound nucleus can decay in various ways:

- A neutron with the same energy as that of the same originally-captured neutron can be emitted. This process is called *compound elastic*[*] *scattering*. When the scattering occurs in the region where the cross-section exhibits a resonance behavior, this process is called *resonance scattering*.
- The excitation energy can be dissipated by emission of one or more γ-rays, thus the phenomenon is termed *radiative capture* or (n,γ) process. The resulting nucleus often decays via emission of a β particle. The probability for this reaction is high at thermal and low energies.
- When the excitation energy is sufficiently high, charged particles or two neutrons can be emitted as: (n,α), (n,p), (n,np), (n,2n).
- A neutron with kinetic energy smaller than that of the incident neutron can also be emitted. In this case, the nucleus remains in an excited state which subsequently decays by γ-emission (*inelastic scattering)*.

[*] In the neutron-nucleus center-of-mass system the energy of the neutron does not change, therefore this is an elastic collision

- Fission can also occur in the heaviest nuclei

1.2.2 Direct reactions

Theses are reactions that proceed directly, without the formation of a compound nucleus.

Direct elastic scattering – Elastic scattering without the formation of a compound nucleus. Direct elastic scattering is frequently identified with *potential scattering*, the deflection of the incident neutron by the nuclear potential, which represents the average of all interactions with other nucleons.

The Q-value of elastic scattering is zero because the total kinetic energy after the reaction is the same as it was before.

For all practical purposes the target nuclei are at rest, therefore the sum of the kinetic energies of the reaction products (recoil nucleus and scattered neutron) must be equal to the energy carried by the incident neutron. Fig. 1.2 shows the neutron interaction diagram in the center of mass and lab coordinate systems.

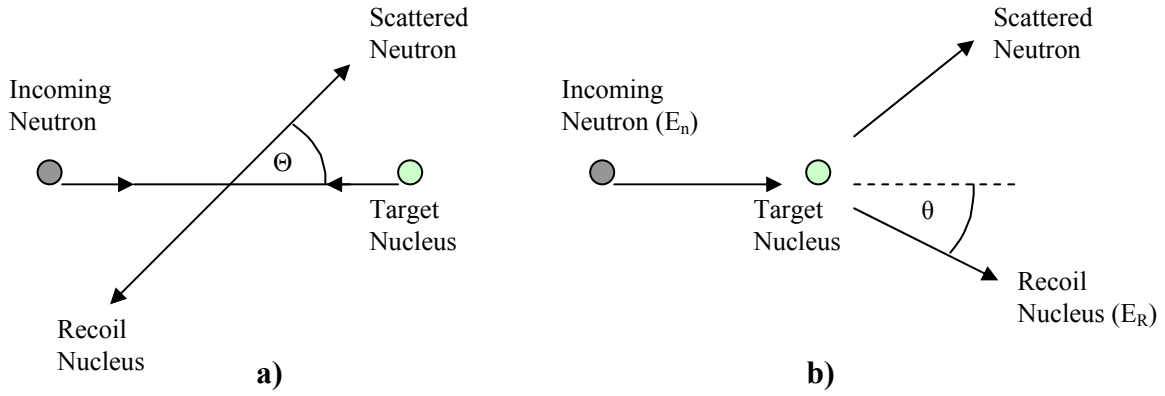

Fig. 1.2: Neutron elastic scattering diagrams for the a) center-of-mass and b) laboratory coordinate system

Conservation of momentum and energy in the center-of-mass coordinate system for incoming neutrons with non-relativistic kinetic energy (E_n) in the lab system (E_n<<931MeV), gives the following relationship for the energy of the recoil nucleus (E_R) in the lab system [17]:

$$E_R = \frac{2A}{(1+A)^2}(1-\cos\Theta)E_n \qquad [1\text{-}1]$$

Where A is the mass of the target nucleus/neutron mass, Θ is the scattering angle of the neutron in the center-of-mass coordinate system and θ is the scattering angle of the recoil nucleus in the lab coordinate system.

The following transformation is used in order to convert to the more convenient lab coordinate system in which the target nucleus is at rest:

$$\cos\theta = \sqrt{\frac{1-\cos\Theta}{2}} \qquad [1\text{-}2]$$

When combining eq.1-1 with eq.1-2, the following relationship for the recoil energy of the nucleus in terms of its own angle of recoil is obtained:

$$E_R = \frac{4A}{(1+A)^2}\left(\cos^2\theta\right)E_n \qquad [1\text{-}3]$$

From eq. 1-3 we can see that the energy imparted to the recoil nucleus is uniquely determined by the scattering angle. For a grazing angle encounter in which the neutron is deflected only slightly, the recoil nucleus is emitted almost perpendicular to the incoming neutron direction ($\theta \cong 90^o$), and eq. 1-3 predicts that the recoil energy will be close to zero. On the other hand, a head-on collision of the incoming neutron will lead to recoil in the same direction ($\theta \cong 0^o$), resulting in the maximum possible recoil energy:

$$E_R(max) = \frac{4A}{(1+A)^2}E_n \qquad [1\text{-}4]$$

While direct elastic scattering can always occur, compound nucleus formation is a resonance reaction, i.e., a compound nucleus can only be formed if the sum of the binding and kinetic energies of the incident neutron corresponds to an excited state of the compound nucleus.

The cross-section of the atomic nuclei is therefore composed of a cross-section for direct elastic scattering and a cross-section for compound nucleus reactions. Fig 1.3 shows the total cross section of carbon-12 which illustrates the above mentioned interactions.

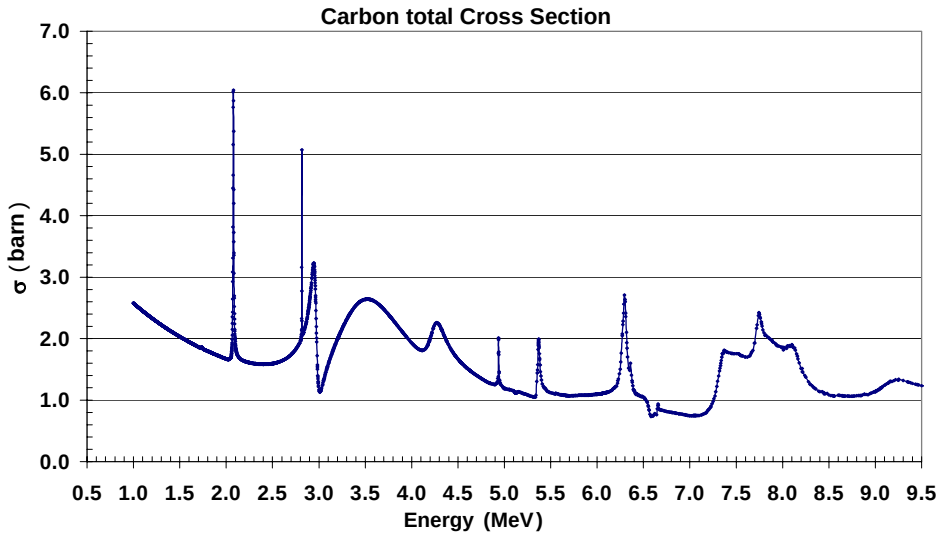

Fig. 1.3: Carbon 12 total cross-section [11]

1.3 Fast Neutron Detectors

1.3.1 Neutron detection

Neutrons are detected by their conversion to a charged particle, either in elastic collision or by a nuclear reaction. A common method of fast neutron detection is based on elastic scattering of neutrons by light nuclei [17]. As can be seen from eqs.1-1 to 1-4, the smaller the target mass A, the larger the energy that can be transferred to it by the incident neutron. For single scattering in hydrogen, the fraction of the incoming neutron energy transferred to the recoil proton can range anywhere between zero and the full neutron energy, so that the recoil proton has an average energy about half that of the original neutron. Hydrogen is therefore the most commonly-used target nucleus in detectors, while deuterium and helium can be used as well.

The detection efficiency of a device based on recoil protons or other recoil nuclei can be calculated from the scattering cross-section. If nuclei of only a single species (for example hydrogen gas) are present in the detector, the intrinsic efficiency is given simply by:

$$\varepsilon = 1 - e^{-N\sigma_s d} \qquad [1\text{-}5]$$

Where N is the number density of target nuclei, σ_s is the scattering cross-section for that nuclei and d is the thickness of the detector.

In most neutron detectors, carbon appears in combination with hydrogen and thus, competing effects due to carbon scattering must be taken into account. The counting efficiency, neglecting multiple scattering, is then given by:

$$\varepsilon = \frac{N_H \sigma_H}{N_H \sigma_H + N_C \sigma_C}\left[1 - exp\left(-\left(N_H \sigma_H + N_C \sigma_C\right)d\right)\right] \qquad [1\text{-}6]$$

Where the subscripts ***H*** and ***C*** refer to hydrogen and carbon relevant values.

Most neutron detectors employ either plastic or liquid scintillators that contain relatively large proportions of hydrogen. Fast neutrons incident on the scintillator give rise to recoil protons whose energy distribution ranges from zero to the full neutron energy. Due to the fact that the range of the recoil protons is usually small compared with the dimensions of the scintillator, their full energy is deposited in the scintillator.
For scintillators that are not small a possibility exists, that an incident neutron will be scattered more than once by hydrogen nuclei before escaping from the scintillator.
All organic scintillators contain carbon as well as hydrogen. The incident neutron can lose up to 29% of its initial energy in one carbon scattering.

Depending on the experimental requirements, a neutron detector may be used for determination of neutron energy (neutron spectroscopy), timing and spatial distribution (neutron imaging). The neutron detector for the PFNTS method (see chapter 2) requires all these features.

1.3.2 Neutron timing and spectroscopy by the time-of flight method

The most precise method for detection of neutron energy is the time-of-flight (TOF) method. This method [4] relies on the neutrons being generated in a short burst. After their emission, some of the neutrons will travel towards the detector with a velocity v_n, depending on their energy E_n:

$$v_n = c\sqrt{1 - \left(\frac{m_n c^2}{E_n}\right)^2} \qquad [1\text{-}7]$$

Where c equals the speed of light and m_n the neutron rest mass. For non-relativistic energies eq.1-7 can be written as:

$$v_n = \sqrt{\left(\frac{2E_n}{m_n}\right)} \qquad [1\text{-}8]$$

The time-of-flight is the time needed by the neutrons to cross the flight path x between source and detector:

$$TOF = \frac{x}{v_n} = x\sqrt{\frac{m_n}{2E_n}} \qquad [1\text{-}9]$$

The arrival time of these neutrons at the detector depends on their energy. Thus, by recording the neutron arrival time at the detector and knowledge of its creation time (time of accelerator burst) permits the determination of the neutron energy.

The energy resolution of this method depends on burst duration (1-2 ns, typically in cyclotrons), detector thickness, the distance between the source and detector and the resolving time of the electronics. Typical energy resolution obtainable with this method is 1-2% for few-MeV neutrons and a detector-source distance of 6-10 meters.

The TOF method permits good separation between γ-ray and neutrons emitted from the source. The γ-ray TOF is considerably shorter than that of the fastest neutrons considered in this energy range. In this manner, γ-ray background can be rejected, leading to pure neutron measurement.

In a typical event-counting TOF measurement, the measurement sequence is started by a pulse generated by the beam burst from an accelerator, which provides a “start” trigger to a Time-to-Amplitude Converter (TAC). The detection of a neutron by a detector provides a “stop” signal, which stops the measurement of time and the TAC generates a signal with an amplitude proportional to the time interval between “start” and “stop” pulses. Any additional “stop” pulse that will arrive for the same “start” pulse will be ignored. Thus in this mode of operation only one event can be counted for each burst. Actually, the “start” pulses are periodic and have much higher repetition rate than the “stop” detector pulses; hence, it is common to reverse the sources of the “start” and “stop” pulses. The neutron detector pulse is used to start the TAC, while the accelerator burst pulse is delayed and becomes a “stop” pulse. With this arrangement every useful “start” pulse is accompanied by a “stop” pulse and the TAC operates at much lower rate set by detected neutrons, with a consequence of negligible TAC dead time. The reversed start/stop scheme causes the reversal of the time spectrum, i.e., smaller TAC pulses will correspond to longer TOF’s.

If the probability of detecting more than one neutron event per beam burst is high, the TAC will give preference to faster neutrons, which arrive earlier and will tend to exclude neutrons which arrive later. Such bias toward faster neutrons will distort the energy spectrum. The distortion of the spectrum can be made negligible by lowering the neutron detection rate, such that the probability of detecting a single neutron is less than **0.01** per burst. This condition prevents the use of event counting TOF at high neutron counting rates.

The energy resolution of this method depends on burst duration (1-2 ns), detector thickness, the distance between the source and detector and the resolving time of the electronics. Typical energy resolution obtainable with this method is 1-2% for few MeV neutrons and detector-source distance of 6-10 meters.
The TOF method permits a good separation between γ-rays and neutrons emitted from the source. The γ-rays TOF is considerably shorter than the fastest neutrons considered in this energy range. In this manner, γ-rays background can be rejected leading to pure neutron measurement.

The main disadvantage of this method is that it requires an accelerator based neutron source capable of generating intense bursts of neutrons of short duration. Another disadvantage of this method is operation at relatively low neutron counting rate to assure detection of less than one neutron per burst.

1.3.3 Imaging fast neutron detectors

Neutron detectors used for fast neutron radiography are mostly based on the following configurations:

- Scintillating screens viewed by CCD
- Plastic scintillator slab viewed by CCD
- Scintillating fiber screens viewed by CCD
- Hydrogenous or metallic converter foils coupled to charged-particle detector

1.3.3.1 Scintillating screens

These screens are based on hydrogen-rich materials such as polypropylene loaded with ZnS(Ag) scintillator.

Neutron induced knock-on protons deposit their energy within the scintillator causing the emission of light, detected by a CCD camera via an appropriate optical configuration [18].
The minimum detectable neutron flux is determined by the optical geometry and the combined noises of the CCD and the image intensifier. Generally, a cooled CCD camera is used, but it is equally important to cool the image intensifier as well.

1.3.3.2 Plastic scintillator slab viewed by CCD

A plastic scintillator slab coupled to a CCD camera [4,16,19-20] is a different version of the detector based on a scintillating screen. A 4cm thick slab provides relatively high efficiency at the expense of spatial resolution. In addition, such a slab is sensitive to γ-rays.

1.3.3.3 Scintillating fiber screen

A screen made of individual scintillating fibers bundled as one unit, is coupled to a CCD readout. Position resolution depends on fiber diameter and length. As the fiber diameter decreases, the spatial resolution increases; however, cross-talk increases as well and light transmission is reduced.
Fiber length determines neutron detection efficiency and penumbra effects. The minimal detectable neutron flux is determined by the optical geometry and CCD noise.

1.3.3.4 Converter foil

Neutrons interact with converter foils [21] via scattering reactions, causing the emission of charged particles which are detected by a charged-particle-detector.

- Hydrogenous converter foil detector:

Neutrons cause the emission of knock-on protons via elastic (n,p) scattering with the hydrogenous foil. The foil is coupled to a position-sensitive charged-particle detector (solid state or gas), used to detect the knock-on protons.
The spatial resolution of the detector is determined by the length of proton trajectories in the gas and by the resolution of the position – sensitive readout.

- Metallic converter foil detector:

A metallic foil is used for the conversion of neutrons to protons via the (n,p) reaction. The resulting protons are registered in a position sensitive detector.

The selection of a metallic foil having a certain energy threshold for the (n,p) reaction enables the rejection of scattered neutrons of energy below this threshold.
Detection efficiencies are low due to the fact that the foils are required to be thin enough for protons to emerge with significant energy and the (n,p) cross-sections for metallic foils are generally below 500 mb requiring the foils to be thin enough for protons to emerge with significant energy.

Table 1-1 compares characteristics of FNR detectors developed over the past decade.

Table 1-1: characteristics of contemporary FNR detectors

Property	Spatial Resolution FWHM [μm]	Efficiency per incident fast-n	Gamma sensitive	Timing (ns)	Detector area realized [cm^2]
Scint. Screen/CCD	250-2000	1% (2mm thick)	Yes	No	30x30 (limited by optics)
Plastic Slab Scint./CCD	2000-3000	20% (40mm thick)	Yes	No	30×30
Scint. Fibers/CCD	500 (depending on fiber dimensions)	4-6% (100 mm long)	Yes	No	20×20
Metallic Converter/Gas Detector	400 (depending on readout)	0.2-0.6% (0.2-2mm thick)	No	10	12×12

The data summarized in table 1-1 leads to the conclusion that most contemporary fast-neutron imaging detectors suffer from low detection efficiency and lack of timing capability.
The *plastic slab scintillator* has relatively high detection efficiency but this advantage comes at the expense of spatial resolution, due to depth-of-field dependence. This loss of spatial resolution is avoided by the use of *scintillating fibers*, for which the spatial resolution is dependent only on the fiber dimensions and the knock-on proton range within the scintillating fiber matrix.
Additional factor to be considered when discussing scintillator-based detectors is the sensitivity to gamma rays. The metallic converter detector operates in a single-event counting mode and is therefore capable of providing information on neutron energy by measuring its time-of-flight. Although insensitive to gamma-rays, its detection efficiency is extremely low.

Recently, Ambrosi et. al. [22-24] proposed a direct fast neutron detection method using a microchannel plate (MCP) with large area a-Si pixel array readout. In this manner, the light conversion step, characteristic of most scintillator-based fast neutron imaging methods, is eliminated.
The MCP acts as both a converter and an intensifier, where the silicon in the plate is used to convert fast neutrons to protons, α -particles or deuterons via the $^{28}Si(n,p)^{28}Al$ and ^{28}Si

$(n,\alpha)^{25}Mg$ neutron capture reactions. The MCP is placed under a potential, thus ionizing particles (produced by the nuclear reactions described above) generate electrons at the channel-wall. These electrons are multiplied by an avalanche process which is read out by the a-Si pixel array underneath (see Fig. 1.4a). The direct and lightless conversion method removes the effect of light spreading in conventional converters and the 5MeV threshold in the conversion reactions (see Fig. 1.4b) reduces scattered neutrons affect on image contrast and resolution.

Fig. 1.5 shows neutron detection efficiency for Si based converters containing various concentrations of Si compared to Hydrogen rich converters [23]. According to fig. 1.5, the detection efficiency of a 10mm thick MCP is about 2%. This efficiency calculation does not take into account the open fraction of the detector, in other words the channels.

Image resolution is expected to be of the order of the channel diameter.

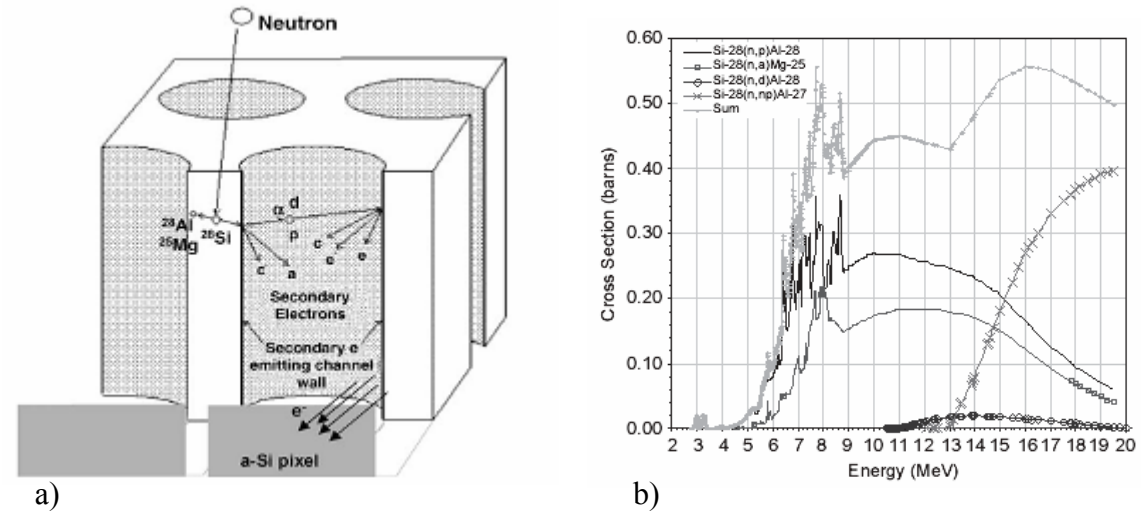

Fig. 1.4: Schematic description of neutrons interacting with the Si in the MCP. These neutrons undergo capture reactions, producing ionizing particles. These particles can generate electrons in the channel wall, which are consequently multiplied by an avalanche process in the MCP. The a-Si pixels detect the electrons to produce an image [23]

Amorphous silicon (a-Si) large area detector offers an attractive alternative to CCDs [22]. Higher photon detection efficiency results from direct one to-one coupling of the converter screen to the sensitive detector area without the need for additional optics; however the readout noise (~800 to ~4000 electron rms) of a-Si panels limit the detectability of small objects [22].

The detector design shown in fig. 1.6a and b [23] facilitates the production of a multi-layer detector, where each segment consist of a 40% Si MCP, 10mm thick and an area of $150mm^2$.

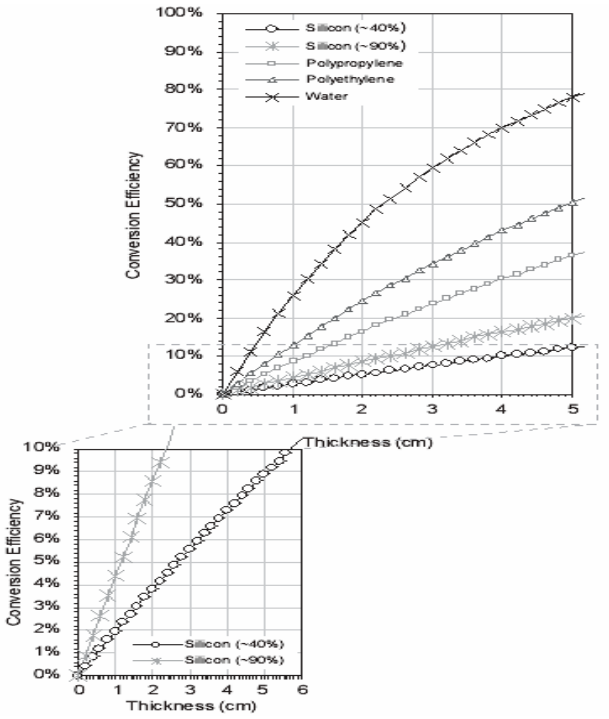

Fig. 1.5: Neutron detection efficiency for Si based converters containing various concentrations of Si compared to Hydrogen rich converters [23]

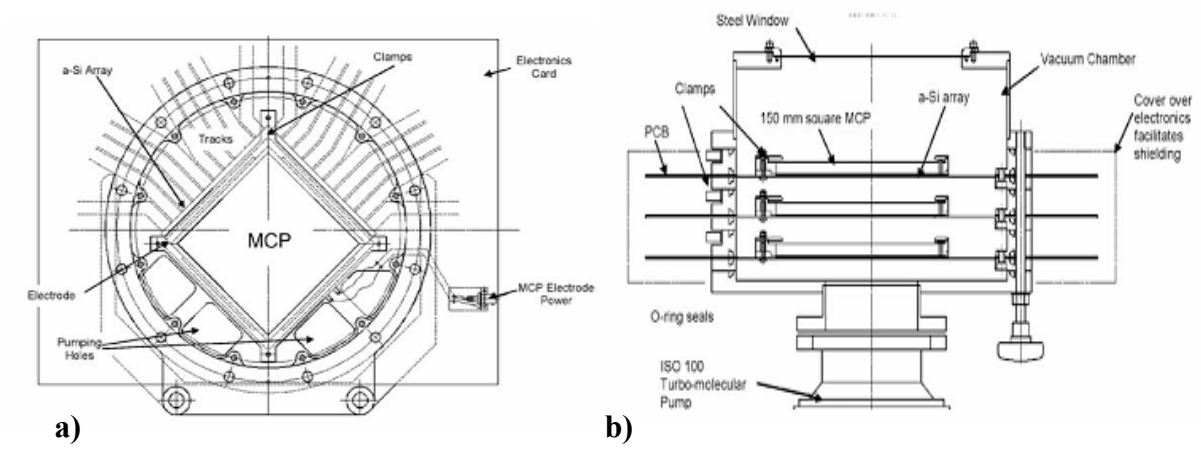

Fig. 1.6: a) A sectional top view of through the multi-layer detector architecture b) Side view of the layered detector [23]

Summary of the MCP a-Si approach:

a. Enhanced image resolution resulting from the energy discrimination properties of the detector and the lightless conversion process. Resolution values of the order of $\geq$ 200μm are potentially achievable
b. Relatively high detection efficiency when arranged in a multi-layer structure. Detection efficiency of 9% is expected for a 5 layer structure.
c. More radiation tolerant than CCD based systems

1.4 Accelerator based fast neutron sources

Fast neutron sources can be obtained by using accelerator driven systems utilizing (p,n), (α,n) or (d,n) reactions [4]. In such reactions, excited compound nuclei are formed. The excitation level equals the sum of binding energy and the kinetic energy of the projectiles. If the excitation energy is larger than the binding energy of a neutron in the compound nucleus, then a neutron is likely to be emitted, since there is no Coulomb barrier to be overcome.

Examples of common neutron producing reactions (with their Q values) are shown below:

1) **D(d, n)^{3}He+3.28 MeV**
2) **T(d, n)^{4}He+17.6 MeV**
3) **^{9}Be(d, n)^{10}B+4.4 MeV**
4) **^{7}Li(p, n)^{7}Be-1.65 MeV**
5) **^{9}Be(p, n)^{9}B-1.85 MeV**

Because of the small binding energy of the deuteron (a very highly excited compound nucleus is formed by its capture), consequently, nearly all (d,n) reactions are exothermic (positive Q value). Relatively high monoenergetic neutron yield can be obtained with deuteron energies as low as 100 to 200 keV in these reactions.

The neutron yield is a function of the cross-section for the reaction, density of target atoms and target thickness. For a thin target in which the incident particle does not change its initial energy significantly, the neutron yield per incident particle current is:

$$Q_{thin} = N\sigma dx \qquad [1\text{-}10]$$

Where N is the density of target nuclei, σ is the cross-section for the neutron producing nuclear reaction, and dx is the target thickness. In a thick target the energy of the incident particle is rapidly degraded by coulomb interaction with electrons in the target substance. Consequently the cross-section for neutron production varies rapidly across the thickness of the target. The slowing down of charged particles in matter is characterized by energy dependent slowing down power-dE/dx. This function has been determined for most particles and target nuclei vs. particle energy. The yield for a thick target can be calculated as following:

$$Q_{thick} = N \int_0^{E_0} \frac{\sigma(E)}{dE/dx} dE \qquad [1\text{-}11]$$

Where E_0 is the incident particle energy.

The d-Be reaction may yield ~10^{10} n/(s·sr·μA) at deuteron energy of 13.54 [25]. The (p,n) reactions on stable nuclei are endothermic, thus there is an energy threshold for its production. The 4th reaction is very common for production of neutrons but it is disadvantageous due to the fact that a radioactive isotope of beryllium, ^{7}Be is produced (^{7}Be decays under electron capture to ^{7}Li with half life of 53.23 days).

The ^{9}Be(d, n)^{10}B reaction is of particular interest to this work, since it yields an intense, broad-energy neutron spectrum required for the PFNTS method. The spectrum of neutrons following bombardment of a thick Be target with deuterons is shown on Fig. 1.7 [26].

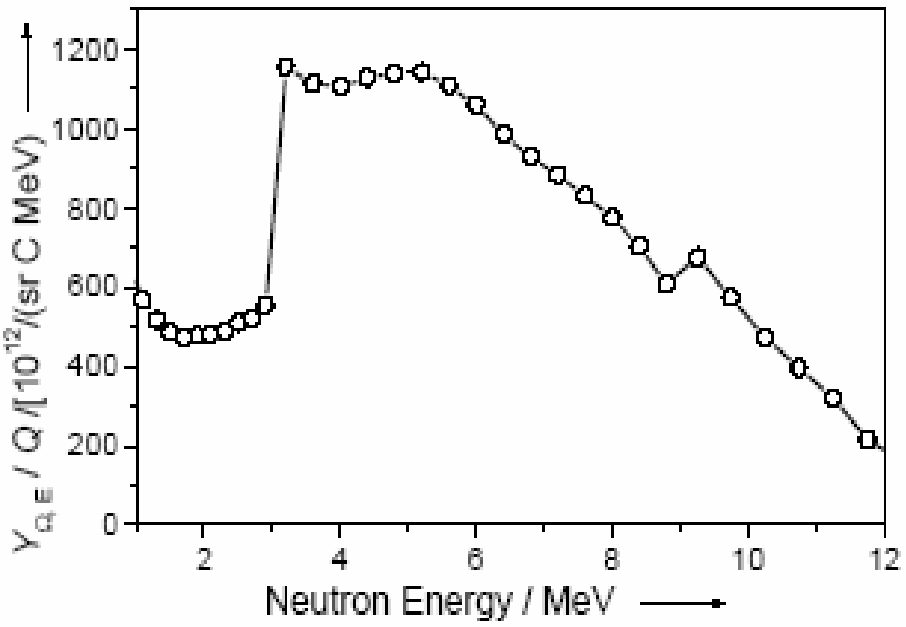

Fig. 1.7: Neutron yield [33] in the forward direction of 13 MeV deuterons incident on a thick Be target

Currently, available neutron sources suitable for PFNTS are linear-accelerators (linacs) or cyclotrons.

A novel neutron source [27-28], described schematically in fig. 1.9, is being developed by Tensor Technology and Lawrence Berkley laboratory. This is a pulsed neutron source based on the T+T reaction and presents a true technological breakthrough which should enable replacing the 25 ton particle accelerator subsystems.

The requirements from the source are high flux, small point-source, pulsed operation with short pulses and broad energy spectrum.

The broad energy spectrum is achieved by utilizing the T+T fusion reaction.

The overall cross-section is comparable to a D-D reaction except that the T-T reaction produces two neutrons per fusion. A typical energy distribution [27], shown in fig. 1.8, ranges from 0 to 9 MeV, which is suitable for the PFNTS screening method.

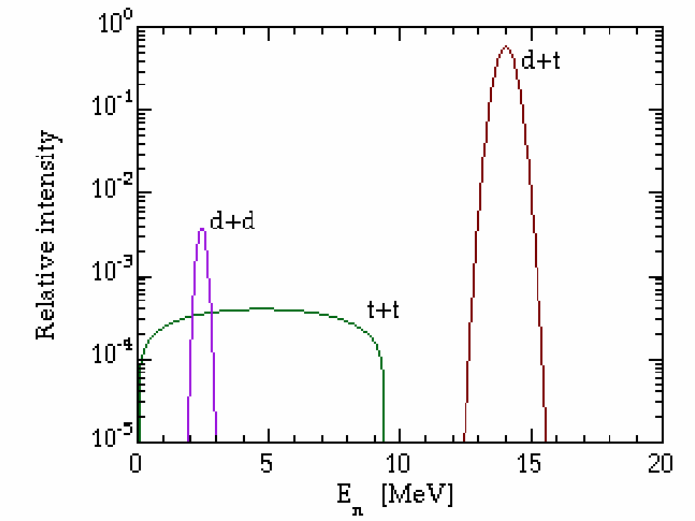

Fig. 1.8: Neutron spectra created by D-D, D-T and T-T reactions [31]

The short beam pulses are generated by sweeping the beam across a collimated aperture with parallel plate beam sweeper. Beam pulses that are 15ns wide have been generated in a very compact device. The requirement for the point source is to have pulse duration of 5ns at 0.25% duty cycle. The point neutron generator is designed to generate the plasma in a shaped plasma chamber and the beam is extracted toward the center of the generator, where it strikes a small-diameter Ti target rod. A hollow Ti rod is used, to permit water cooling. The plasma is produced by RF induction discharge which can provide high current density with atomic ion concentrations greater than 90%.

The point neutron generator uses 20 pulsed narrow beams (beamlets) to produce a current of 1A. This generates 10^{12} n/s time average yield during the pulse.

The ion source will be floating at +20 to +30kV potential, while the collimator/beam dump will be at ground potential to facilitate straightforward water-cooling arrangements. The target will be biased to -100kV. The discharge will be operated in pulsed mode with a 3 kW, 13.5 MHz RF generator. The RF antenna is a copper or aluminum coil wrapped around the plasma chamber as shown in the fig. 1.9 [27]. Since the antenna is located outside the plasma chamber, there is no limitation on its lifetime.

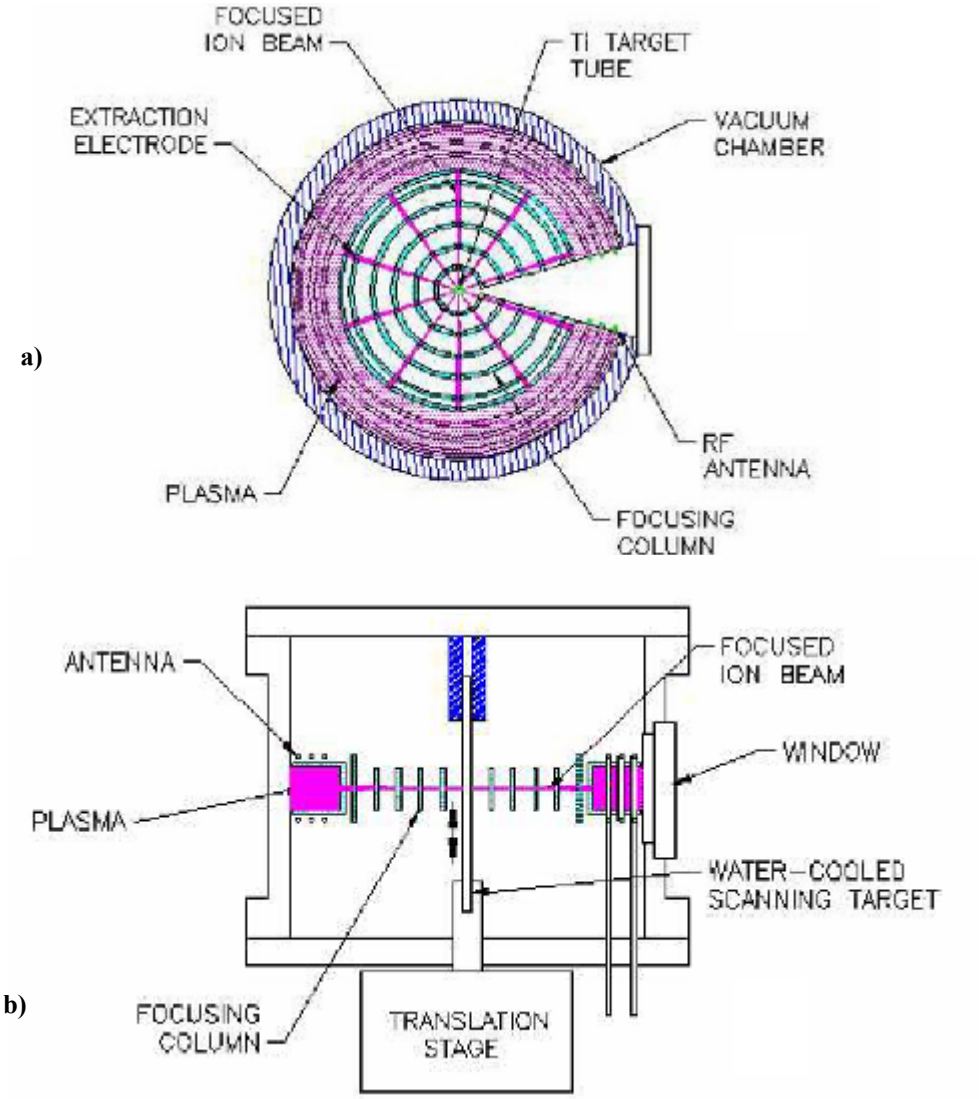

Fig. 1.9: a) Top view of point neutron source, and (b) Side view of point neutron source [31]

The ions of each beamlet (small beam) are accelerated to 100 kV and are focused down to a beam spot size of ~2-mm-diameter eventually uniformly irradiating the Ti target. The Tritium is implanted in the Ti target surface. When the incoming ions impinge on these atoms, neutrons will be generated via the T-T fusion process. The neutron yield builds up to a maximum after several minutes of bombardment.

The neutrons produced will appear to come from a small "point source" with diameter no larger than 2 mm.

The power density deposited by the focused ion beams on the target surface can be maintained at ~500 W/cm^2. This moderate heat load can be easily removed by using an oscillating water-cooled target stage. The entire neutron generator is about 20-cm diameter by 20-cm high.

Chapter 2

2.1 Review of fast neutron interrogation methods

Neutron and X-ray radiography reveal different aspects of the examined object. The low and medium-energy (hundreds of keV) x-ray attenuation coefficient [29] increases rapidly with elemental atomic number Z, whereas fast neutron attenuation exhibits only a relatively weak dependence on the atomic number Z. The result is that fast neutrons are highly penetrating and can be used for interrogation of relatively large objects such as medium-sized cargo containers. However, light materials such as hydrogen and deuterium have relatively high macroscopic attenuation cross-sections. Thus, penetration in objects containing hydrogenous materials will be rather limited.

The interrogation of an object with fast neutrons can be performed in a radiography mode, in which the fast neutron flux transmitted through the object is detected by an imaging detector. If the total cross-section for an element of interest has resonances, this feature can be used for its identification. Specifically, the well known resonances in the fast-neutron cross sections of C, O and N in the 1 - 8 MeV range can be used for detecting their presence and relative abundance.

Alternatively the incident fast neutrons can induce a nuclear reaction (neutron capture, inelastic scattering, fission) in the object leading to the emission of characteristic (prompt or delayed) gamma-rays which, in turn, are detected by gamma-ray detectors.

Neutron-based techniques for the non-destructive elemental characterization of materials in bulk have been commercially operational since the late 1970's, especially in the context of on-line analysis and control and in the minerals industry [30].

In the last twenty years there has been notable interest in the investigation of these techniques for non-destructive detection of explosives and illicit drugs. The following section reviews several fast neutron interrogation techniques for detection of explosives and illicit drugs concealed in small mail items, airline baggage and large cargo containers.

2.2 Thermal Neutron Activation analysis (TNA)

Thermal Neutron Activation analysis was one of the first techniques for detection of explosives in passenger bags that employed neutrons [31,32]. Fast neutrons emitted by a radioisotopic source such as ^{252}Cf or a sealed tube neutron generator (STNG), are moderated to low energies (< 0.025eV) within the investigated object. A fraction of these neutrons react with nuclei in the objects, producing prompt capture γ-rays, which are detected by the detector. The detection of explosives using TNA is primarily based on the identification of hydrogen and nitrogen via the detection of the 2.22 and 10.83 MeV capture γ-rays from hydrogen and nitrogen respectively. Figs. 2.1a and b show schematically the irradiation chamber and the neutron-capture gamma-ray spectrum obtained in a TNA system. The system detects the presence of nitrogen (a constituent of most standard explosives) and estimates its quantity. The estimation of these parameters by themselves led to a high false alarm rate, since nitrogen can be present in many innocuous materials in large quantities.

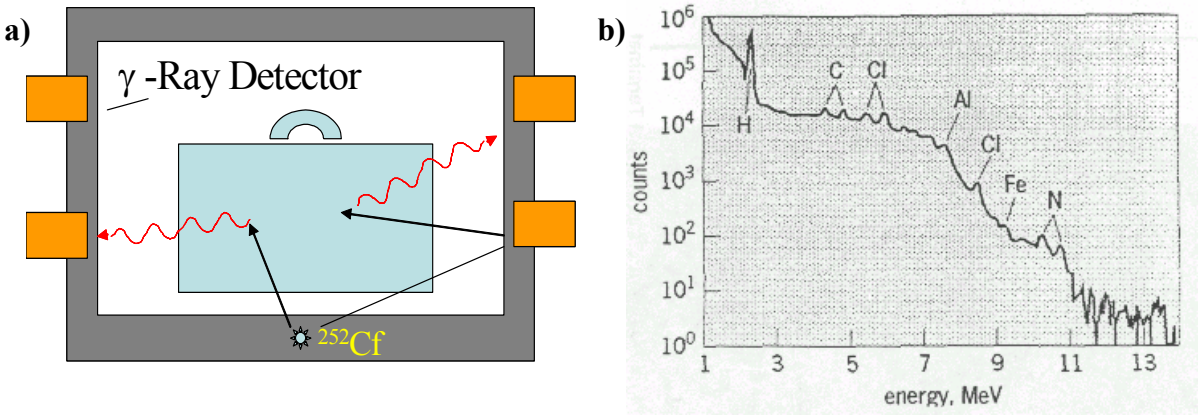

Fig. 2.1: a) Schematic representation of a TNA chamber and b) typical gamma-ray spectrum

The TNA method is used today for inspection of small parcels such as briefcases and portable computers. The system, manufactured by Ancore, USA, is shown in fig.2.2.

Fig. 2.2: TNA explosives detection system for small parcels

The bag is inserted into the container in front of the instrument and the presence of nitrogen above a certain quantity is indicated. The inspection time is about 30s and the explosives threshold quantity is below 1 kg (200g for C4). The radiation dose is about 5 μSv and the total weight of the system is 1180 kg.

2.3 Fast Neutron Activation analysis (FNA)

This technique was conceived in 1986 by Gozani et al [33] as a possible improvement of the TNA (thermal neutron analysis) technique for explosive detection [34]. A collimated beam of fast neutrons (typically 14 MeV) is used to bombard the investigated object. Fast neutron inelastic scattering events activate the inspected-object nuclei, which subsequently release characteristic de-excitation γ-rays, detected by an array of detectors surrounding the object and shielded from direct exposure to the source neutrons [30,34]. The identification of the specific elements found in each volume element or "voxel" is carried out by the deconvolution of the γ-ray spectra measured by each detector. Main signatures used are derived from the detection of the 4.43 MeV γ-ray from ^{12}C, the 1.64, 2.31 & 5.11 MeV γ-rays from ^{14}N and the 6.13 MeV γ-ray from ^{16}O.

FNA suffers from high inherent background that stems from interactions of scattered fast-neutrons with the γ-ray detector material. The detector shielding (which reduces the signal from scattered neutrons), also reduces γ-ray detection efficiency.

2.4 Pulsed Fast Neutron Activation analysis (PFNA)

The PFNA method was developed originally by the SAIC Company, USA [34,35] and the system is now manufactured by Ancore [36-37]. PFNA utilizes a pulsed neutron "pencil beam" which scans the object in a periodic vertical motion. The object moves through the system at a constant horizontal speed, so that a full raster rectilinear scan is obtained (fig.2.3). Collimated mono-energetic neutrons of about 8.5 MeV are produced in 1 ns bunches by an accelerator via the $^{2}H(d,n)$ reaction with 6 MeV deuterons. γ-rays produced by inelastic scattering are detected by arrays of Na(Tl) crystals.

Two limitations that affect FNA, namely, high background and relatively poor imaging capabilities for large objects, can be overcome by pulsing the incident neutrons and making use of the time-of-flight (TOF) method.

The TOF method enables to determine where the mono-energetic neutron interacts [34].

Additionally, the neutrons must be bunched in narrow pulses so that the induced γ-rays arrive at the detector before the front of the next neutron pulse. The flight time required for 8 MeV neutrons to traverse a suitcase or a truck is 20 and 60 ns respectively [34].

Thus the identification of C, O, N, Fe, Cl and other elements is possible using γ-ray spectroscopy, performed for each voxel (volume cell). The 3D location of the interacting nuclide may be determined by the knowledge of the position of the "pencil beam" relatively to the object (at any moment in time) and the depth of interaction is determined by measuring the time span between the emission of the mono-energetic neutron pulse from the target and the detection of the de-excitation γ-ray (fig. 2.3).

Spectral quality is usually high, due to good separation between the signal and major sources of background. The spatial resolution of this method is determined by the dimensions of the "pencil beam" and the timing resolution of the time of flight method. A typical voxel size in this method is about 5×5×5 cm^3 [34]. The reported throughput of the system is 5-20 containers per hour depending on type of cargo.

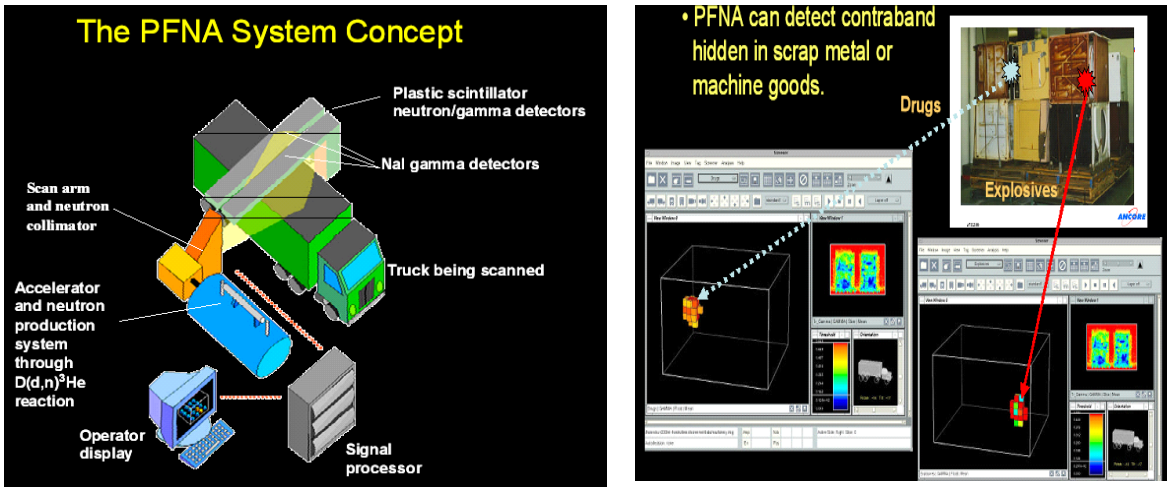

a) **b)**

Fig. 2.3: a) Schematic drawing of the PFNA system and b) a display depicting detection of various materials

A prototype utilizing this method has been built and is currently being applied for inspection of marine containers and trucks at the El Paso, Texas, point of entry from Mexico into the United States, as seen in fig. 2.4.

Fig. 2.4: Ancore PFNA inspection site at Ysleta Port of Entry in El-Paso Texas

The main disadvantage of the PFNA system is its large voxel size. The poor spatial resolution prevents detection of small quantities of explosives and thin sheet explosives. Furthermore, multiple scattering of high energy neutrons adds uncertainty to the location of the nuclear interaction, thus leading to a (false) reduction in the effective measured density.

2.5 Pulsed Fast & Thermal Neutron Activation analysis (PFTNA)

The PFTNA technique generally utilizes a μs-pulsed sealed-tube neutron generator (STNG) producing bunches of 14.1 MeV neutrons that are several μs-wide via the $^{3}H(d,n)^{4}He$ reaction. The γ-rays from these reactions are detected by a suitable set of detectors (usually bismuth germanate (BGO) scintillators).

PFTNA usually involves two types of neutron induced reactions [38-40]:

<u>During pulse emission time</u> (10^{-8}-10^{-7} s) - Fast neutron reactions (inelastic scattering (n, n' γ)) with elements such as C and O. The de-excitation γ-rays are detected and stored

<u>Between two consecutive pulses</u> – Some of the fast neutrons lose their energy by collisions with light elements within the inspected object. When these neutrons are thermalized (10^{-6}-10^{-5}), neutron capture reactions may occur (n,γ) with elements such as H, N and Fe. The prompt capture γ-rays are detected within the same detectors and stored separately from the inelastic scattering spectra.

This sequence is repeated at a frequency of about 10 kHz. Every few hundred pulses the neutron beam is turned off for a longer time interval, such as 3ms, and a different analog-to-digital converter (ADC) collects the events originating from the delayed γ-ray emission from the activated elements such as O, Si, F and P.

This technique combines fast neutron inelastic scattering, thermal neutron capture and delayed activation analysis. Fig. 2.5 shows the time sequence of the nuclear reactions taking place [39].

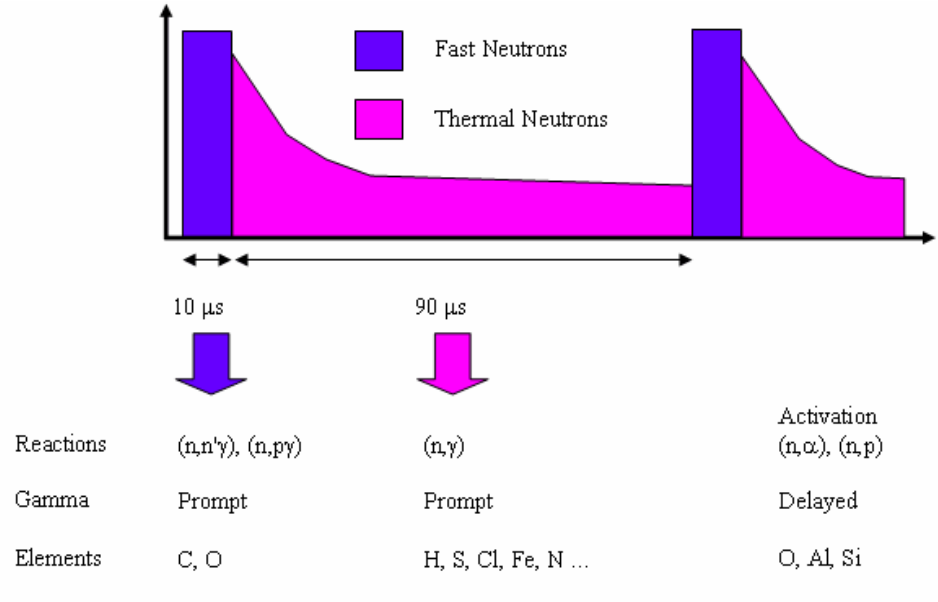

Fig. 2.5: Pulsed neutron generator time sequence

A PFTNA-based device called PELAN (Pulsed Elemental Analysis with Neutrons) was built by Vourvopoulos and Womble [40-41] for the characterization of explosives. PELAN (seen in fig. 2.6) is a small man-portable device that comprises a suitcase containing the necessary power supplies for the neutron generator and the data acquisition system, and a probe which is placed next to the object under interrogation. The probe contains the neutron generator tube (upper horizontal tube in fig. 2.6), the BGO γ-ray detector (lower horizontal tube), and the necessary material to shield the detector from the neutrons (vertical tube). The total mass of the probe and suitcase is less than 45 kg.

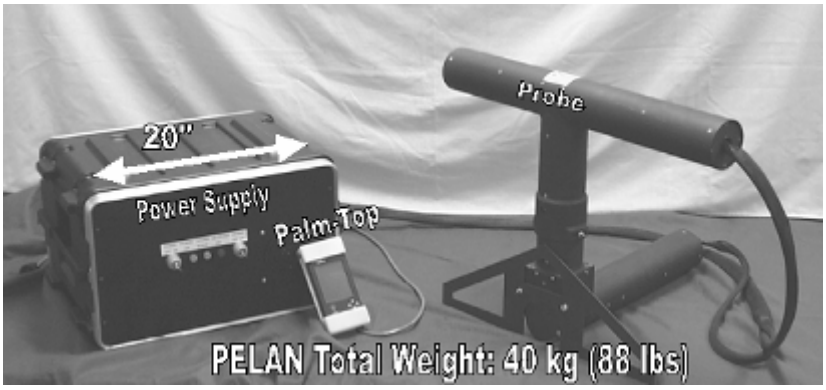

Fig. 2.6: The PELAN system [101]

2.6 Fast Neutron Scattering Analysis (FNSA)

The FNSA technique [42-43] involves bombarding the investigated material with mono-energetic fast neutrons produced by the $^{2}H(d,n)^{3}He$ reaction and the detection of neutrons scattered elastically and inelastically from the interrogated object.

The nuclear characteristics on which the elemental scattering signatures used in FNSA are based are:

a. The elastic and inelastic differential scattering cross sections of the nuclides of different elements, which determine the relative intensities of the elemental signature components at different incident neutron energies and scattering angles

b. The dependence of backscattered neutron energy on target mass number A (fig. 2.7), analogous to that underlying the well-known charged particle technique of Rutherford backscattering analysis (RBS)

The determination of various properties regarding the scattering nuclides (type, quantity and position) is accomplished by measuring the angle and energy of the scattered neutrons. The incident neutron energy may be alternated between two pre-selected neutron energies. Neutron time-of-flight can be used to resolve small energy differences, such as separation between elastically and inelastically scattered neutrons.

Measurements of pure elemental samples such as carbon (graphite), liquid nitrogen and liquid oxygen provide scattering signatures that characterize the scattering nuclide rather well. Readings from two NE-213 liquid scintillation detectors positioned at 45^{0} and 150^{0} (fig. 2.8), at two different incident neutron energies, are combined to form a sample scattering signature.

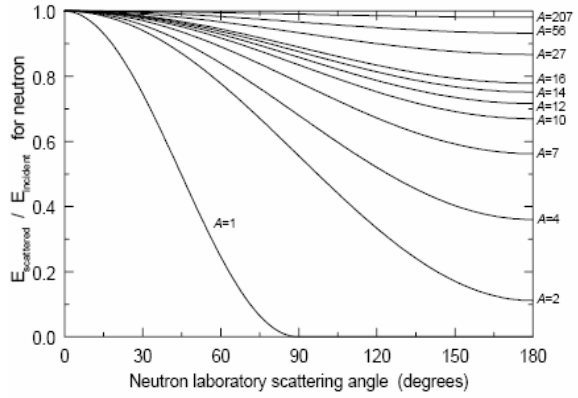

Fig. 2.7: Neutron scattering angle for various elements

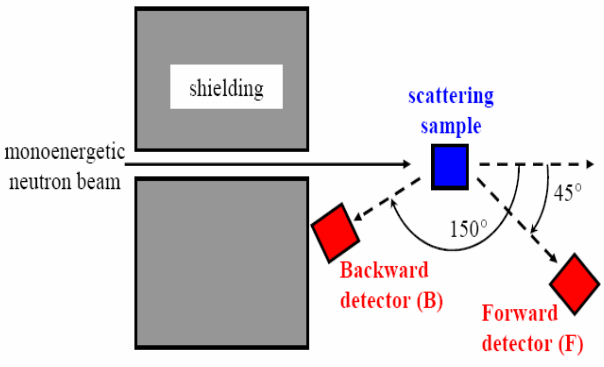

Fig. 2.8: Schematic illustration of the FNSA detection setup [85]

The measured signature for a sample of an unknown material is unfolded into components corresponding to the scattering signatures, in order to determine atomic fractions of each element in the sample. Atomic fractions are used to identify the scattering material.

Fig. 2.9 shows a FNSA system, proposed by Buffler et. al [44] for the detection of illicit drugs in incoming airline luggage.

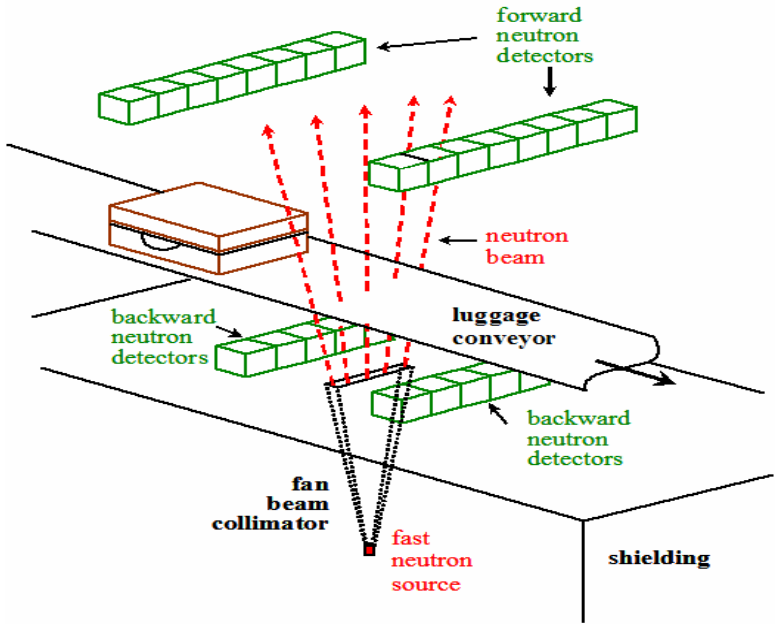

Fig. 2.9: Proposed FNSA system for the detection of illicit drugs in incoming airline luggage [102]

FNSA can measure atomic fractions of the elements in a small sample (0.2-0.8 kg) of a material containing H, C, N and O to an accuracy of few percent [30].
Nevertheless, the FNSA method possesses no imaging capability and does not provide any spatial information regarding the location of the suspicious material in the inspected object.

2.7 Fast Neutron Resonance Radiography (FNRR)

Fast Neutron Resonance Radiography is based on the fact that the absorption of a beam of neutrons varies with neutron energy for a given element. Typically, the total cross-section of each element displays a series of narrow peaks (resonances) and valleys as function of neutron energy. Fast Neutron Resonance radiography can be performed using continuous or pulsed neutron beams. The former is referred to as FNRR while the latter is referred to as PFNTS. Using a mono-energetic neutron source, one can "map" individual elements one at a time. This is usually done by selecting an energy region in which the cross-section exhibits a resonance or a valley for a specific element, but is relatively flat for other elements. For example, we might choose the resonance peak at 7.75 MeV for carbon, as

seen in fig. 2.10. A radiographic image is taken on-resonance and another taken off-resonance (at 6.8 MeV for Carbon, for example). The ratio of the two images will provide an enhanced 2-dimensional (2-D) map of the corresponding element [45-46].
Thus, with appropriate choice of neutron energies, an image of a particular element within an object may be obtained.

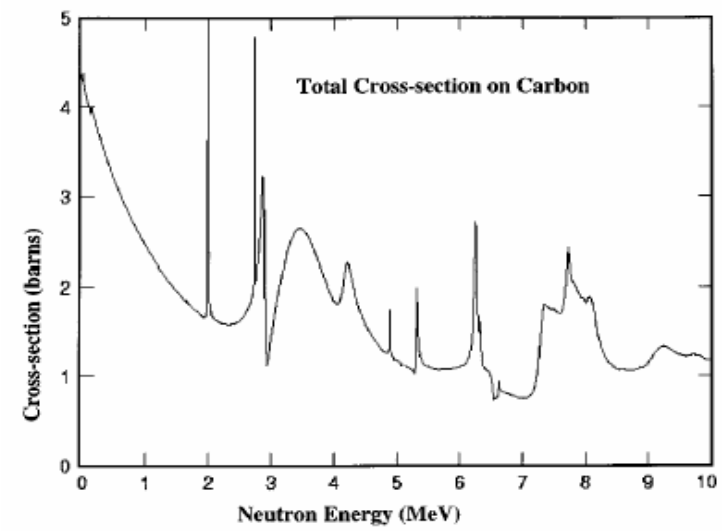

Fig. 2.10: Total neutron cross-section for Carbon [88]

A radiographic image is a 2-D map of projected attenuation, which is sum of the areal densities of all existing elements present, weighted by their attenuation coefficients. For each pixel in the image, there exists a linear equation that reflects the fact that the total attenuation equals the weighted sum of projected elemental areal densities.
When another radiographic image with a different energy spectrum is taken, the resulting linear equations have different attenuation coefficients (weighting factors or attenuation coefficients) and total attenuation, but represent the same projected areal densities, if the orientation of the object to the neutron beam is the same. In principle, when there are more equations than the number of existing elements, the set of linear equations can be solved as a definite least-squares solution for the projected elemental areal densities [45].

Fast neutrons for resonance radiography are commonly generated in the 3-12 MeV energy range, by bombarding a deuteron target with energetic deuterons accelerated by a fixed energy RF quadrupole (RFQ) accelerator [45-46]. The neutron energy from a D-d source has a strong angular dependence (fig. 2.11), which can be exploited to obtain the desired neutron energies by introducing a simple rotational geometry (fig. 2.12). The object-detector assembly is rotated around the D-d neutron source.

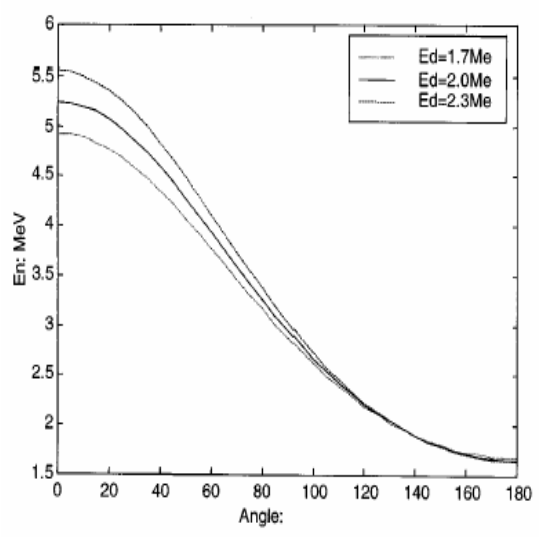

Fig. 2.11: D-d Neutron energy as function of emission angle [88]

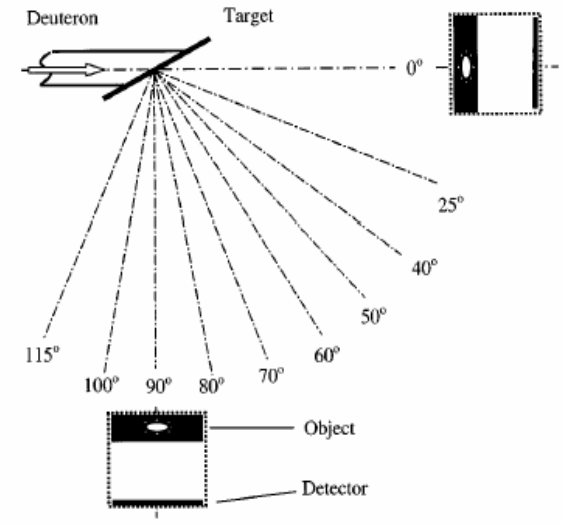

Fig. 2.12: Rotational geometry [88]

Resonance peaks are generally very narrow; accordingly, neutron beams with energies exactly matching these peaks are difficult to obtain, even when using a variable-energy charged-particle accelerator and a thin target to generate mono-energetic neutrons. Moreover, the use of thin targets limits beam currents due to target heating.

R. C. Lanza and G. Chen have built and tested a fast-neutron resonance radiography system [45-46], shown in fig. 2.13. Neutrons passing the object are measured by a detector, which includes a scintillator and a charge coupled device (CCD). In the scintillator, fast neutrons are scattered by hydrogen nuclei (a proton) which recoils, then ionizes and excites the molecule or crystal of the scintillator, causing the emission of light.

Scintillation light from the neutron detector is reflected by a mirror and then collected with a lens onto a charge coupled device (CCD), which converts individual photons into electrons. A CCD is an analog integrated circuit that converts an optical image into an electronic one. This arrangement enables the CCD (and other electronics) to be shielded from the direct neutron beam.

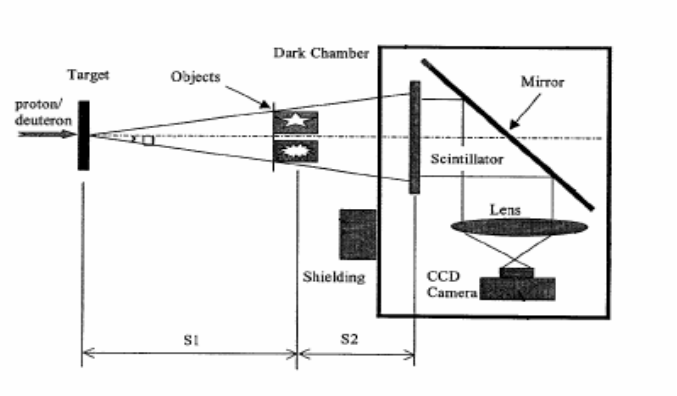

Fig. 2.13: Fast neutron radiography system [89]

Electrons, induced by photons are accumulated in each pixel during the exposure time and subsequently transferred to readout electronics. After the desired exposure time, the number of electrons in each pixel is converted to a digital level that is communicated to a computer that generates the final digital image.

Lanza et al. performed a radiography simulation, using the "COG" radiation transport code, of a bag [45-46] consisting of a thin aluminum shell (~40×30×10 cm^3) with a wooden handle, thick cloth covering and steel fittings. The bag contained: a newspaper, a bag of sugar (~100gr), cocaine-HCl (~100gr), a travel umbrella, a 4" switchblade knife, a paperback book, a 300 gr block of plastic explosive (50/50 wt % mix of RDX and PETN), a pen and pencil set, a small camera, an automatic pistol with extra ammunition clip, a flat paper notebook and a selection of cotton, wool and nylon clothing items. The bag is heavily loaded to an average density of ~0.5 gr/cm^3. Fig. 2.14a and b show the neutron image at 0^0 and 140 keV x-ray image respectively.

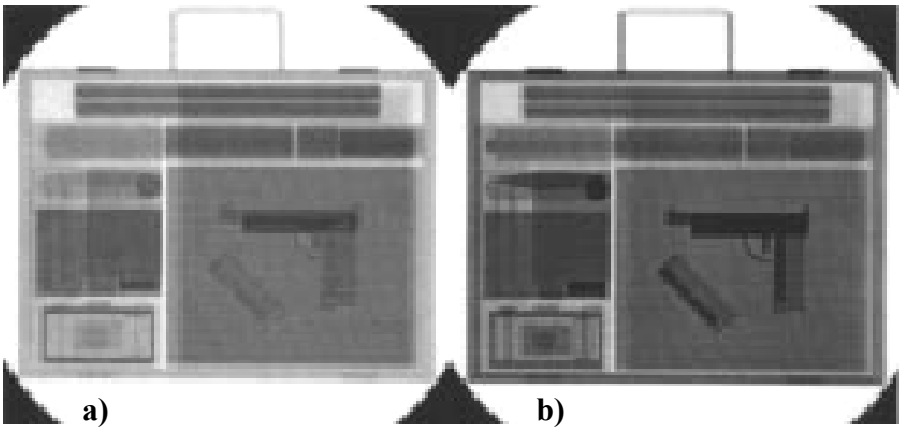

Fig. 2.14: Fast neutron radiography simulation at a) 0^0 and b) X-ray radiograph

Neither method can distinguish the book from the plastic explosive, or the sugar bag from the drug bag. The plastic explosive can be identified by its high nitrogen and oxygen content and low Hydrogen and Carbon content. The cocaine has about equal amount of hydrogen and carbon, but very little amounts of oxygen.
Fig. 2.15a and b show calculated elemental images for nitrogen and oxygen respectively.

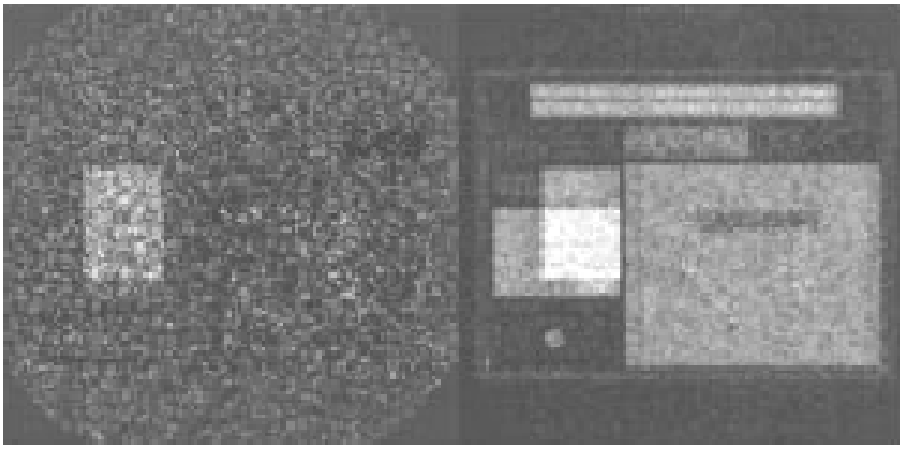

a) **b)**

Fig. 2.15: Calculated elemental images for a) Nitrogen and b) Oxygen

The principal problems encountered when using this method are: a) sensitivity to γ-rays which degrades image contrast b) a requirement for small viewing angle ($<10^0$) so that the neutron energy falloff across the image is significantly smaller than the difference between on and off resonance energy, thus the on-resonance condition is maintained over the entire image.

Another element-sensitive, fast-neutron resonance radiography system has been built and tested by the De-Beers company [47] in collaboration [48] with the Department of Nuclear Engineering at MIT, the South African Atomic Corporation and Brookhaven National Laboratory, for the purpose of detecting the presence of a specific substance in a host body, such as a diamond inclusion in a piece of kimberlite (a dense rock formation in South Africa containing peridotite- coarse-grained rocks, in which it is well known that diamonds may be found).

In this variant, individual kimberlite particles are irradiated with a beam of fast mono-energetic neutrons. The image created by the transmitted neutrons carries information regarding the existence of the substance of interest in the host particle. The mono-energetic neutron beam is energetically well defined, such that the neutrons have energies around the

resonance for the substance in question. In the case of detection diamond in kimberlite, the neutrons may have energy of about 8 MeV which is at a resonance peak in the total cross-section of Carbon (fig. 2.10) and at which there is good contrast between diamond and kimberlite absorption [47].

By modifying the accelerator acceleration voltage, the samples can also be irradiated with a fast neutron beam at two distinct energy levels, producing on-resonance and off-resonance images (as explained in the previous section).

The neutron detection apparatus built by De-Beers [47] (fig. 2.16) is based on a fiber scintillator screen, comprised of bundles of side-by-side parallel fibers, each containing the scintillating material.

Neutrons transmitted by the kimberlite enter the fibers and generate scintillation via knock-on protons. The light travels within the fibers to the extremities of the fibers. An amorphous silicon detector plate is placed at the farthest end of the fibers to collect the emitted light, which is processed and analyzed in the electronic processor.

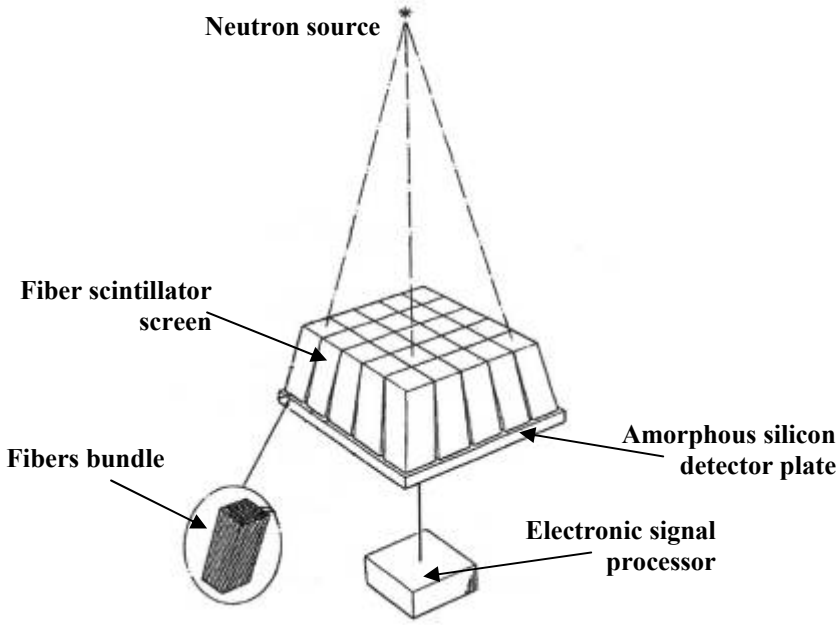

Fig. 2.16: Fast neutron detection apparatus built by De-Beers [47]

2.8 Pulsed fast neutron transmission spectroscopy (PFNTS)

The PFNTS technique [5] is a variant of Fast-Neutron Resonance Radiography that requires an intense "white" spectrum of ns wide neutron bunches. These are usually produced via ^{9}Be(d,n) (see fig. 2.18) or ^{3}H(t,n)He reactions. In this method, a broad energy-spectrum fast-neutron beam (0.8-10 MeV) transmitted through an object (see fig. 2.17a) is modified according to the resonant features present in the cross-section of this element. (see fig. 2.17b). Using the time-of-flight (TOF) technique, the spectrum of the transmitted neutrons is measured by a position-sensitive neutron detector and the attenuation at particular neutron energies, that corresponds to specific cross-section structures ("resonances") of light elements, such as C, N and O, is measured [13-15].

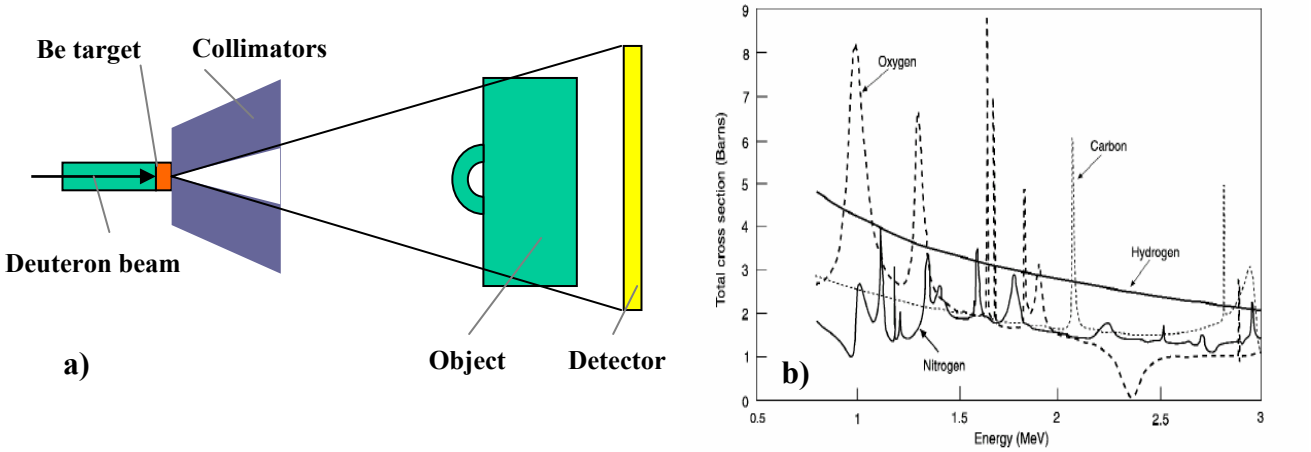

Fig. 2.17: a) Schematic description of the PFNTS method (not to scale) and b) the total cross sections of C, N, O and H [35]

The knowledge of the total cross-section allows the measured transmission spectra to be unfolded, and the areal densities of elements present in the interrogated object to be determined. The method reveals the presence of C, O, N, and other elements in the interrogated object.

Since the PFNTS method provides the operational basis of the imaging system presented in this work, it will be described here in detail.

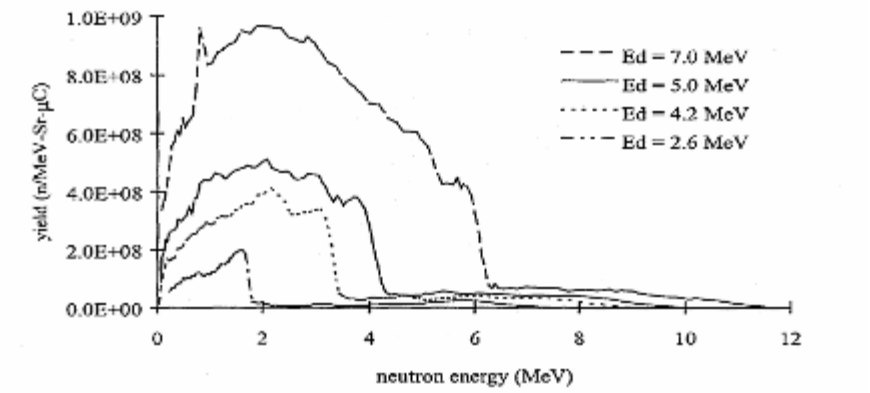

Fig. 2.18: Neutron yield spectrum at different deuteron energies for the Be(d,n) reaction [86]

2.8.1 The University of Oregon PFNTS system

Overley [5-7] was the first to demonstrate that knowledge of the total cross sections for H, C, N, O, and other elements of interest allows the measured transmission spectra to be unfolded, thus providing information on areal densities of elements present in the interrogated object. The combined effective contribution from other elements (which are of no interest in the present context) was taken together as fictitious element X and assigned an energy-independent cross-section of 3 barns [9].

For every pixel in the target, the energy-dependent transmitted neutrons are measured and used to determine relative amounts of the above mentioned elements.

The University of Oregon (Overley et al) developed a TOF spectrometer composed of a 16-detector linear horizontal array with 3×3 cm^2 pixels [9]. The neutron spectrometer consisted of a 10 cm-diameter, 2.5 cm-thick liquid scintillator coupled to a fast photomultiplier [5]. Timing signals derived from the deuteron beam pulse and from the photomultiplier were routed to a time-to-amplitude converter (TAC). Resulting pulses were digitized by an analog-to-digital converter (ADC) and stored by an online computer as 1024-channel neutron flight-time spectra. Proton recoil events of energies less than 0.3 MeV were rejected at the ADC. Overall time resolution was about 2 ns [9].

TAC dead time was reduced by gating the TAC off during 96% of the beam cycles for a 0.1 μs interval centered about the potential arrival time of the prompt γ-ray timing signal at the TAC. The γ-ray peak was reduced by a factor of 25 without altering the rest of the spectrum.

Figure 2.19 shows the TOF spectrometer logic diagram [8]. The 16 spectrometers are individually calibrated by enabling the time-mark generator for 5 seconds, and reading and analyzing the time-mark data. Live charge for each spectrometer must be recorded in each neutron spectrum, since losses depend upon counting rates that, in turn depend upon the contents of the inspected object. The circuitry shown allows beam-current integrator pulses to be stored at a selected place in every TOF spectrum.

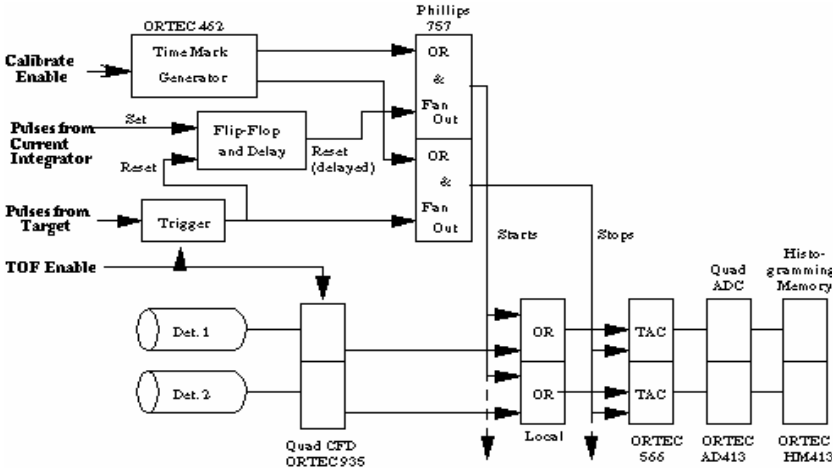

Fig. 2.19: Logic diagram of the TOF spectrometer built by the University of Oregon [38]

2.8.1.1 University of Oregon tests

In 1996, a series of blind tests was conducted by the Federal Aviation Administration (FAA) at the University of Oregon [9,11], in order to evaluate the effectiveness of the PFNTS technique for explosive detection in real luggage. The tests involved 134 different luggage items and 8 different nitrogen-based explosives, which were interrogated using neutron time-of-flight (TOF) spectrometer configured as described above.

As a result of these tests, Overley et al. reported [9,11] detection probability of 93.3% (for all explosive types, after algorithm adjustments), 4% false alarm probability (for all explosive types after algorithm adjustments). The undetected explosives weighed 450 grams or less and were less than 1.2-cm in thickness [9].

Figure 2.20 shows two gray-scale maps obtained from a suitcase in one of the Oregon blind test experiments [8]. The first (a) shows explosive likelihood (b-values), where black is innocuous and white is explosive. Partly filled pixels are marked with circles and should be ignored. A sheet of explosive is indicated in the lower left corner. The second grey-scale map (b) contains Z values. The large white rectangular area has Z values up to 40. It was identified as lead (Pb) by including the lead cross-section in the deconvolution. The pixels marked with circles indicate poorer than usual fits (higher values of chi-squared) to the measured attenuation. When the data was reprocessed including the lead cross-section, the fits dramatically improved. The b-values were originally innocuous but after reprocessing with lead added, the positive explosive indication shown in fig. 2.20 appeared.

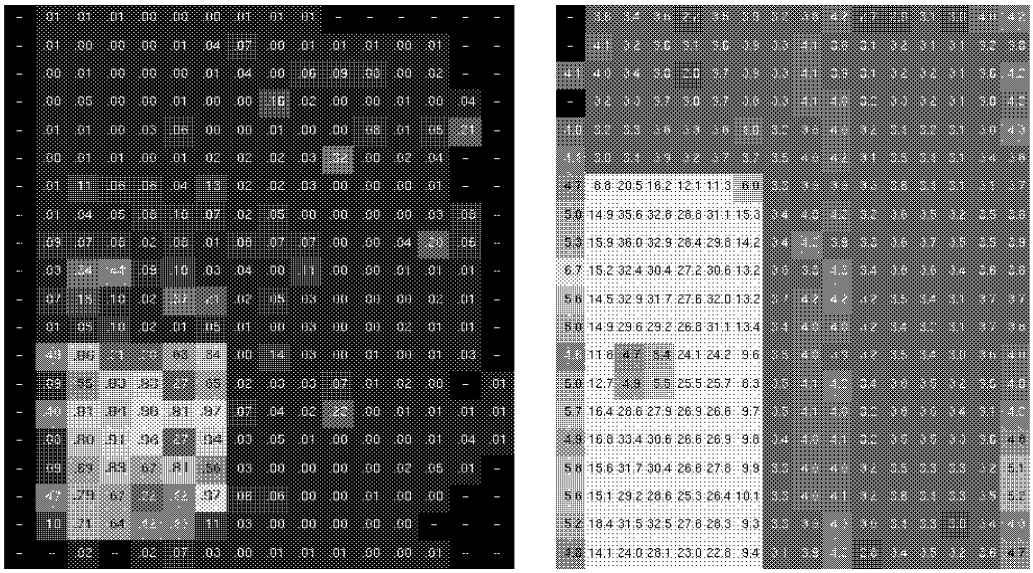

a) **b)**

Fig. 2.20: Gray-scale maps obtained from one suitcase from Oregon's blind tests [38]. a) Shows explosive likelihood (b-values) and b) contains Z values

Figure 2.21 is a drawing of an accelerator system that National Electrostatics Corp. (NEC) of Middleton, Wisconsin has proposed for this use [8]. It uses a Torvis high current negative ion source with harmonic chopping and bunching to deliver a 20 μA average current of bunched 4.2 MeV deuterons. It has a quoted spark rate of 2 or less per day, and a quoted up-time of 95% including scheduled maintenance. The deuteron beam can be quickly intercepted in a Faraday cup before acceleration and the voltage of the terminal will remain at 2.1 MV. The beam can be transported and focused to a diameter of 5 mm or less on a Be target.

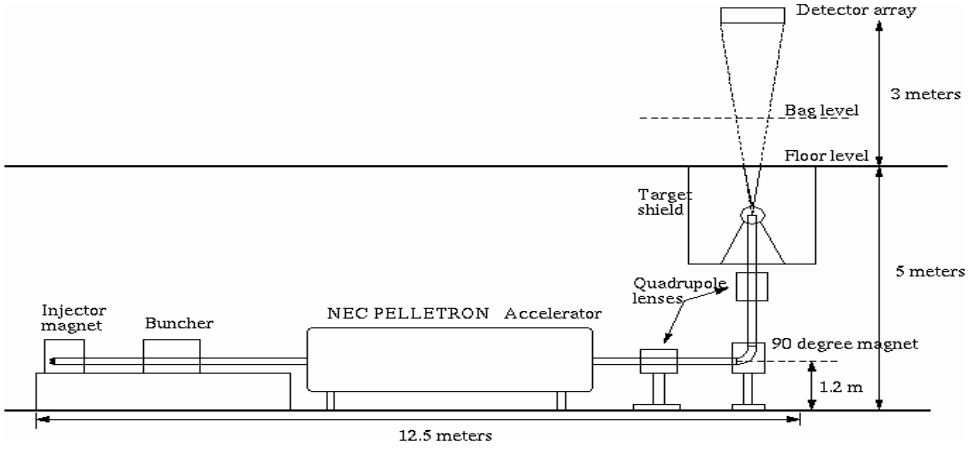

Fig. 2.21: Drawing of an accelerator system proposed by the National Electrostatics Corp. of Middleton, Wisconsin for use with the TOF spectrometer built by the university of Oregon [38]

Additionally, the transport system incorporates a 90 degree magnet and a pair of quadrupole triplet lenses to produce a vertically-directed neutron beam. The target and collimator are 1 m below floor level. The luggage conveyor is 1 m above the floor, and the neutron detectors are 2 m above that. This geometry allows the accelerator to be conveniently located in a ground level vault. Luggage is handled at concourse level, and the neutron detectors are well off the floor in otherwise unused space. A labyrinth needed around the scanning location to shield people from scattered radiation was not designed at that stage.

After several years, the University of Oregon discontinued its work on PFNTS.

2.8.2 The Tensor Technology Inc. system

During the 1990's, Tensor Technology also developed a TOF fast neutron spectrometer, assembled for identification of contraband in sealed containers.

The system was based on a two dimensional 99-element array [11] with pixel size $4\times4\times3cm^3$ [96], as seen in fig. 2.22. At that time, it was stated that reduction of pixel size would entail an increase in the quantity of electronics to an unmanageable level [10].

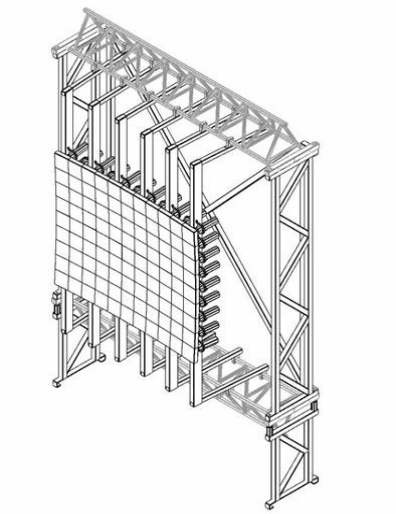

Fig. 2.22: Two dimensional matrix of 99 individual scintillation detectors, each coupled to a light guide, photomultiplier and electronics. Pixel size $4\times4\times3cm^3$ [11-12,49]

TOF measurements were performed using a Time-to-Digital Converter (TDC) [10] which digitized the TOF measurements without recourse to any analog circuitry. The TDC method directly counts the number of clock cycles between the start and the stop signals with a fast clock, and then determines the position of the stop pulse, within the clock pulse, using an interpolator. This method resulted in faster conversion times (compared to the usage of a time-to-analog converter (TAC) and an analog-to-digital converter (ADC)) and significantly reduced the electronics complexity. Fig. 2.23 describes a schematic description of a TDC based data acquisition system. The Constant Fraction Discriminator (CFD) is used to generate the start timing signals which are fed into the TDC.

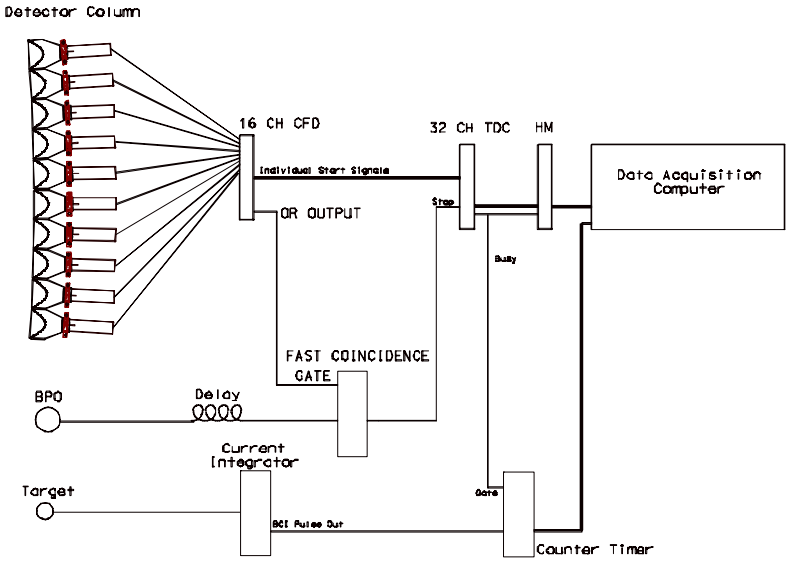

Fig. 2.23: Schematic layout of TDC based data acquisition system [34]

2.8.2.1 Tensor Technology Tests

In 1997, 150 suitcases were scanned at Tensor Technology as a part of an FAA blind test [11], aimed at evaluating explosives detection using the TOF spectrometer described above. The setup built by Tensor Technology [10] is comprised of a matrix of individual scintillation detectors positioned as a 2-dim array, as shown in fig. 2.22.

Detection probability reported in these tests [11] was 88% (all explosive sizes and thicknesses) and a false alarm probability of 24% (all explosive sizes and thicknesses). Detection probability for thin explosives (1.2 cm or less thick and weighing 450 gr or less [based on data from ref. 9]), was 40% [11]. Fig. 2.24 illustrates neural net values obtained during Tensor's blind testing for a slurry sample in a suitcase.

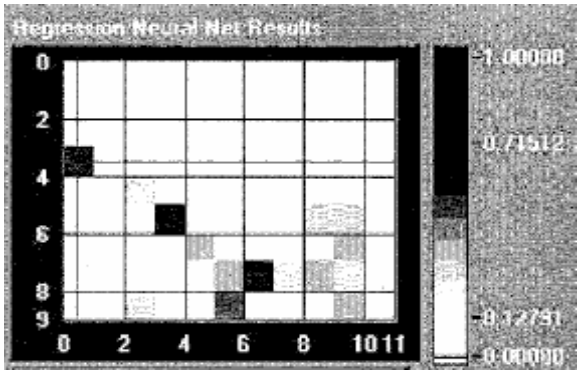

Fig. 2.24: Neural net values obtained during Tensor blind testing [11]

Tensor had proposed an innovative approach to the PFNTS neutron source, using a cyclotron rather than a linear accelerator in order to reduce footprint of the explosives-detection device [35] (fig. 2.25a and b). The Ebco Technologies (British Columbia, Canada) cyclotron TR9D, proposed for use by Tensor, had reported current stability of <1% and weight of 20 tons. Total weight of the system with shielding amounts to 701 tons and size of 8×13m.

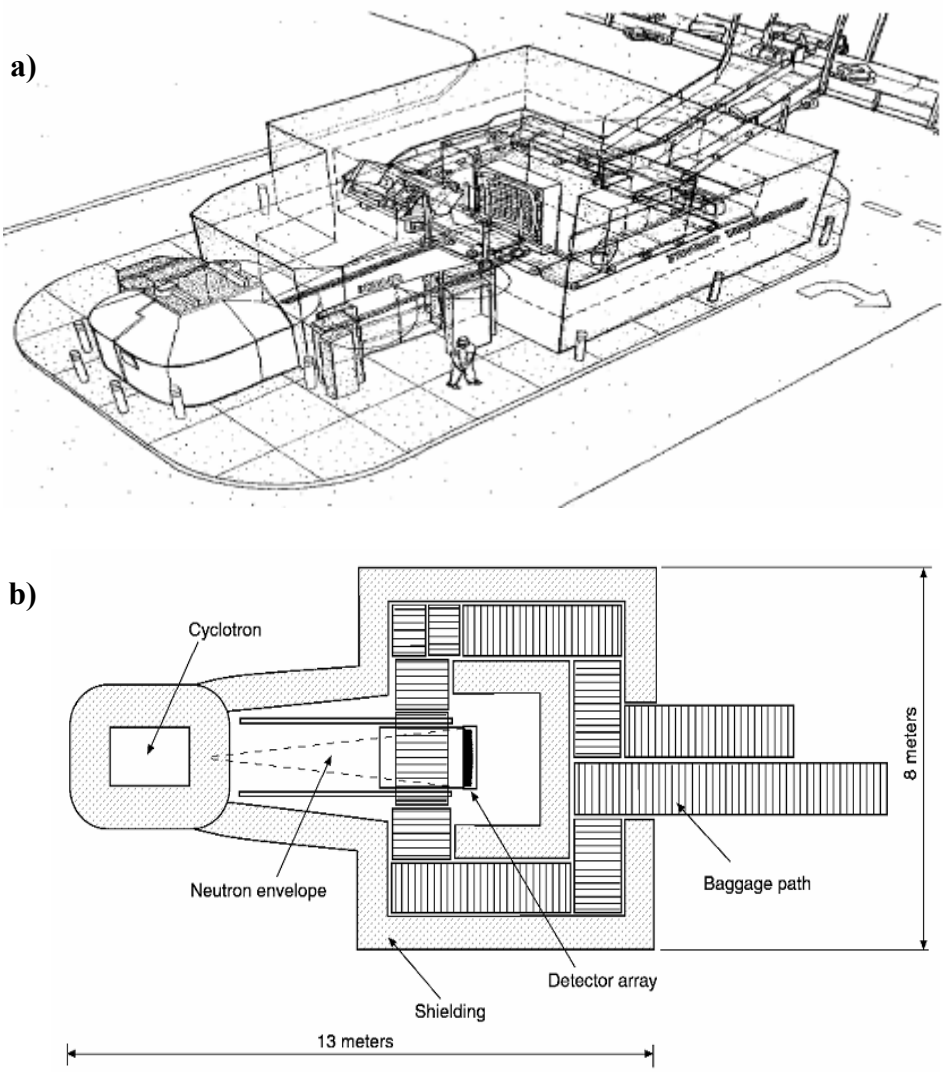

Fig. 2.25: a) Artist's conception of the layout of the explosives-detection system proposed by Tensor, b) Top view of possible baggage flow path [35]

Several concerns were raised regarding the above described system configuration proposed by Tensor [11]. One of these was that weight and space requirements of the cyclotron-based design may preclude integration into the passenger baggage inspection line at existing airports. In addition, deployment of such a system is possible only on the ground floor, due to weight considerations. These concerns have led Tensor to continue refining their detection algorithms, electronics data collection speeds and to pursue an alternative, more compact neutron source, as described in chapter 1 section 1.4.

2.9 Summary of Oregon & Tensor PFNTS tests

It has been claimed by these groups that both series of blind tests provided good detection levels for bulk explosives (of thickness greater than 1.2 cm and weighing more than 450 gr [9]). Thus the PFNTS method appears to provide a very robust set of measurements for explosives detection, in the sense that they lead to unequivocal quantitative assignment of C, N & O areal densities. Table 2-1 provides a summary of detection performance levels obtained in these tests.

Table 2-1: Summary of detection performance level

Group	Explosive category	Detection probability P_d	False alarm probability P_f
Oregon University	All explosives	93.3%	4%
Tensor Tech.	All explosives	88%	24%

However, the pixel size determined by these detectors (few centimeters) posed an intrinsic limitation on the position resolution, which did not permit reliable detection of objects that are smaller and thinner (<1cm thick).

Thus, the National Academy of Science Panel (NAS) in 1999 [11], advised against building an operational airport prototype, since no compact, suitable neutron source was available at that time, nor was the detector spatial resolution adequate for reliable detection of sheet explosives (thinner than approx. 1.2 cm and weighing less than 450 gr [9]). Nevertheless, it recommended developing existing and new technologies in the field of neutron sources and neutron detectors.

In order to respond to the above challenge, a next-generation PFNTS detector should be capable of providing a mm-size spatial resolution with good TOF spectroscopy per pixel and an ability to work at high neutron fluxes. The following chapter describes a detector that attempts to meet the above requirements.

Chapter 3

3. Time Resolved Integrative Optical (readout for) Neutrons (TRION)

3.1 Requirements of a PFNTS detector

The present work seeks to provide an efficient, large-area fast-neutron detector for combined sub-mm spatial imaging and TOF spectrometry, capable of loss-free operation in mixed, high-intensity neutron-gamma fields.

Table 3-1 summarizes the properties required from a PFNTS detector.

Table 3-1: PFNTS detector requirements

Detector parameter	**PFNTS Requirement**
Detector area	> 50×50 cm^2
Detection efficiency	10-15%
Separation between neutrons and γ-rays	Good discrimination
Counting rate capability	> 10^6 c/s·cm^2
Neutron spectroscopic capability	Essential
Energy resolution	Better than 3% at 8MeV
Position resolution	Better than 1 mm

3.2 The TRION concept

TRION is a novel, fast-neutron imaging device based on time-gated optical readout. The concept was first proposed by Dangendorf et al. [26] of the PTB Institute, Germany and subsequently developed at Soreq NRC in close collaboration with the PTB group.

Fig. 3.1 provides a schematic description of the TRION detector configuration.

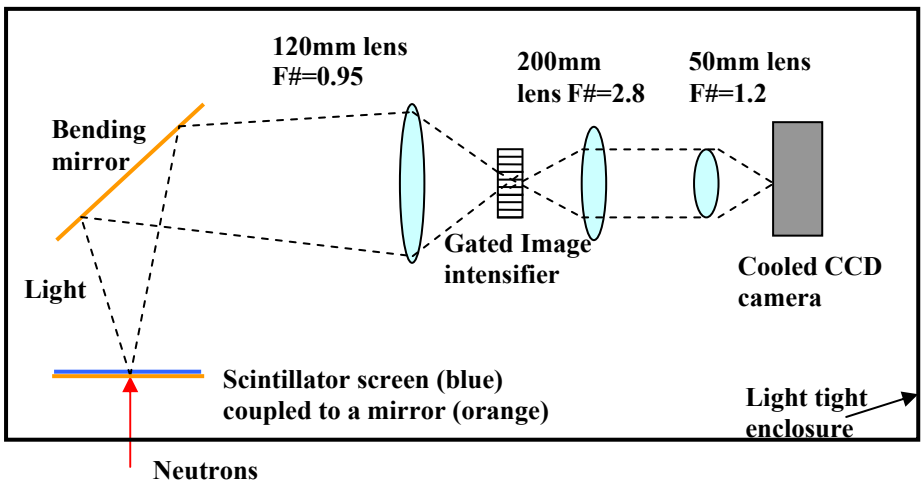

Fig. 3.1: The TRION concept

The detector is designed to detect fast-neutron pulses produced, for example, in the ^{9}Be(d,n) reaction using a pulsed (~1 ns bursts, 1-2 MHz repetition rate) deuteron beam. As illustrated in fig. 3.1, these fast-neutron pulses impinge on the scintillator screen causing the emission of light from the screen via knock-on protons. The light is reflected by a front-coated bending mirror (98% reflectivity, positioned at an angle of 450 relative to the neutron beam direction) towards a large aperture 120 mm F#0.95 lens. The light is amplified by a ns-gated image intensifier and transmitted by an optical tandem assembly comprising a 200 mm lens (F#=2.8) and a 50 mm lens (F#=1.2) coupled to a cooled CCD camera.

The gated image intensifier acts as a fast electronic shutter for the CCD camera. By selecting the gate time relative to the neutron beam pulse, it is possible to select a time window (gate width) that corresponds to a preselected neutron energy bin. In a typical pulsed fast-neutron beam, the burst rate is of the order of 2 MHz. Within a time period of 500 ns, depending on neutron-source to detector distance, the system should integrate neutrons into an image in a well defined time window. Typical gate width is 10 ns.

Thus, the detector is based on an integrative (as opposed to single-event counting) optical technique, which permits neutron energy-resolved imaging via time-gated optical readout. This mode of operation permits loss-free operation at very high neutron-flux intensities.
The TRION neutron imaging system can be regarded as a stroboscopic photography of neutrons arriving at the detector on a few-ns time scale.

Although stroboscopic time-resolved optical imaging techniques have previously been used to determine various physical properties, no time-resolved neutron imaging has yet been performed.

3.3 Detailed description of TRION

Fig. 3.2 shows the engineering drawing of TRION. Its neutron converter consists of a fast plastic (polystyrene) scintillating fiber screen, 200×200×30 mm^3 in dimensions, positioned at the front end of the system. The reason for using scintillating optical fibers, rather than a plain plastic scintillator slab, is to maintain the position resolution, independent of screen thickness, as scintillation photons are emitted from one plane (the fiber screen surface), while in a plain slab they are emitted from different points along its thickness. The fiber diameter in the screen is 500 μm. A neutron that interacts in the fibers transfers part of its

energy to a proton, which gives rise to scintillations in the fiber. A fraction of this light travels along the fiber and is emitted at its extremities. The light is transported via a front-coated 45^{o} mirror and is viewed by a custom designed large-aperture lens (120 mm F#0.95) and a nanosecond-gated image-intensifier. A cooled CCD camera, positioned at the rear-end of the system, captures the image from the image intensifier through a set of two lenses. The camera integrates the image over many cyclotron pulses, until sufficient counting statistics in the pixels of the CCD is obtained.

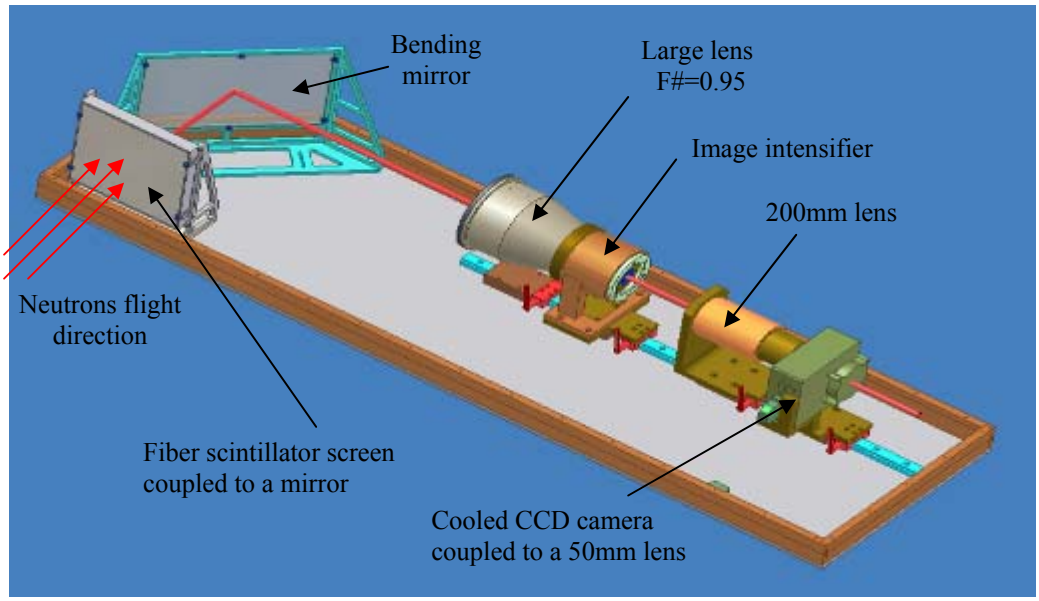

Fig. 3.2: An illustration of the TRION detection system

The system components are mounted on linear guides that can move freely along the rail, or be kept static by the attached motion-limiters. All system components are mounted in a light-tight enclosure. The optical alignment procedure is provided in appendix 1.

Table 3-2 provides a summary of distances between the system components.

Table 3-2: Summary of distances between system components

From	To	Distance (mm)
Scintillator screen	Large lens F#=0.95	750
Large lens F#=0.95	Image intensifier	~5
Image intensifier	200 mm lens	71
200 mm lens	50 mm lens (Coupled to CCD)	~30 mm

Figs. 3.3 and 3.4 show two views of the TRION system. The 200 mm lens is mounted backwards, i.e. the bayonet end faces the image intensifier, while the front end faces the 50 mm lens (attached to the CCD camera).

In this manner, the back end of the 200 mm lens is focused on the image intensifier, thus emitting a parallel beam of light towards the 50 mm lens, as illustrated in fig. 3.1.

The following section will provide a more detailed description of each of TRION's components.

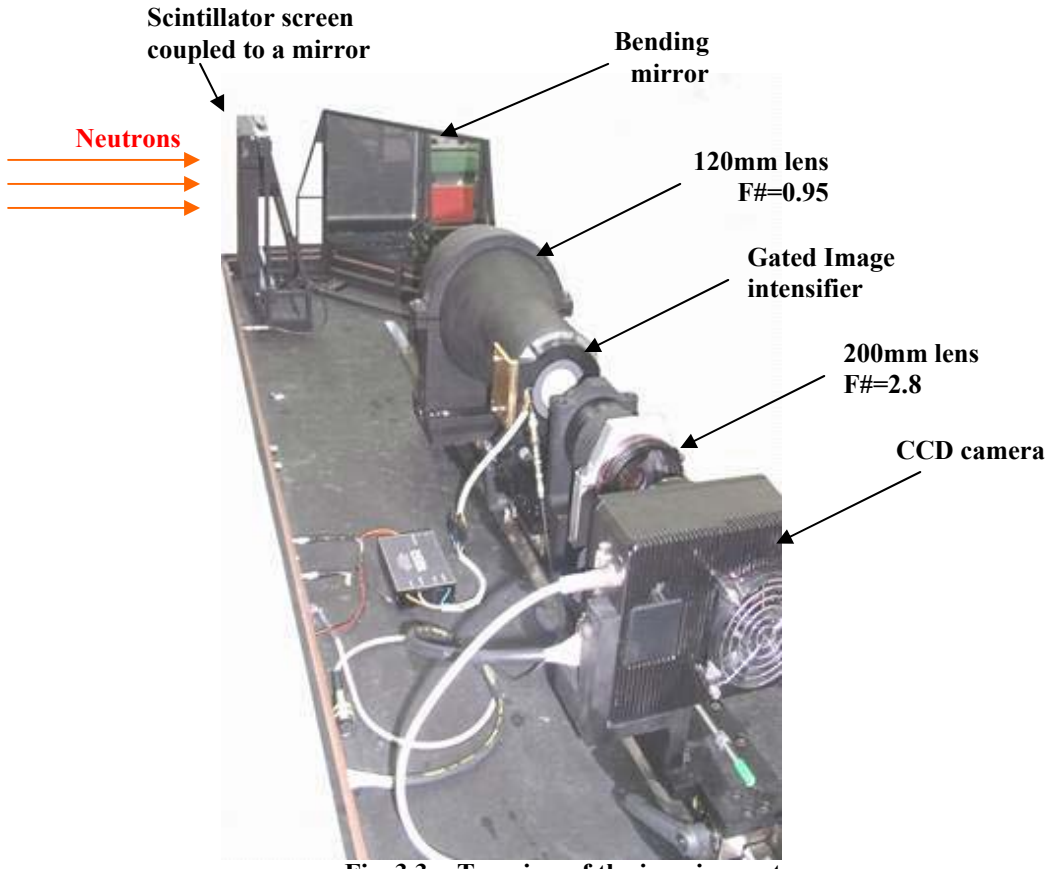

Fig. 3.3: Top view of the imaging system

Fig. 3.4: Side view of the imaging system

3.3.1 Scintillator screen

A plastic scintillator screen is used in this work as neutron detector. As mentioned in chapter 1, section 1.3.3, the most common fast-neutron detection scheme is based on conversion of the neutron into a proton, via neutron elastic-scattering by hydrogen present in the detector medium.

Fast neutrons with energies E_n in the 0.1-10 MeV range can be detected by n-p recoil reactions in plastic scintillators. The kinetic energy of the recoil protons E_R is given as function of their scattering angle θ [17]:

$$E_R = E_n \cos^2(\theta) \qquad [3\text{-}1]$$

When a charged particle transfers energy to matter, it will either produce heat, ionize the atoms or raise electrons into excited states. If the material is a scintillator, when these excited states decay to lower energy states some of the excess energy will be carried away by a photon.

Photon production [50] in organic scintillators is a molecular process most easily described by using the potential energy diagram illustrated in fig. 3.5. The lower curve represents the potential energy when all of the electrons are in the ground state; the upper curve represents the potential energy of an excited state.

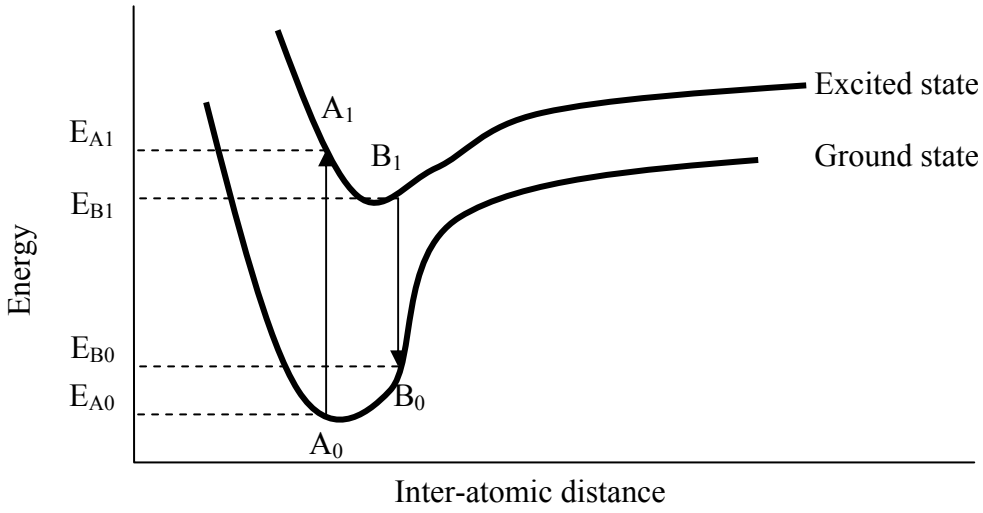

Fig. 3.5: Simplified energy diagram of organic scintillators

The Frank-Condon principle states that the energy deposited by a charged particle not dissipated as heat causes a transition from A_0 to A_1 ($E_e=E_{A1}-E_{A0}$) in a time (~0.1 ps) that is short compared to the vibration time of the molecule. Some energy is lost through lattice vibrations moving the molecule to B_1. After a time (~10ns), long compared to the vibration time, the excited state may decay to the ground state (B_1 to B_0) as the excess energy ($E_p=E_{B1}-E_{B0}$) is carried away by a photon.

The fluorescent emission produces approximately one photon per every 100 eV of deposited energy. Due to the fact that the energy required to generate an excited state (E_e)

exceeds that carried away by photons (E_p), the probability for reabsorption of emitted photons is small, i.e., the scintillator is transparent to the light it generates.

Secondary scintillators are frequently used to "shift" this emitted light to longer wavelengths. These secondary flours have high absorption cross-section at the wavelengths generated by the primary scintillations.

When choosing a scintillator, the following properties have to be considered:

- Neutron detection efficiency
- Light output per detected neutron
- Scintillation light decay time

Intrinsic neutron detection efficiency of a scintillator is defined [50] as the efficiency of conversion of an impinging neutron into a light pulse. It is influenced by the isotopic composition of the scintillator and the interaction parameters of the neutron with these isotopes. On the assumption that each converted charged particle will produce scintillation, the detection efficiency of a device based on recoil protons or other recoil nuclei can be calculated from the scattering cross-section σ_s of the target nuclei.

A typical plastic scintillator (polyvinyl-toluene, or polystyrene) contains H and C atoms with approximately similar atomic density $\boldsymbol{N}$ (atoms/cc), thus competing reaction due to carbon-neutron scattering must be taken into account when calculating the probability for creating a knock-on proton. Hence, the detection efficiency (neglecting protons resulting from C(n,p) reaction) is then given by:

$$\varepsilon = \frac{N_H \sigma_H}{N_H \sigma_H + N_C \sigma_C} \left(1 - exp^{-(N_H \sigma_H + N_C \sigma_C)d}\right) \qquad [3\text{-}2]$$

Where the $\boldsymbol{H}$ and $\boldsymbol{C}$ subscripts refer to separate carbon and hydrogen values for the quantities defined above.

The detection efficiency per incident neutron was calculated using known cross-sections [51] for a polystyrene-based screen. Fig. 3.6 shows the calculated detection efficiency of polystyrene scintillator vs. neutron energy for scintillator thicknesses of 1, 5 and 10 cm.

As the detector thickness increases, the resonances in the carbon cross-section become more prominent. As can be observed, in order to obtain 10-20% detection efficiency for neutrons of several MeV energy, a **30-50 mm** thick scintillator is required.

The light output of a typical plastic scintillator, based on polyvinyl-toluene (BC-400 or EJ-200) is about **10,000 photons** per MeV, for a minimum ionizing particle [52]. A polystyrene (BCF-12) based scintillator emits about 70-80% of this value [53]. This compares unfavorably with inorganic scintillators such as NaI(Tl) or CsI(Tl), which emit 38000-54000 photons per 1 MeV γ [53], but have much longer decay times.

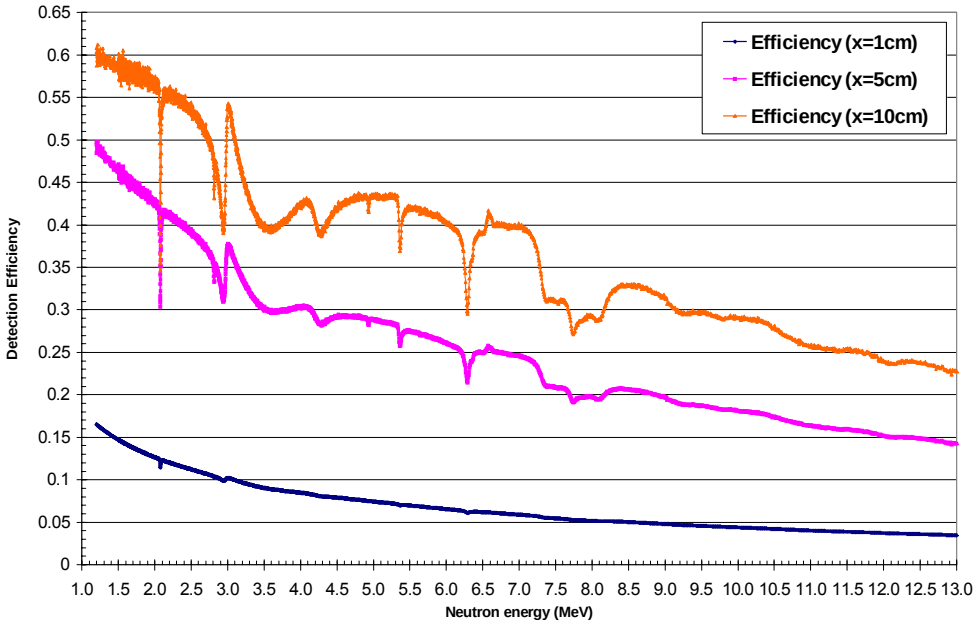

Fig. 3.6: Detection efficiency of polystyrene scintillator vs. neutron energy for various scintillator thicknesses

When performing TOF measurements the decay time-constant of the scintillation light (wavelength of approx. 420 nm) must be as short as possible, in order to provide accurate timing. The decay curve of a NE102 plastic scintillator (composition similar to polystyrene) is shown in fig. 3.7 [54-55]. It can be decomposed into 3 components with decay constants of approximately 2.5, 12 and 68 ns. The ratio of amplitudes of each component is 1:0.026:0.0023 respectively. This is considered to be a fast scintillator and has been chosen as the material used for our screen.

As mentioned previously, the screen must be 30 to 50 mm thick in order to obtain adequate detection efficiency. The screen is viewed by a lens focused on a certain depth inside the screen. However, as scintillations may occur at any depth in the scintillator, only some of

them will be in focus as the CCD is focused on the middle of the scintillator. Thus, the thicker the screen, the poorer the overall spatial resolution. This effect, referred to as *depth-of-field*, is particularly important for large aperture lenses, positioned at a short distance from the screen.

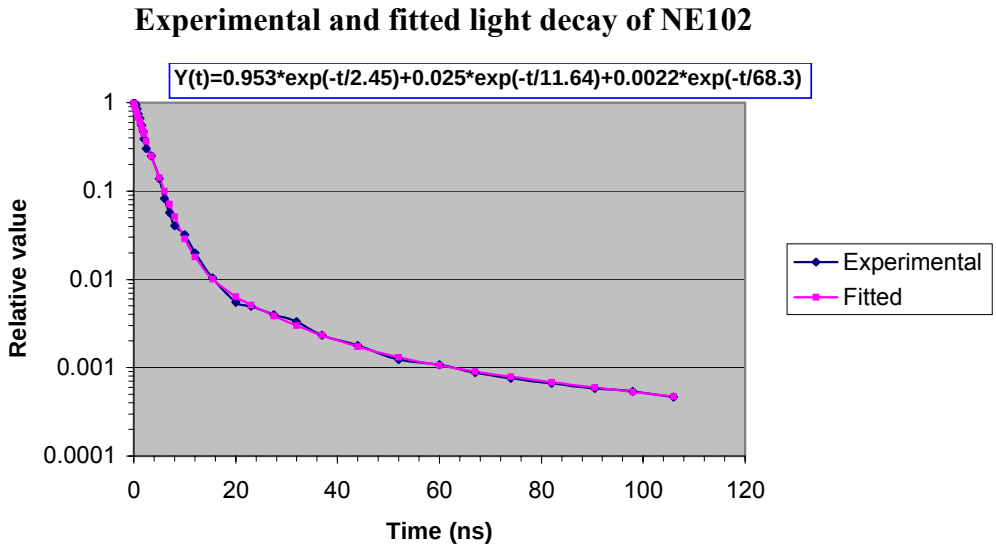

Fig. 3.7: Decay time of a typical plastic scintillator (NE 102) [106,107]

Hence, in order to maintain the spatial resolution independent of screen thickness, a screen constructed of **scintillating optical fibers** was used. A neutron-induced recoil proton loses its energy inside the fiber and produces scintillation. A fraction of this light travels along the fiber and is emitted at its ends. In this manner, the focus of the lens is permanently set on the front end (closest to the lens) of the fiber-screen and the spatial resolution is maintained independent of screen thickness.

The fiber screen is coupled to a highly reflective mirror (98% reflectivity made by Praezisions Glas & Optik GmbH), with the reflective side facing the fiber scintillator. This was done in order to collect also the scintillation photons emitted backwards, i.e. to the opposite direction from the lens.

In order to determine the distribution of energy deposited in the fibers and the amount of light created by the neutrons, we have performed a GEANT [56] simulation of the energy deposited by protons in a 0.5×0.5 mm^2 pixel of a fiber screen 200×200×20 mm^3 in dimensions [15]. In this simulation, the fiber screen was irradiated uniformly by neutrons incident normal to its face. Fig. 3.8 shows the distribution of the energy deposited by the

protons in the fiber. The average proton energy is **0.78, 2.44** and **3.22 MeV** for the 2, 7.5 and 14 MeV neutrons, respectively.

As can be observed the distribution approximates the flat shape only for the low energy neutrons, where the proton deposits most of its energy in the fiber. As the neutron energy increases the proton can escape the fiber and the energy is distributed in more than one fiber. Using the known entrance and exit energies of each proton in the fiber we have also calculated the number of light photons created in the fiber by the incident neutrons, using the non-linear proton-energy to-light conversion relation for a plastic scintillator (see fig. 3.9) [17].

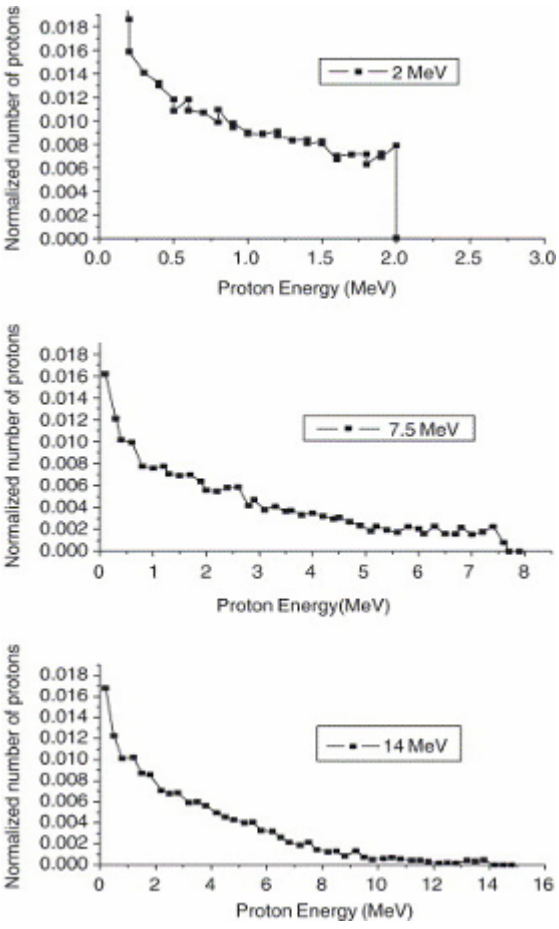

Fig. 3.8: Spectra of energy deposited by protons in 0.5×0.5-mm^2 fibers for 2 (top), 7.5 (middle) and 14 MeV (bottom) neutrons. The number of protons was normalized to the number of incident neutrons/pixel [14]

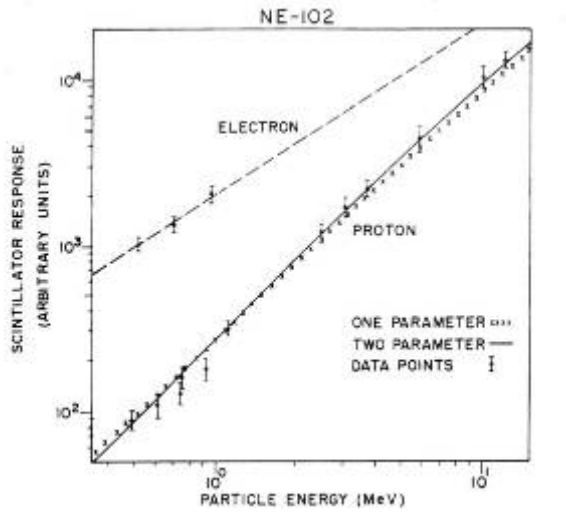

Fig. 3.9: Scintillation light yield for a common plastic scintillator (NE 102) when excited by electrons and protons [17]

The average amounts of visible light photons created in a single fiber were **2600, 10,600** and **17,400** for 2, 7.5 and 14 MeV neutrons, respectively.

As opposed to a slab scintillator in which the scintillation light is emitted into 4π, the light emitted from an optical fiber is limited to a cone, whose apex angle θ (*Numerical Aperture* ***NA***) is determined by the refractive indices n_1 of the core and n_2 of the cladding material respectively, according to [57]:

$$NA = \sin\theta = \sqrt{n_1^2 - n_2^2} \qquad [3\text{-}3]$$

In a typical single-clad plastic scintillating fiber the emission angle $\theta_{fiber\ max}$ is ~35° [58].

Figs. 3.10-3.12 show 3 scintillation screens. On the left, a 200×200 mm^2 scintillating fiber screen, manufactured by Saint-Gobain, USA. The screen is 30 mm thick and consists of 400×400 square polystyrene scintillating fibers, 500 ×500 μm^2 in dimensions. The middle image shows a 10 mm thick screen 120×120 mm^2 in area with round scintillating fibers, 250 μm in diameter. Scintillator slabs (Eljen, EJ-200 [52], polyvinyl toluene) of various thicknesses (seen on the right) were also used in order to compare image resolution to that obtained with the fiber screen.

Fig.3.10: A (20×20) cm^2 polystyrene fiber scintillator screen. Fiber diameter is 0.5 mm and screen thickness is 30 mm

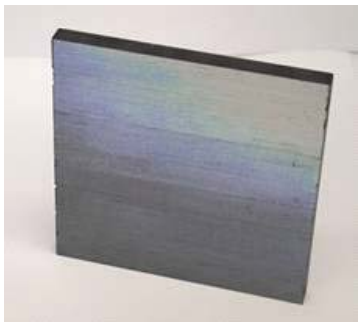

Fig.3.11: A (12×12) cm^2 polystyrene fiber scintillator screen. Fiber diameter is 0.25 mm and screen thickness is 10 mm

Fig.3.12: A (20×20) cm^2 polyvinyl toluene scintillator slab. Slab thickness is 20 mm

3.3.2 45° bending mirror

In order to protect the system components (CCD and image-intensifier) from radiation damage, the components were moved out of the neutron-beam flight path. Thus, a bending mirror was positioned at 45° facing the scintillator to deflect the scintillation light toward the F#=0.95 lens and onward.

The mirror (3.3 mm thick), manufactured by Praezisions Glas & Optik GmbH [59], is composed of a borosilicate substrate front-coated by a multi-layer dielectric thin-film. The mirror exhibits reflectance of >99% for single wavelengths (see fig. 3.13), high mechanical resistivity and high temperature stability.

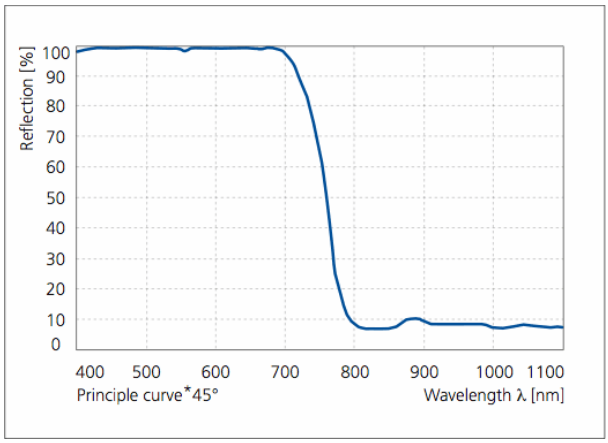

Fig. 3.13: Reflection curve as function of wavelength [105]

3.3.3 F#0.95 120 mm lens

The amount of scintillation-light emanating from the screen is not large. It is thus important to collect this light on an image intensifier as efficiently as possible. This is done with the aid of a large-aperture lens. The following calculation determines the efficiency of light collection using such a lens.

The plastic scintillating screen is not a typical thin *Lambertian source* that emits uniformly into 2π, but more like a transparent slab with a refractive index n_1=1.58 [52]. The light created by the neutron inside the slab (see fig. 3.14) can be considered as a point source emitting isotropically into 4π. If there is no reflector on the irradiated side, the light will travel inside the plastic toward the optical system and be refracted on its exit to air as shown on fig 3.14. The refraction will reduce the solid angle of the emitted light seen by the lens.

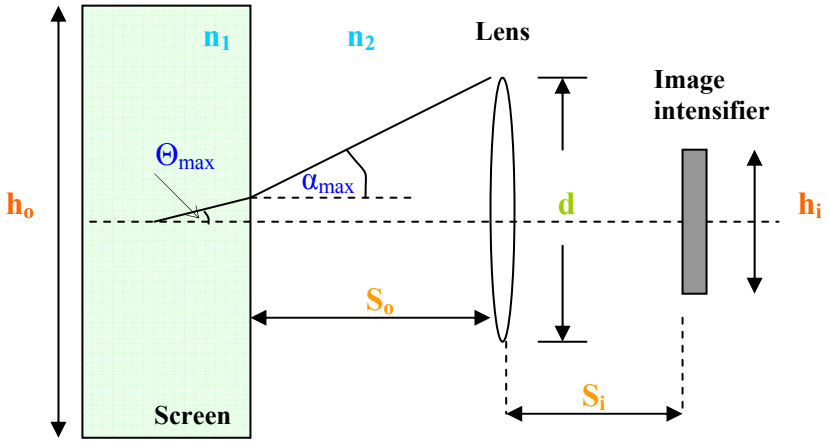

Fig. 3.14: Side view of the F#=1 lens. Top: cross-section view of the lens and image-intensifier coupling. Bottom: outside view of the lens

The fraction of the light emitted into the solid angle subtended by Θ_{max} out of the total into 4π is given by:

$$g = \frac{1}{2}[1 - \cos(\Theta_{max})] = \sin^2\left(\frac{\Theta_{max}}{2}\right) \qquad [3\text{-}4]$$

And for small angles (below 10^o):

$$g \cong \frac{1}{4}\sin^2(\Theta max) \qquad [3\text{-}5]$$

Θ_{max} is related to α_{max} by Snell's law:

$$\sin(\Theta_{max}) = \frac{n_2 \sin(\alpha_{max})}{n_1};\quad n_2(air) \cong 1 \Rightarrow$$
$$\sin(\Theta_{max}) = \frac{\sin(\alpha_{max})}{n_1} \qquad [3\text{-}6]$$

Therefore,

$$g \cong \frac{1}{4n_1^2}\sin^2(\alpha_{max}) \approx \frac{1}{4n_1^2}\tan^2(\alpha_{max}) \qquad [3\text{-}7]$$

By using the lens equation to calculate the focal length f, $\frac{1}{f} = \frac{1}{S_0} + \frac{1}{S_i}$ and magnification factor m, $m = \frac{S_i}{S_o}$ With $F\# = f/d$ and typical lens transmission T=0.85, we obtain:

$$g \cong \frac{T}{16n_1^2}\frac{m^2}{F\#^2(1+m)^2} \qquad [3\text{-}8]$$

7.5 MeV neutrons will produce protons with an average energy of 3.75 MeV. According to St-Gobain [58], polystyrene emits ~8000 photons per 1 MeV electron (e-) (as compared to 10,000 photons emitted by EJ-200). From fig. 3.9 [17] it can be deduced that a 3.75 MeV proton will yield the same number of scintillation photons as a ~1.325 MeV electron. Thus, for a 7.5 MeV detected neutron the average number of scintillation photons created (in polystyrene) is about 10,600.

In our system the screen size is 200 mm and the image intensifier diameter is 40 mm, hence ***m***=0.2, the refractive index n_1 of the polystyrene fiber scintillator is 1.6 [58] (1.58 for EJ-200 [52]) and the distance between the screen and the lens was chosen to be 750 mm.

In order to collect at least 20 photons/neutron, the collection efficiency should be:

$$g = \frac{Number\ of\ required\ photons}{Number\ of\ photons\ created\ per\ fast\ scintillation} = \frac{20}{10600} = 0.00189$$

For the geometry presented in this work, this efficiency leads to a lens with an *F#*=0.56, the focal length would be *f*=125 mm and the lens diameter would be 227 mm. Large diameter, low *F#* lenses are very expensive and require custom design. A reasonable compromise is to choose a lens with a focal length *f*=120 mm and diameter of 126 mm resulting in *F#*=0.95.

The light from the fiber is emitted into a cone with an apex angle of 35.45° [58], as shown in fig. 3.15 below:

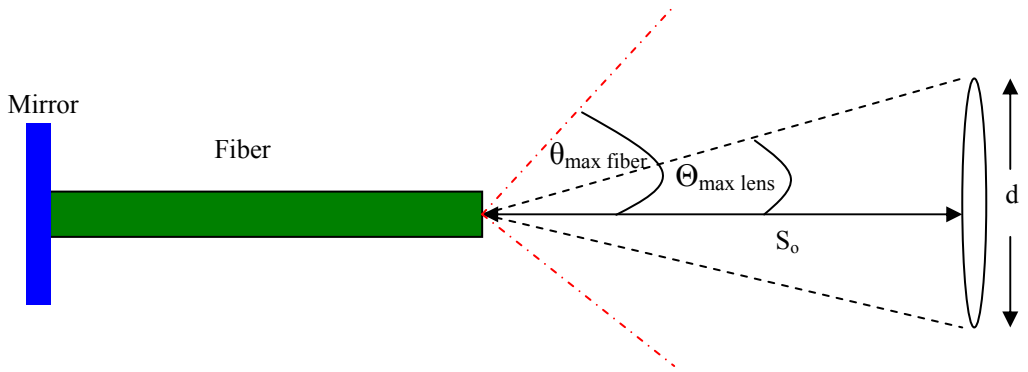

Fig. 3.15: Schematic description of light emission from a fiber scintillator

The angle subtended by the lens positioned at a distance S_o from the end of the fiber is:

$$\theta_{max\ lens} = arctg(d / 2S_o) \qquad [3\text{-}9]$$

The light emitted by the fiber is collected through the lens with the following efficiency:

$$g = T \cdot \frac{(1 - \cos\theta_{max\ lens})}{(1 - \cos\theta_{max\ fiber})} \qquad [3\text{-}10]$$

For a lens diameter of 126 mm and fiber-to-lens distance of 750 mm, $\theta_{max\ lens}$= 4.8°, $\theta_{max\ fiber}$ is 35.45° and *T*=0.85, hence, *g*=0.016.

In a square scintillating fiber, only 4.4% of scintillation photons will travel to each end of the fiber via total internal reflection [58]. By coupling a good quality mirror to the opposite end of the fiber we can reflect back the photons which are traveling in the direction away from the lens and get a maximum 8.8% of the scintillation photons.

Thus the maximal number of photons reaching the image intensifier per one neutron will be:

$$N_{photons}=\mathbf{10600 \times 0.088 \times 0.016 = 14.9\ photons/neutron}$$

Due to the fact that such a lens was not commercially available, it had to be specially designed by a professional lens designer. A schematic view of the lens is shown in Fig. 3.16.

The lens consists of 5 elements, 3 positive and 2 negative. Its effective focal length is 120 mm, *F#* is 0.95 and its entrance pupil diameter is 126 mm.

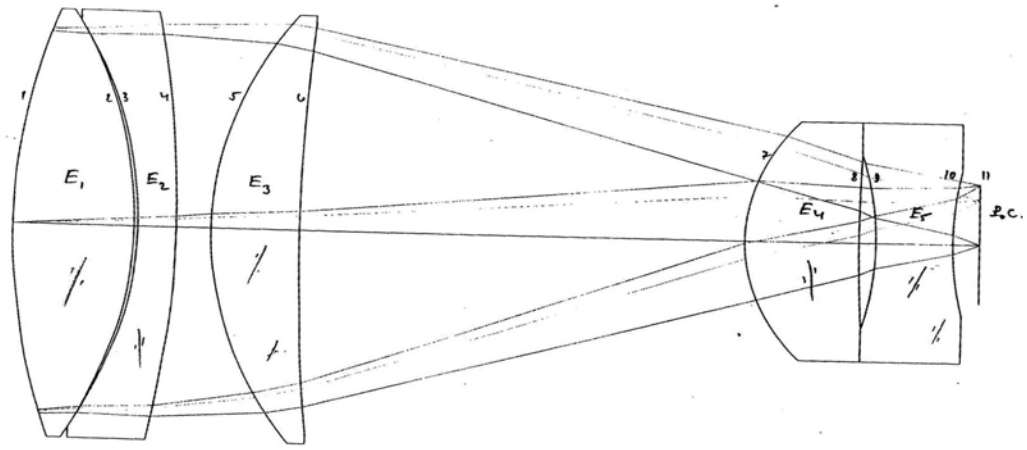

Fig. 3.16: Schematic drawing of the collecting F#=1 lens

The lens elements were specially manufactured by A. Optical Components Ltd., Azur, Israel and the lens was assembled in Soreq NRC. figs 3.17, 3.18 show the engineering illustrations of the assembled lens.

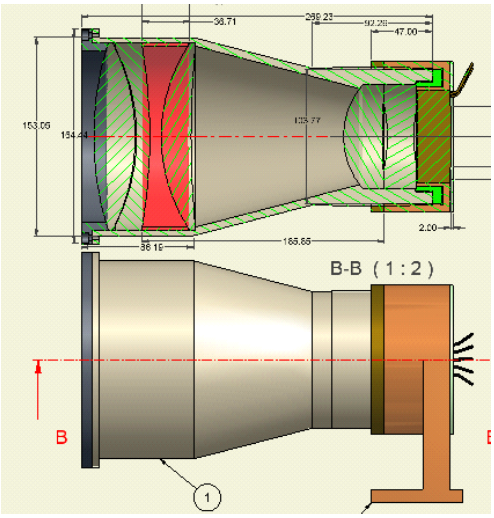

Fig. 3.17: Side view of the F#=1 lens. Top: cross-section view of the lens and image-intensifier coupling. Bottom: outside view of the lens

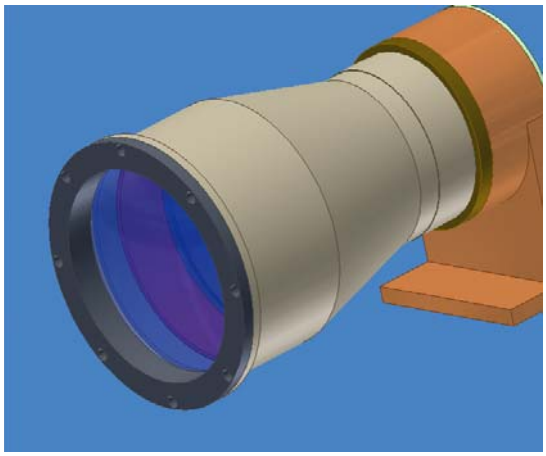

Fig. 3.18: A general view of the F#=1 lens

3.3.4 Image intensifier (I-I)

Energy selection via the time-of-flight technique is enabled by gating the image intensifier (I-I) on a ns scale. The image intensifier acts as a very fast optical shutter, synchronized with the accelerator pulses and triggered to open after certain delay time that corresponds to a specific pre-selected neutron energy. As can be seen in fig. 3.17, an image intensifier is a vacuum tube device comprised of a photo-cathode input, single or multiple Multi-Channel Plates (MCP) and a phosphor screen. A detailed description of the principle of operation of the I-I and its components is given in appendix 2.

When the photocathode is biased more positively than the MCP, electrons will not enter the MCP and the MCP is gated off. If the photocathode is negatively biased, electrons will be accelerated towards the MCP and the intensifier is gated on.

As illustrated in fig. 3.19, a portion of the incident light photons striking the photocathode cause the release of electrons via the *photoelectric effect*[*]. These electrons are then accelerated (by a voltage of about –150 V) towards the MCP, where they are multiplied and accelerated again (under voltage of +3900 V) toward the phosphor screen.

[*] The *photoelectric effect* represents the emission or ejection of an electron from the surface (the photocathode in this case) in response to an incident photon of sufficient energy to overcome the binding energy of the electron

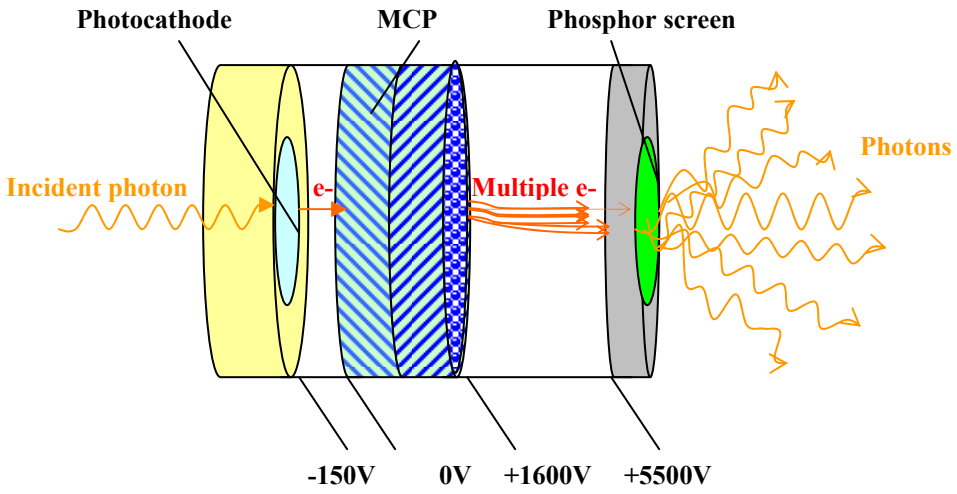

Fig. 3.19: Schematic description of an image intensifier (not to scale). An incident light photon striking the photocathode causes the release of an electron via the photoelectric effect. This electron is accelerated towards the MCP, where it is multiplied and accelerated again toward the phosphor screen. These electrons strike the phosphor screen, causing the emission of fluorescence photons

The electrons striking the phosphor screen cause the emission of fluorescence photons. Thus, for every photon releasing an electron from the photocathode, a larger number of photons (by several orders of magnitude) is emitted from the phosphor screen.

The image-intensifier (MCP240) [60] employed here, seen in figs. 3.20a and b, was manufactured by PHOTEK Limited, UK, as a high-gain, proximity-focus device. The tube is about 25 mm in length and 40 mm in diameter with a rugged metal ceramic construction. Two micro-channel plates enable a gain of 10^6 W/W. The input window is made of fused silica and the output window is made of fiber optic and a P43 phosphor screen. The photocathode is a low noise S20 with maximum sensitivity at 450 nm. Its limiting resolution is 20 lp/mm.

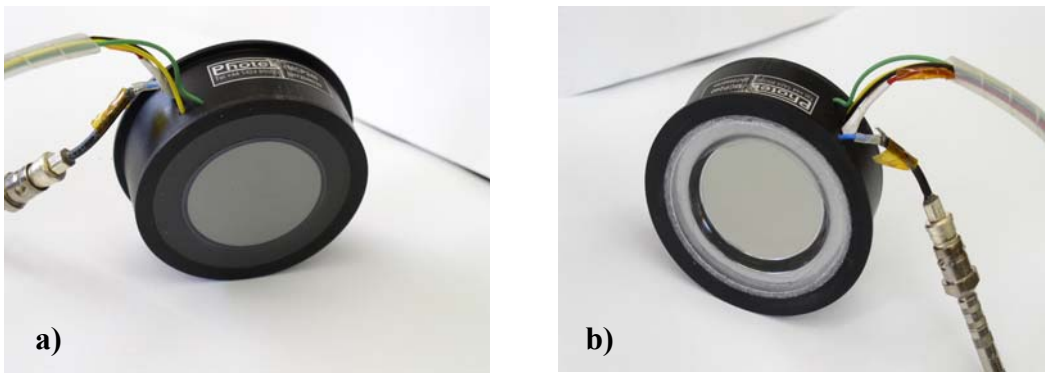

Fig. 3.20: The MCP 240 image-intensifier a) Rear view, the bright circle in the center is the phosphor screen, b) Front view, the bright circle at the center is the photo-cathode

The spectral response of the image-intensifier S-20 photocathode is displayed in fig. 3.21. The maximal sensitivity is 47.26 mA/W at 450 nm, which corresponds to quantum efficiency QE of about 13%. This is rather low compared to the 20-25% obtainable with vacuum photo-multipliers at this wavelength.

The relatively low QE of the photocathode is due to the method of the cathode preparation aimed to reduce the *irising* [61] effect at nanosecond gating.
Since the photocathode has a small electric conductivity, it will take the high voltage gating pulse a finite time to travel from the edge of the intensifier to the center. Therefore, there will be a delay for the center to switch on/off relative to when the edge switches on/off. This delay is referred to as *irising*.

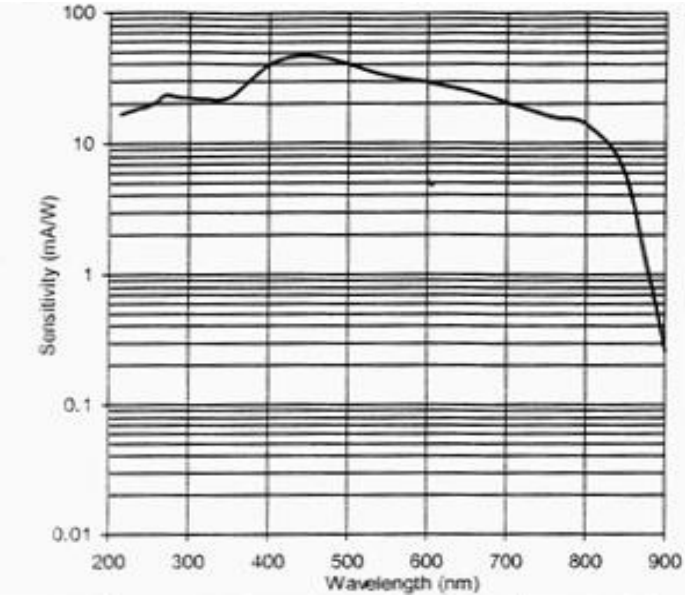

Fig. 3.21: Spectral response of the LN S20 photocathode present in the TRION system

Many of the photocathode materials used in image intensifiers are not highly conductive and therefore, in order to achieve faster gate speeds, a Ni mesh undercoating is laid down on the inside surface of the input window beneath the photocathode. This absorbs ~30% [61] of the incoming photons before they strike the photocathode. The minimal gate width that can be applied to the photocathode for full I-I opening was determined experimentally to be about 8 ns (see chapter 4).

Using the figure of 13.4 photons/neutron reaching the I-I (see section 3.3.3) and QE of 13%, the average number of photoelectrons produced by a 7.5 MeV neutron will be about **1.7 photoelectrons/neutron**.

3.3.4.1 Timing and gating of the I-I

In order to perform TOF measurements, the I-I photocathode has to be biased at a precise delay and width following the accelerator burst. For this purpose, a computer controlled Gate and Delay Generator (G&DG) and a fast HV pulser were custom developed. The G&DG was developed and built at PTB, Germany and the HV pulser was purchased from Roentdek.

Fig.3.21 shows a block diagram of I-I pulsing (top) and the pulsing regime (bottom) [62].

The G&DG is a single NIM module (see fig. 3.22) computer-controlled via RS232 port. Its input is a TTL pulse from the accelerator, providing a TTL output which feeds into 50 Ω of the HV pulser. The gate and delay widths can be obtained in coarse time steps of 8 ns, derived from a 125 MHz clock. The fine tuning is realized by digital delay lines providing steps of 0.25 ns. To avoid a time jitter between the G&DG clock and the cyclotron pulse, the 125 MHz clock was phase-locked to the cyclotron frequency.

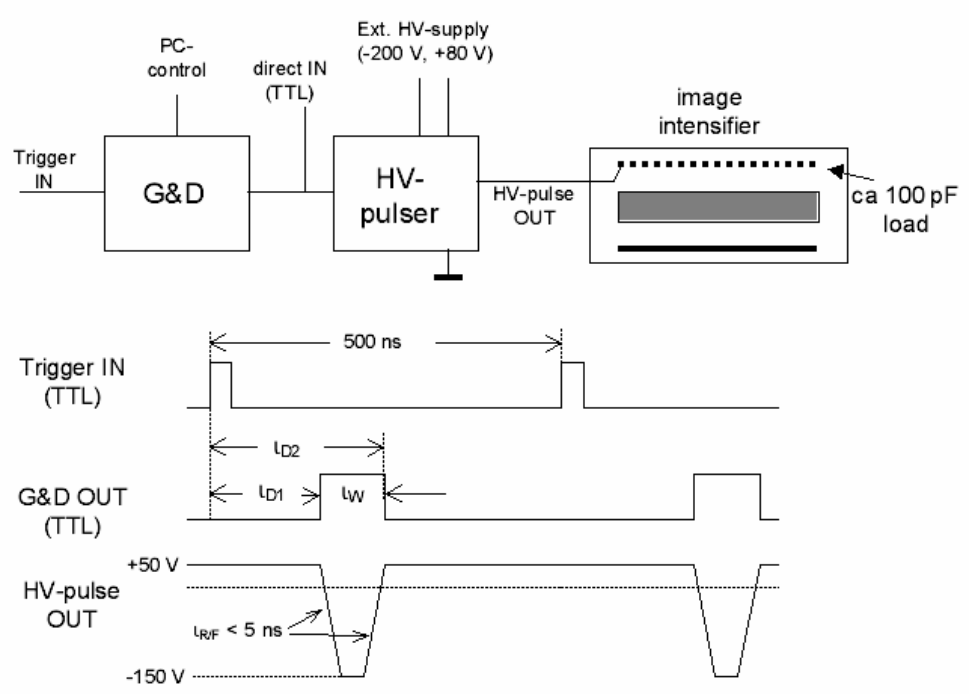

Fig. 3.22: Block diagram of I-I pulsing (top), and pulsing regime (bottom). Delays: L_{D1}, L_{D2}, gate width: $L_w = L'_{D2} - L_1$

The Roentdek HV pulser is triggered by a TTL pulse from a G&DG [63]. The output switches the photocathode voltage between +50 V (I-I-off) and –150 V (I-I-on) with rise time of 2-5 ns (depending on the capacitive load). The high switching frequency (2 MHz) and the large capacitance of the Field-Effect-Transistor (FET) and FET pulser-driver cause significant heating due to high power deposition (about 30 W). This heat is removed by

coupling the pulser box to a water cooled copper block, refrigerated to 5-10 ^{o}C. An image of the pulser mounted in the system is shown in fig. 3.23.

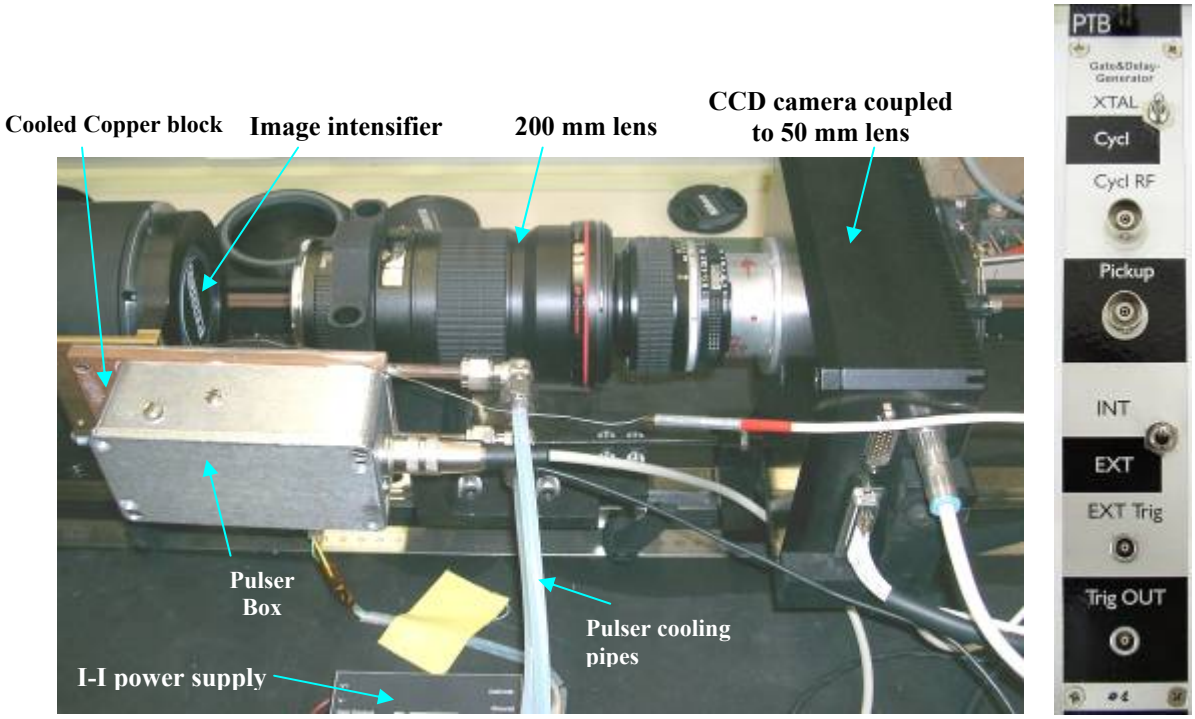

Fig. 3.23: Images of the pulser (left) mounted next to the image intensifier and the gate and delay generator (right)

3.3.5 Tandem lenses

A 200 mm F#=2.8 Canon lens is positioned behind the image-intensifier. This lens is used to relay the image created at the intensifier's phosphor to the CCD via the Nikon 50 mm lens. As can be seen in fig. 3.23, the 200 mm lens is mounted backwards, i.e. the bayonet end faces the image intensifier, while the front end faces the 50 mm lens (coupled to the CCD camera). In this manner, the rear end of the 200 mm lens is focused on the phosphor, thus transporting a parallel beam of light to the 50 mm lens. The 50 mm lens demagnifies the image to the CCD sensor dimensions, as illustrated in fig. 3.24.

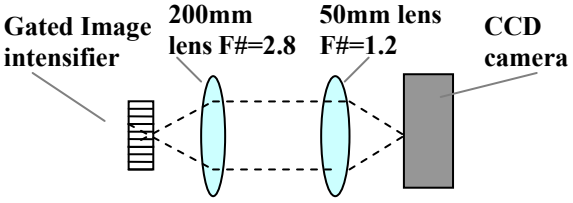

Fig. 3.24: Schematic diagram of relay lenses operation principal

This configuration was chosen due to the fact that it provides greater light transmission efficiency by more than a factor of 4 compared to a single lens configuration [64].

However, it also introduces a *vignetting* effect. In an optical system, vignetting [65-66] produces a gradual reduction of image illuminance as the off-axis angle increases. This may arise from failure to capture some of the peripheral rays by the second lens. Fig. 3.25 illustrates an example [67] of a similar tandem configuration (not to scale) where some of the peripheral rays are not captured by the second lens.

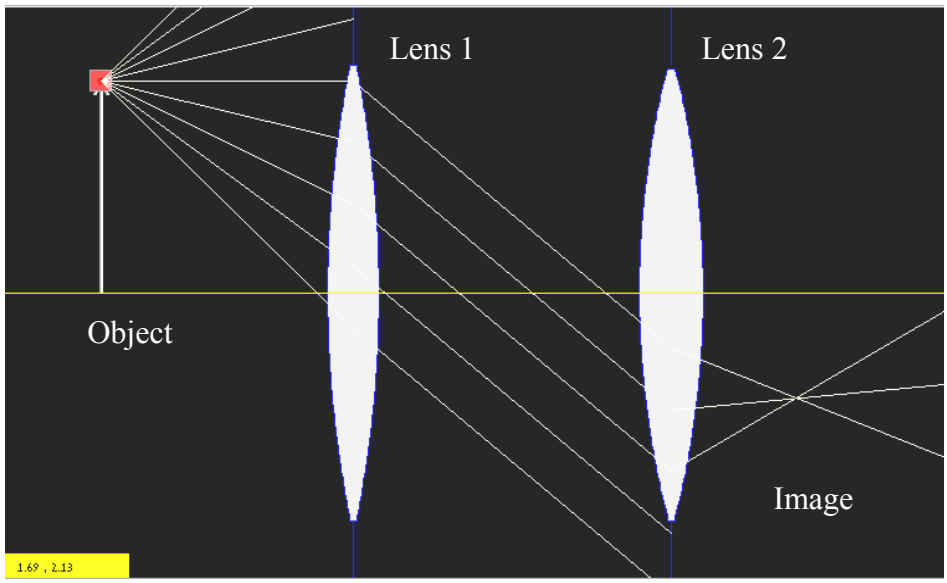

Fig. 3.25: An example [114] (not to scale) of vignetting effect introduced by a tandem configuration, similar to the one presented in this work

3.3.6 Charge Coupled Device – CCD camera

The CCD camera used in this work, Chroma C3 (see fig. 3.26), was manufactured by DTA Scientific Instruments, Pisa, Italy. The CCD sensor housed in the camera, KAF 1602E [68-69] (manufactured by Kodak), is comprised of 1024 (H) × 1536 (V) photoactive pixels of 9 μm×9 μm in dimensions. Each pixel has a Full-Well Capacity (FWC) of 100,000 e- and dark current level of ~0.623 e-/sec (with gain of 5.4 V at -5.2^{o} C) [70]. The analog signal is digitized by an Analog-to-Digital converter (A/D) of 14 bits, providing a dynamic range of 16384 gray levels. The overall photosensitive area of 13.8 mm (H) × 9.2 mm (V) can be cooled down to -40 ^{o}C (below ambient temperature) by a Peltier cooler.

The camera can be controlled via the computer using the Vista management software (programmed by DTA) or by a specifically written program which utilizes the Vista

drivers. A detailed description of the principle of operation of the CCD is given in appendix 3.

Fig. 3.26: CHROMA C3 camera used to house the KAF1602E CCD sensor

Chapter 4

4. Experimental configuration

4.1 Experimental facility at PTB, Germany

The performance of the TRION detector was tested with a ns-pulsed (beam-burst ~1.5ns wide, pre-selectable repetition rate in MHz range), variable-energy neutron beam produced by the PTB cyclotron. The PTB neutron irradiation facility (shown on fig. 4.1 [26]), houses a rotatable CV28 compact cyclotron manufactured by TCC (The Cyclotron Corp)., USA (seen in position 2). In addition, the PTB facility houses a 3.75 MeV Van-de-Graaff accelerator (position 1) for low energy ion and neutron beams, also capable of providing 1 ns beam pulses.

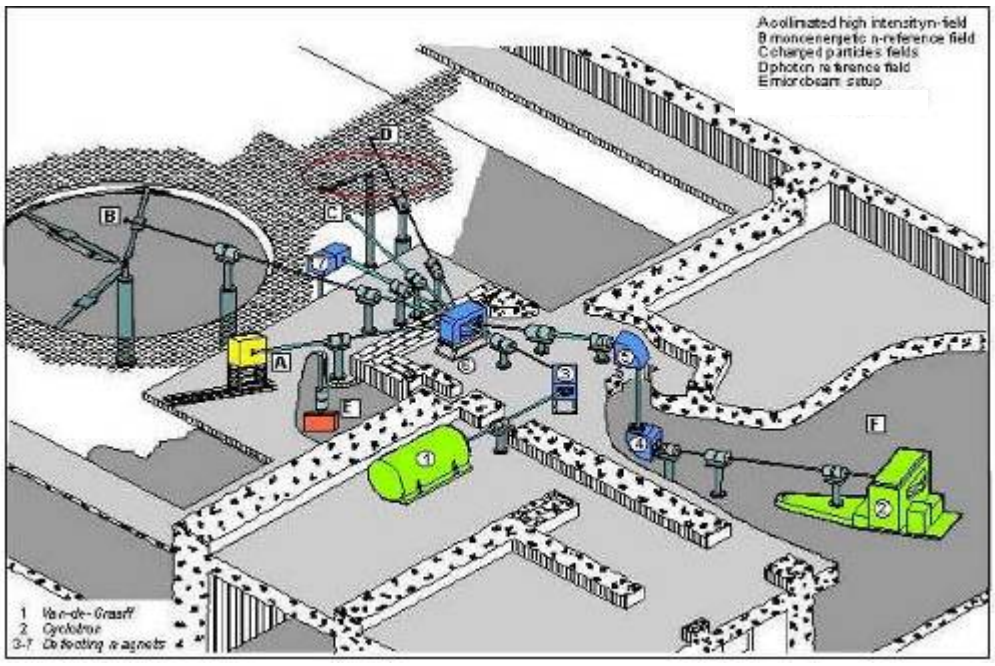

Fig. 4.1: Layout of the cyclotron facility at PTB [33]. Position 1: 3.75 MeV Van-de-Graaff accelerator, position 2: CV28 compact cyclotron, positions 3-7: bending magnets

The cyclotron is equipped with a fast internal beam-pulsing system, that provides the capability to choose between a wide range of pulse repetition rates, 2 kHz to 6 MHz [25]. The actual rate had to be restricted to 2 MHz (500 ns separation between consecutive pulses) in order to prevent the most energetic neutrons produced in a particular beam burst from arriving at comparable times to the less-energetic neutrons produced in the preceding pulse.

The cyclotron is located on the lowest floor of the facility, along with a sophisticated low-scattering collimation system defining 5 different neutron beam-lines, each consisting of a set of massive polyethylene, water and concrete collimators combined with steel (seen in figs. 4.2 & 4.3). Our setup was located at 0^{o} or 25^{o} to the incident deuteron beam.

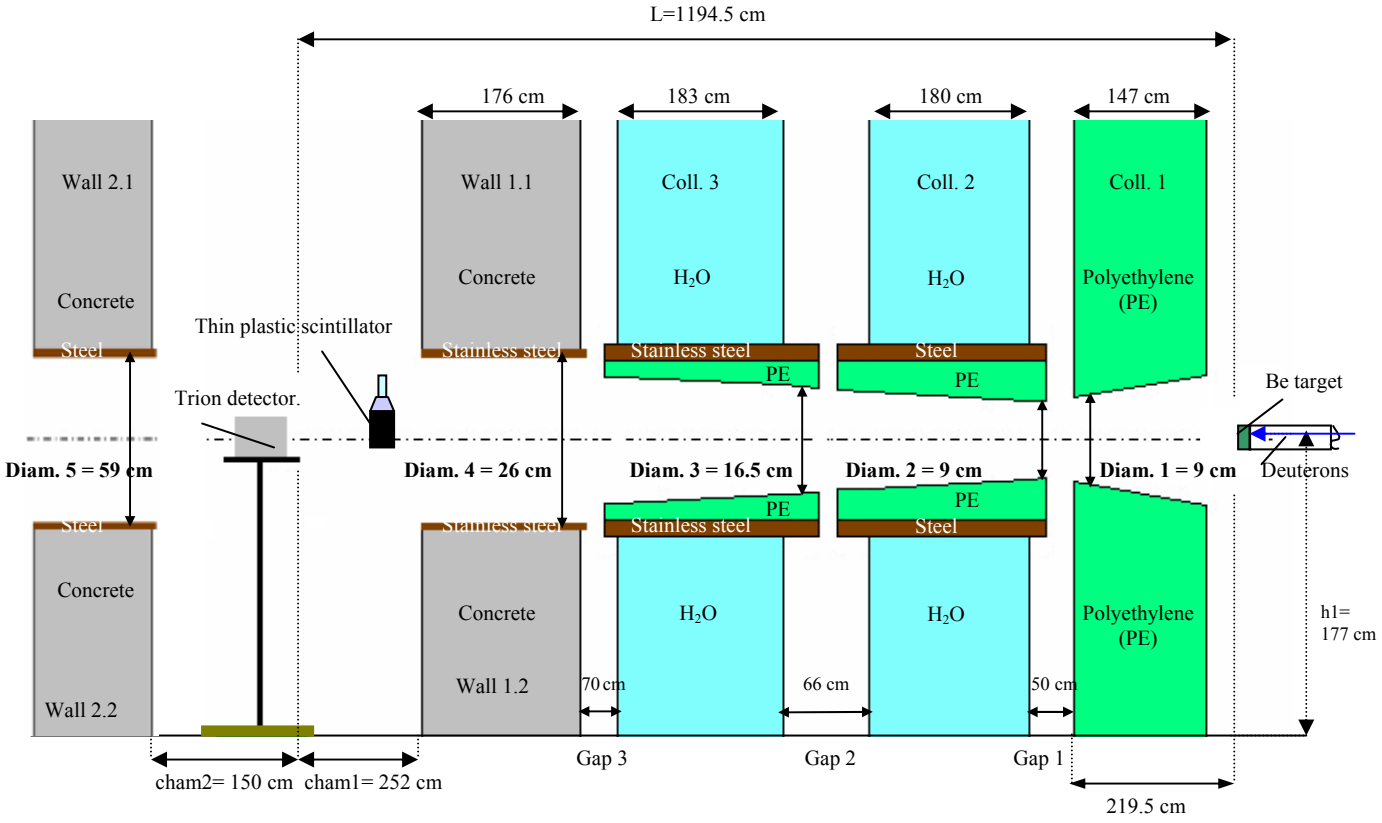

Fig. 4.2: Cross-section schematic diagram of the PTB experimental setup (not to scale) for the 0^{o} beam-line

The detector was positioned at a distance of 1194.5cm from the target.

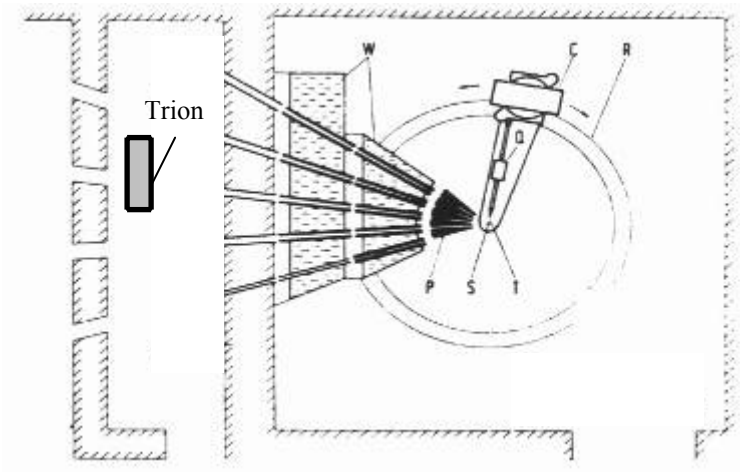

Fig. 4.3: Schematic top-view layout of the PTB experimental geometry. C- Cyclotron, R- rails, Q- quadrupole magnet, T-Be target, S- scattering probe, P- polyethylene collimators, W- water tank [115]

Two types of neutron spectra were employed in this experiment:

- A broad-energy neutron spectrum produced by 13 MeV deuterons impinging on a thick (2-3 mm) solid Be target
- A mono-energetic neutron spectrum produced by 9.7 MeV deuterons impinging on a deuterium gas target

As mentioned earlier, the neutrons were produced in 1.5 ns bursts with repetition frequency of 2 MHz. In several experiments the frequency was reduced to 1 MHz to reduce neutron frame overlap. The average deuteron beam current at 2 MHz was 1.5-2 μA. Figs. 4.4a & b display an image of an air-cooled Be target used at PTB and a schematic layout of the target arrangement [25], repectively.

In front of the Be target a capacitive beam target pickup was installed, in order to derive the timing signal for the TOF measurements.

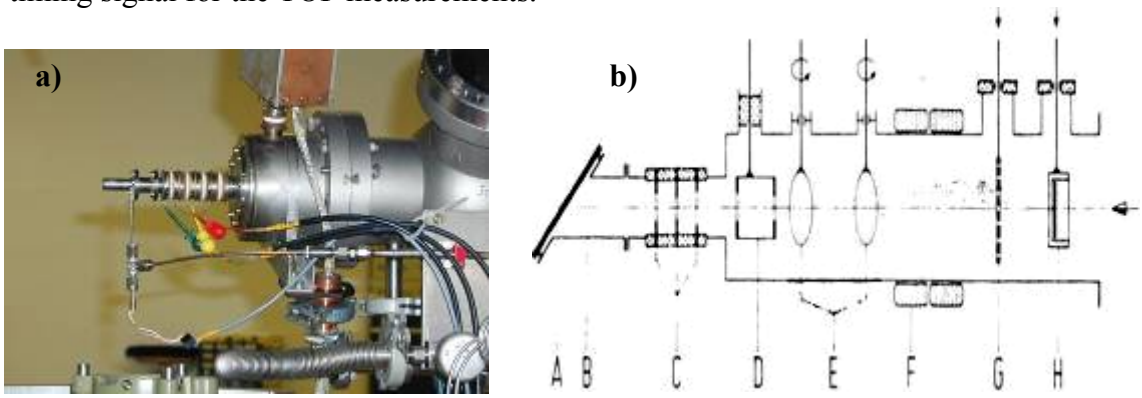

Fig. 4.4: a) Air cooled Beryllium target, and b) schematic layout of the target arrangement [74]. A - Be disc, B - rotatable target support, C - defining apertures, D - beam pickup unit, E - rotating beam scanner, F – quadrupole lenses, G – aluminium grid, H – Faraday cup

The deuteron beam structure was determined with the help of a Cerenkov detector positioned at a large distance (approximately 30 meters from the target). This detector, which has low sensitivity to neutrons, measures the flash of gamma rays emitted during the deuteron interaction with the target. Fig. 4.5 shows the TOF spectrum measured with the Cerenkov detector.

The spectrum was time-calibrated by adding a 20 ns delay-cable to the TAC stop signal. The 20 ns addition shifted the peak by 400 channels, so the calibration was 0.05 ns/ch. As can be observed, the gamma burst consists of a main peak (FWHM of 2.6 ns) followed by a satellite peak (~3 ns separation between peaks). Using the single-electron-response of a

Photo-Multiplier (PM), the deuteron burst FWHM was estimated to be 1.7 ns. The temporal resolution will be addressed in more detail in chapter 5.

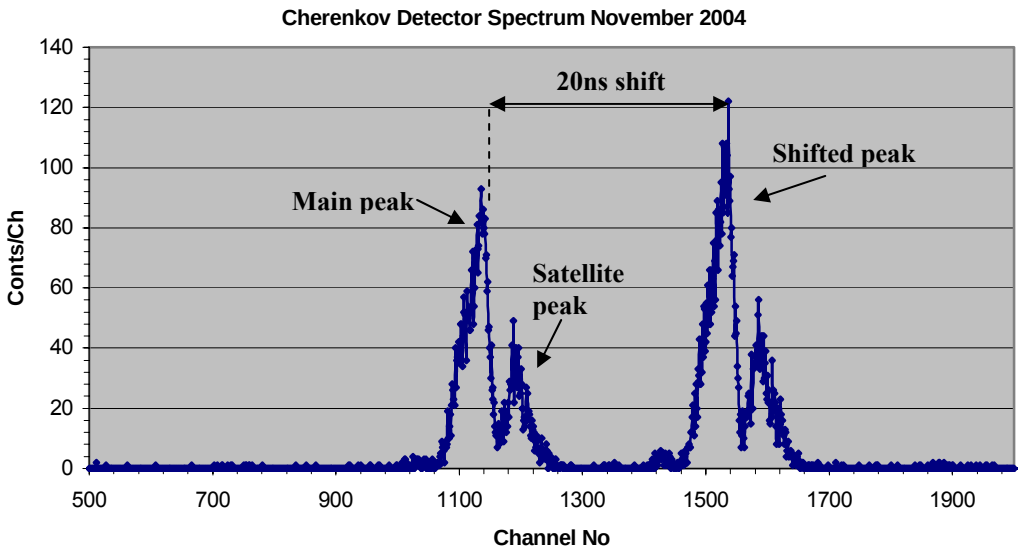

Fig. 4.5: The spectrum obtained from a Cerenkov detector

To permit a measure of neutron spectra by event-counting time-of-flight spectroscopy, a thin NE102 plastic scintillator coupled to a PM (shown on fig. 4.6) was positioned on a motorized movable stand, at a distance of ~1000 cm from the target. The scintillator could be inserted into the neutron beam as desired.

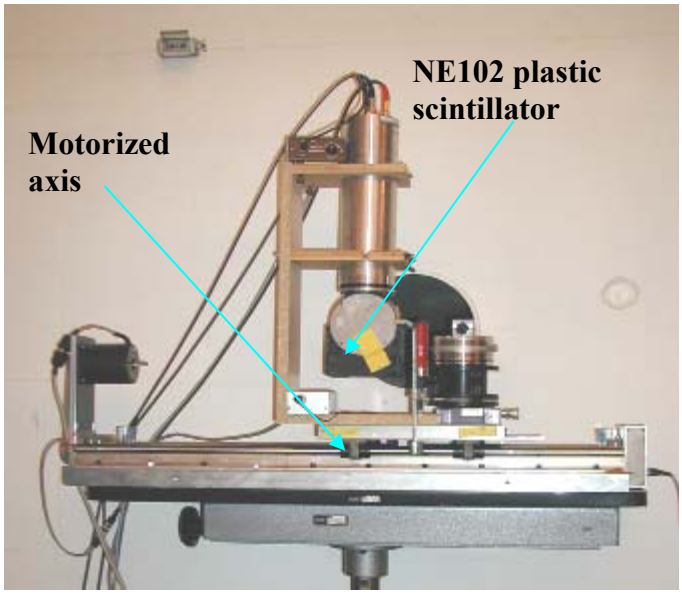

Fig. 4.6: NE102 plastic scintillator attached to a movable stand, positioned inside the neutron beam path

4.2 Neutron spectra and flux

Fig. 4.7 displays a TOF neutron spectrum as measured by the NE102 scintillator/PM.

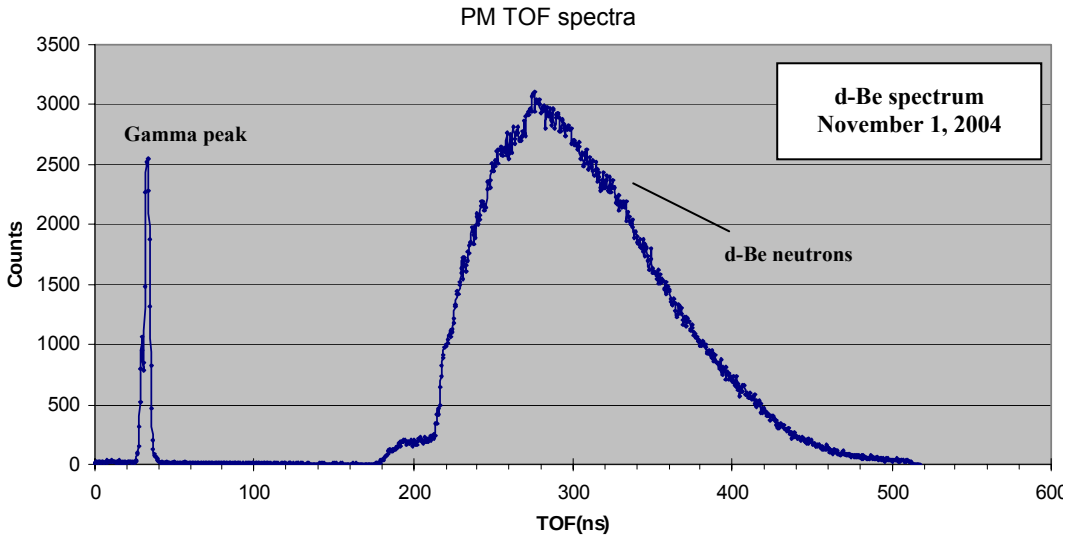

Fig. 4.7: TOF d-Be spectrum obtained with plastic NE102 scintillator

The peak on the left hand side is the gamma-ray flash from the d-Be reaction. The fastest neutrons arrive ~150 ns after the gamma-rays. Obviously, this spectrum is affected by the detection-efficiency; hence, in order to determine the true neutron spectrum emitted from the target, it is necessary to take the detection efficiency into consideration.

Figs. 4.8a and b show the true d-Be neutron energy spectrum (for three deuteron energies, 9.43, 10.87 and 13.54 MeV) and angular dependence of the total neutron yield per unit beam charge, respectively, as measured by Brede et al. [25]. At an emission angle of 0^{o}, the total reaction yield is 2.6×10^{10} n/(s·sr·μA). This produces a neutron flux of 1.8×10^{4} n/s·cm^2 per μA on a detector positioned at a distance of 12 m from the target.

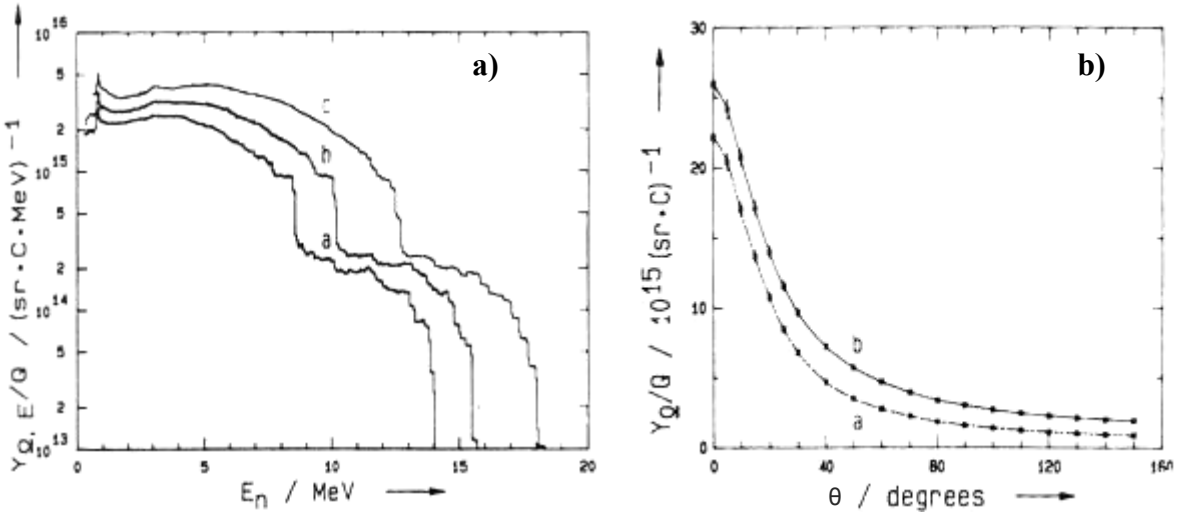

Fig. 4.8: a) Spectral neutron yield per unit beam charge $Y_{\Omega,E}(0^{o})/Q$ for a thick Be target bombarded with deuterons of various energies E_d. Curve (a) corresponds to E_d=9.43 MeV, curve (b) to E_d=10.87 MeV and curve (c) to E_d=13.54 MeV. b) Angular dependence of the total neutron yield per unit beam charge Y_{Ω} (θ)/Q, of the d-Be reaction for deuteron energy of 13.54 MeV and two recoil proton energy thresholds E_{th}. Curve (a) corresponds to E_{th}= 400 keV and (b) to E_{th}= 2 MeV [74]

As mentioned previously, the d-D reaction was also employed as part of the TRION system evaluation at PTB. Fig. 4.9 shows a d-D spectrum obtained with 9.7 MeV deuterons, producing 12.16 MeV neutrons.

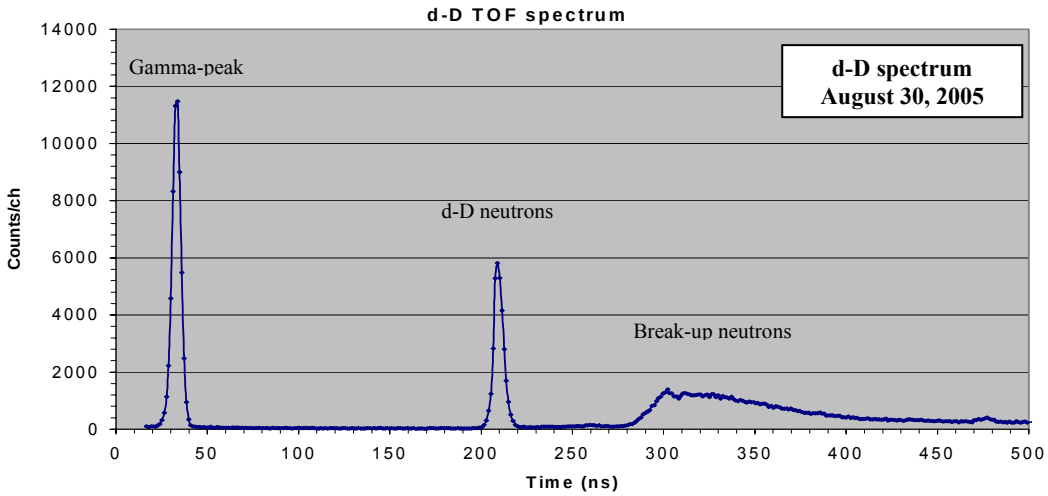

Fig. 4.9: TOF spectrum of d-D reaction

In addition to the main 12.16 MeV peak there are some lower energy neutrons due to deuteron breakup.

4.3 Simulation of beam transport

The measured spectra, shown in fig. 4.9, may contain other events than fast neutrons emitted directly from the target. These are primarily neutrons scattered by the collimators, as well as gamma-rays produced in the collimation system by inelastic neutron scattering and neutron capture. In order to determine their contribution and time behavior, the experimental setup (shown in fig. 4.2) was simulated using the GEANT code [56].

All simulations used a cone-beam of 12.16 MeV mono-energetic neutrons emitted from a point source, air humidity of 55%, neutron energy cutoff of 12 keV and beam opening angle of 9^{o} (as illustrated in fig. 4.10).

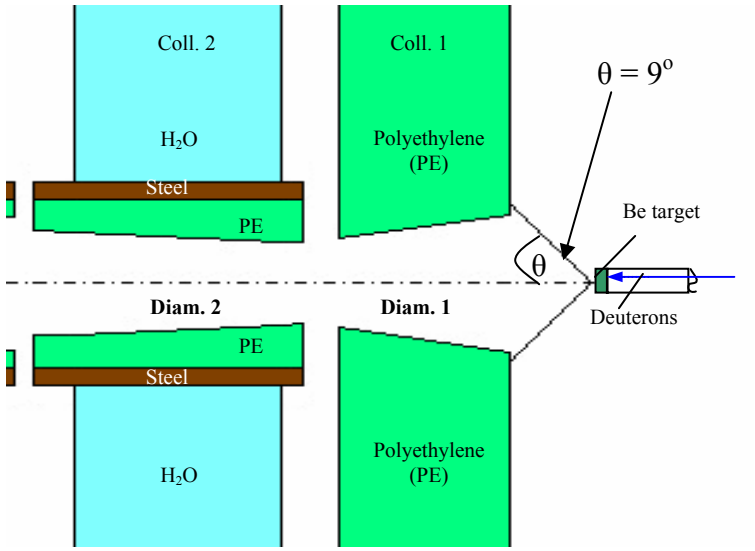

Fig. 4.10: A section of the collimation system with neutron beam opening angle of 9°

4.3.1 Influence of scattered neutrons

Figs. 4.11 & 4.12 describe the simulated energy spectrum and TOF spectrum of the scattered neutrons entering the detector, respectively. The ratio of the scattered neutrons to the direct ones (all neutrons which enter the detector) is 2.5×10^{-3}. This small ratio is clearly a result of the efficient PTB neutron low-scattering collimation system (see section 4.1), implying that neutrons scattered by the collimation system will not constitute a significant source of image degradation.

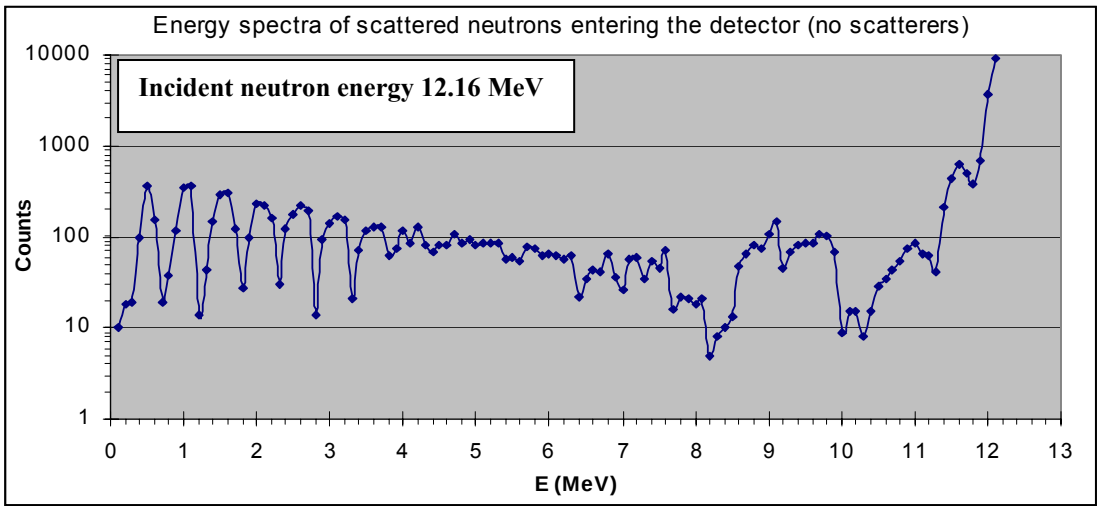

Fig. 4.11: Energy spectra of scattered neutrons entering the detector. Incident neutron energy – 12.16 MeV

The oscillations seen in the lower energy region of the spectrum (0-4 MeV) are not explained and require further investigation.

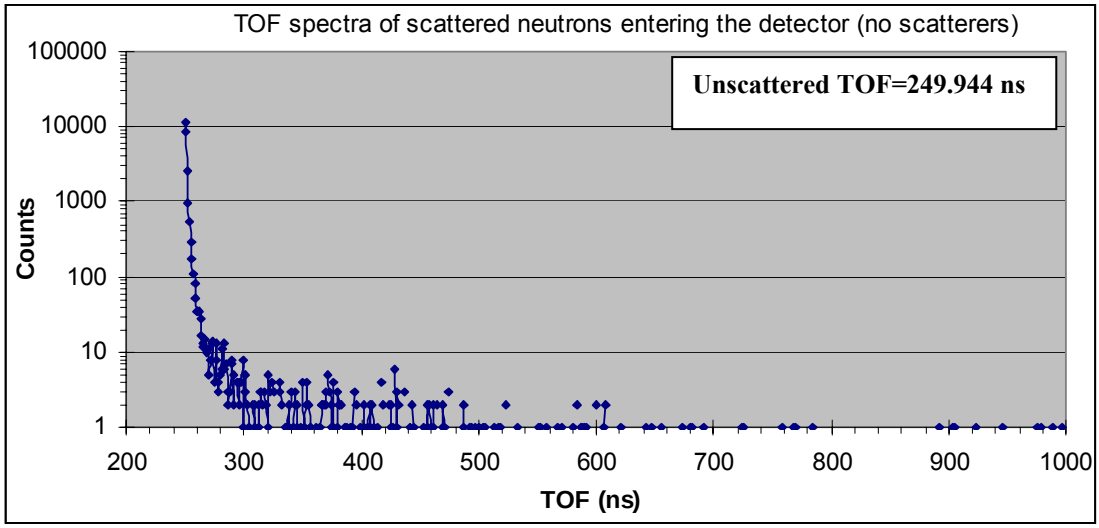

Fig. 4.12: TOF spectra of scattered neutrons entering the detector

4.3.2 Gamma ray background

The number of neutron induced gamma photons entering the detector was also simulated (fig. 4.13). The ratio of gamma photons to the number of direct neutrons (all entering the detector) is 4.7E-3. This rather low ratio, does not take into account gamma rays produced by neutrons of energies lower than 12 keV (due to the fact that GEANT 3.21 has a cutoff limit of 10 keV).

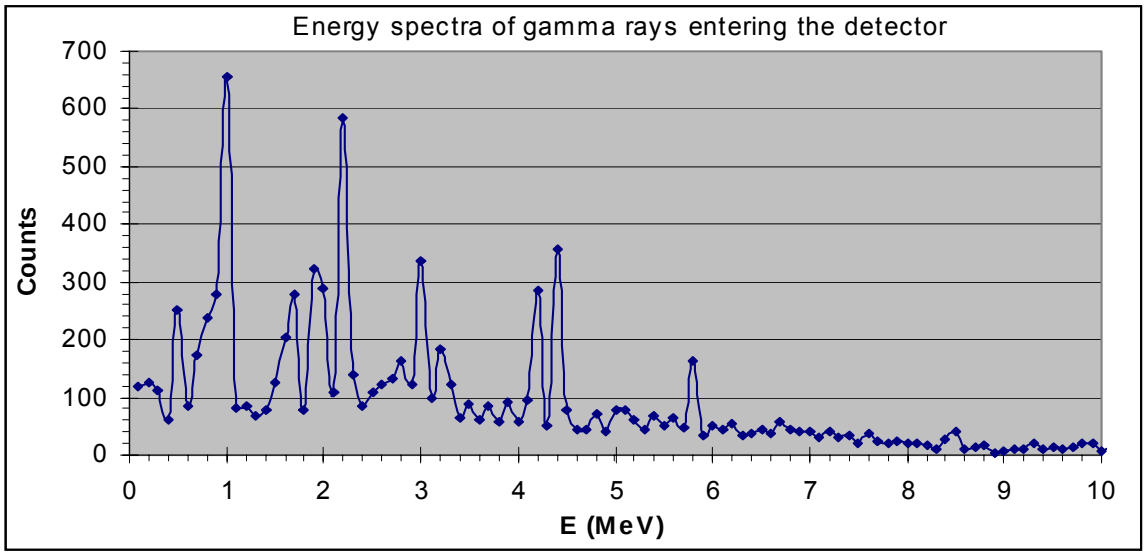

Fig. 4.13: Energy spectra of gamma rays entering the detector

From these calculations, it can be concluded that the number of neutrons and gamma-rays which contribute to the background is negligible.

Chapter 5

This chapter deals with the determination of the basic parameters of the detection system such as position resolution, timing resolution screen properties and the various factors that influence image quality.

5.1 General comments and definitions

The in-beam experiments at PTB were conducted in two separate rounds, the first in November 2004 and the second in August 2005. After the first round, the following improvements were made on the TRION system: the scintillating fiber screen (12×12×1 cm^3) was replaced by a larger and thicker one (20×20×3 cm^3), the I-I photocathode gating pulse was shortened from ~20 ns to ~10 ns and external cooling was applied to the CCD camera. Table 5-1 summarizes the principal performance differences between the two rounds of experiments.

Table 5-1: Principal performance differences in the two PTB runs

	Fiber-scintillator dimensions (H×W×T) (mm)	**individual fiber diameter (µm)**	**CCD cooling temp. (^oC)**	**I-I Gating pulse width (ns)**
1st round	120×120×10	250	-5	~20
2nd round	200×200×30	500	-17	~10

The following experiments were performed during the two rounds and will be described in detail in this chapter:

- Dependence of image quality on screen type and thickness
- Dependence of image quality on neutron energy
- Timing properties of the detector

In order to obtain a normalized net neutron image we have to collect four independent images:

1. Gross image ($\boldsymbol{Im_{gross}[t]}$)

This is an image taken with the neutron beam on. Its light signal per pixel consists of the sum of the net neutron signal, the dark current (originating from CCD and from image intensifier) and the read-out noise ($\boldsymbol{RN}$). A detailed description of various sources of noise is given in appendix 4. To the best of our understanding, the neutron-induced signal in any pixel ($\boldsymbol{x,y}$) is dependent on exposure time $\boldsymbol{t_{im}}$ and the integrated deuteron beam charge ($\boldsymbol{Q_{im}}$) according to:

$$Im_{gross}\,[t_{im}]_{(x,y)} = Im_{net} \times Q_{im} + DC \times t_{im} + RN \qquad [5\text{-}1]$$

Where Im_{net} is the net neutron induced signal in CCD signal units (u) per unit beam charge (Q_{im}), DC the dark current noise rate in u/s, t_{im} the exposure time and RN the readout noise in CCD signal units (u).

2. Readout noise image (RN)

Readout noise is a combination of system noise components inherent to the process of converting CCD charge carriers into a voltage signal for quantification, subsequent processing and analog-to-digital (A/D) conversion. This noise, added uniformly to every image pixel and described by the number of electrons per pixel, is independent of exposure time (t_{im})**.** The RN is acquired by triggering on the CCD camera for the shortest possible integration time (close to 0 sec), while the shutter is closed.

3. Background image ($Bmoff_{gross}[t_{off}]$)

Each pixel (x,y) in the background image, also referred to as **beam-off image**, contains a signal which is comprised of RN and dark current:

$$Bmoff_{gross}[t_{off}]_{(x,y)} = RN + DC \times t_{off} \qquad [5\text{-}2]$$

Dark current contribution to the background increases linearly with acquisition time ($\mathbf{t_{off}}$). The image acquisition is performed with opened CCD shutter, with the neutron beam off and the image intensifier operated at the same regime as when the neutron beam is on. For good quality images the $Bmoff_{gross}[t_{off}]$ should be collected for a long time (t_{off}), in order to obtain good statistics. Minimal integration time should be at least equal to the integration time of the radiography object image.

4. Flat image ($Flt_{gross}[t_{flt}]$)

The flat (full-transmission) image is acquired while neutron beam is on, but without any object placed between the neutron source and the detector:

$$Flt_{gross}[t_{flt}]_{(x,y)} = Flt_{net} \times Q_{flt} + DC \times t_{flt} + RN \qquad [5\text{-}3]$$

All settings are kept similar to those used during the radiography of the object of interest. The Flt_{net} image is used for pixel-by-pixel normalization of Im_{net}. This operation (also

known as *flat fielding*) removes image non-uniformities that originate from differing pixel response to light and also corrects for neutron beam intensity variations across the detector area. This image should also be taken with good statistics, in order not to impair image quality.

Each pixel (***x,y***) in the final net image is calculated as:

$$Im_{net,(x,y)} = \frac{[Im_{gross} - RN]/t_{im} - [Bmoff_{gross} - RN]/t_{off}}{Q_{im}/t_{im}} \qquad [5\text{-}4]$$

An identical expression is obtained for the flat image:

$$Flt_{net,(x,y)} = \frac{[Flt_{gross} - RN]/t_{flt} - [Bmoff_{gross} - RN]/t_{off}}{Q_{flt}/t_{flt}} \qquad [5\text{-}5]$$

Each pixel ***Pix(x,y)*** in the net normalized transmission image is represented as:

$$Pix(x,y) = Im_{net,(x,y)}/Flat_{net,(x,y)} \qquad [5\text{-}6]$$

5.2 Factors affecting image quality

Radiographic image quality can be quantitatively assessed by deriving the experimental values for spatial resolution and contrast. These figures-of-merit are governed by:

- Irradiation system geometry and various backgrounds. These include geometrical un-sharpness, scattered neutrons and gamma background.
- Intrinsic detector response

In order to characterize TRION's response, it is important to clearly define the system-response related factors and minimize their effect on image quality.

5.2.1 Irradiation system geometry

The divergent incident neutron beam and finite source dimensions introduce geometric un-sharpness in the neutron radiography images. The ***L/D*** ratio, also known as the *collimation ratio* [21,71-72], defines the geometric un-sharpness originating from the finite dimension of the radiation source (***D***) and the distance between source and object (***L***).

Image un-sharpness U_g due to the finite source dimension is expressed by:

$$U_g = \frac{L'}{(L/D)} \qquad [5\text{-}7]$$

Where L' is the distance between the object and neutron detector.

In our case the deuteron beam diameter on the target is about 5 mm, the distance between target and detector is 12 m, while the distance between object and detector varied between 0.15 m (PTB 2004) and 0.5 m (PTB 2005). Thus the geometrical unsharpness is only 62.5 μm for the former and 208 μm for the latter, smaller than the fiber dimension in both runs (250 and 500 μm, respectively).

The impact of beam divergence can be minimized by keeping the target-detector distance large compared to detector dimensions. In our case the maximum divergence angle is 0.48°.

5.2.2 Neutron and gamma ray background

On their way to the detector, neutrons may be scattered by the collimation system and the interrogated object. Some of these neutrons reach the detector and affect image formation by producing unwanted scintillation events in the scintillator. A large number of such events will tend to degrade image resolution and contrast by adding to the image noise.

Neutrons scattered inelastically by the collimation system and thermalized neutrons undergoing capture reactions may produce gamma rays. These gamma rays may reach the scintillator and cause spurious scintillation events that degrade image contrast and resolution. The GEANT simulation of the PTB beam transport system, described in chapter 4, shows that the contribution of the scattered neutrons and gamma-rays to the direct neutron beam is below **0.5%**.

It is thus safe to conclude that the irradiation-system related factors do not significantly influence the determination of intrinsic detector response.

5.2.3 Intrinsic detector response

Each of TRION's components may influence the spatial resolution of the detector. The TRION detector is based on de-magnification of the 200×200 mm^2 object-image by a factor of 20 on a CCD chip, divided into approximately 1536×1024 pixels. For such a configuration, the basic resolution unit in the object plane cannot be better than approximately 200×200 μm^2.

In the following sections, we will attempt to separate the different contributions to image quality, imported by the following components & characteristics:

1. The scintillating screen
2. The inherent resolution of the optical system
3. Overall resolution obtained with neutrons
4. Image intensifier and CCD noises

5.2.4 The Contrast Transfer Function (***CTF***)

An objective method for the assessment of image quality [73-75] is provided by the calculation of Modulation Transfer Function (MTF) or the Contrast* Transfer Function (***CTF***) [76]. These are used to quantify the imaging system's ability to transfer contrast from an object to an image at various resolution levels or spatial frequencies.

The ***CTF*** represents the response of an imaging system to a constant square-wave input in terms of spatial frequency, whereas the MTF represents the response to a sine wave input. As the spatial frequency increases, the observable image contrast decreases. It is this loss of contrast at higher spatial frequencies that characterizes the performance of the imaging device.

In order to calculate the ***CTF***, an image profile (see fig. 5.1) depicting TRION's response to a constant square-wave input mask (such as the one seen in fig. 5.2) is analyzed.

The ***CTF*** at a certain spatial frequency ω is calculated using the maximum (I_{max}) and minimum (I_{min}) transmission values, also seen in fig. 5.1:

$$Modulation(\omega) = \frac{I_{\max}(\omega) - I_{\min}(\omega)}{I_{\max}(\omega) + I_{\min}(\omega)} \qquad [5\text{-}8]$$

$$CTF(\omega) = \frac{Modulation(\omega)}{Modulation(\omega_o)} \qquad [5\text{-}9]$$

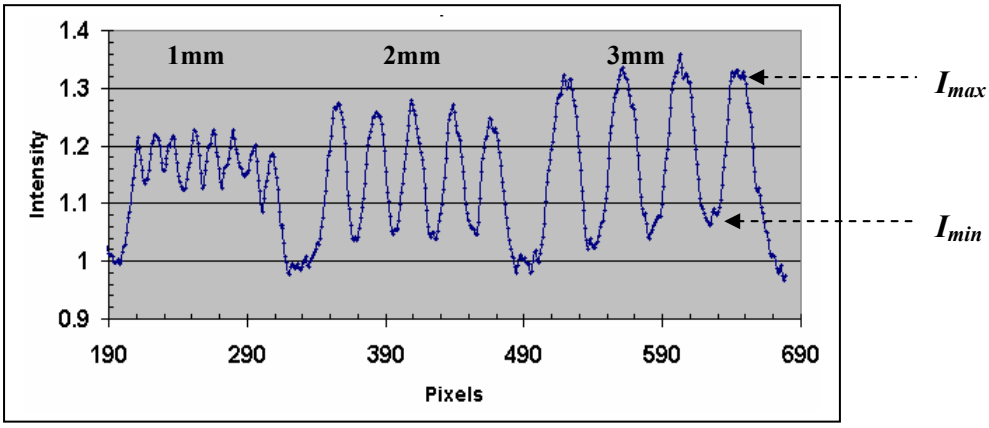

Fig. 5.1: Image profile containing three different spatial frequencies

* Image contrast = (max. brightness – min. brightness) / (max. brightness + min. brightness) [60]

The convention employed is that each modulation (***modulation(ω)***) is normalized by the modulation of the lowest spatial frequency (***modulation(ω_o)***) which represents the best achievable contrast.

A common reference unit for spatial frequency is the number of line pairs per millimeter (lp/mm). For example, a continuous series of black and white line pairs (seen in fig. 5.2) measuring 0.5 mm per pair would repeat twice every millimeter, thus having a corresponding spatial frequency of 2 lp/mm.

An ideal imaging system would have an MTF or ***CTF*** of unity at all spatial frequencies (a system with a delta function response). However, due to imperfect response of the system as a result of aberrations, assembly imperfections, alignment errors and other factors, a real image will be somewhat degraded in comparison to the original object.

In order to characterize the resolving power of the TRION imaging system, a bar-patterned mask containing a series of slits with increasing spatial frequency and decreasing slit width, as illustrated in fig. 5.2 was imaged and analyzed.

For determination of the resolution of the optical system the pattern on the left was transmission-illuminated using a flat lamp (described in section 5.3.2). For neutron transmission resolution studies an identical pattern mask made from steel (shown on the right side) was used.

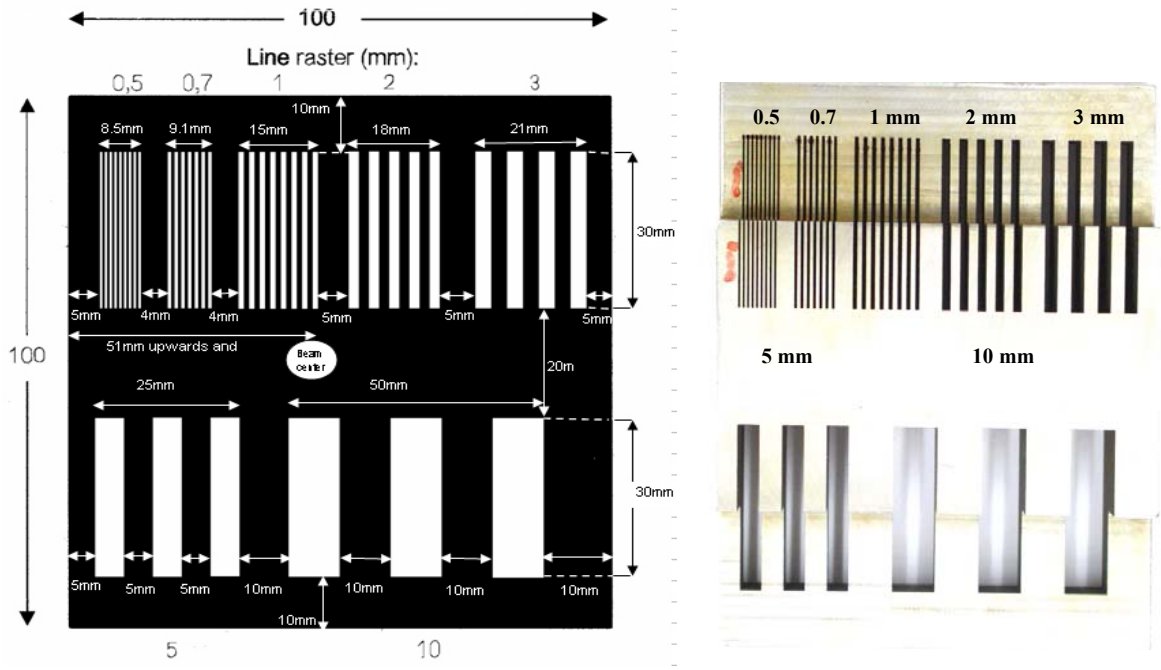

Fig. 5.2: Optical pattern mask (left) and steel mask (right) for CTF calculation

5.3 Influence of TRION's components on ***CTF***

5.3.1 Scintillating screen

As mentioned previously, plain slab scintillators are affected by the *depth-of-field* effect (see section 3.3.1): the thinner the slab the better the spatial resolution, at the expense of detection efficiency. For this reason, fiber scintillator screens are favorable, providing independence of spatial resolution from scintillator thickness (which translates to detection efficiency).

The spatial resolution of a scintillating fiber screen is affected by the fiber cross-sectional dimensions, range of the knock-on proton generated by the incident neutron, multiple scattering of neutrons within the screen and light cross-talk between fibers.

Fiber diameter determines the inherent spatial resolution achievable employing the fiber screen. However, the recoil proton may cover a distance of several hundred microns (a ~3.75 MeV proton will travel 203 μm [77]) before coming to rest within the scintillator. Thus, the best achievable spatial resolution is of the order of the maximal proton range within the scintillator for a given neutron energy.

In order to determine the contribution of the fiber screen to the degradation of the spatial resolution, light generation due to neutron interactions within the polystyrene fiber screen was simulated by the GEANT 3.21 code [56]. The calculation simulated the experiment performed in November 2004 (first round) at PTB, in which the steel mask shown in fig. 5.2 was radiographed. The screen pixel size was 250×250 μm^2 and the distance between the Be target and the screen was 12 m. The deuteron beam diameter on the target was 5 mm and the steel mask was positioned at a distance of 15 cm from the screen.

The GEANT simulation calculated the total amount of energy deposited in a fiber by protons created directly in the fiber and by protons entering the fiber from the surrounding area. In addition, the simulation calculated the number of light photons generated in a fiber by each proton, taking into account the non-linear behaviour of the light-energy relation for protons.

Figs. 5.3 a - c show profiles calculated with GEANT, taken over the high frequency portion of the steel mask for three neutron energies: 2, 7.5 and 14 MeV.

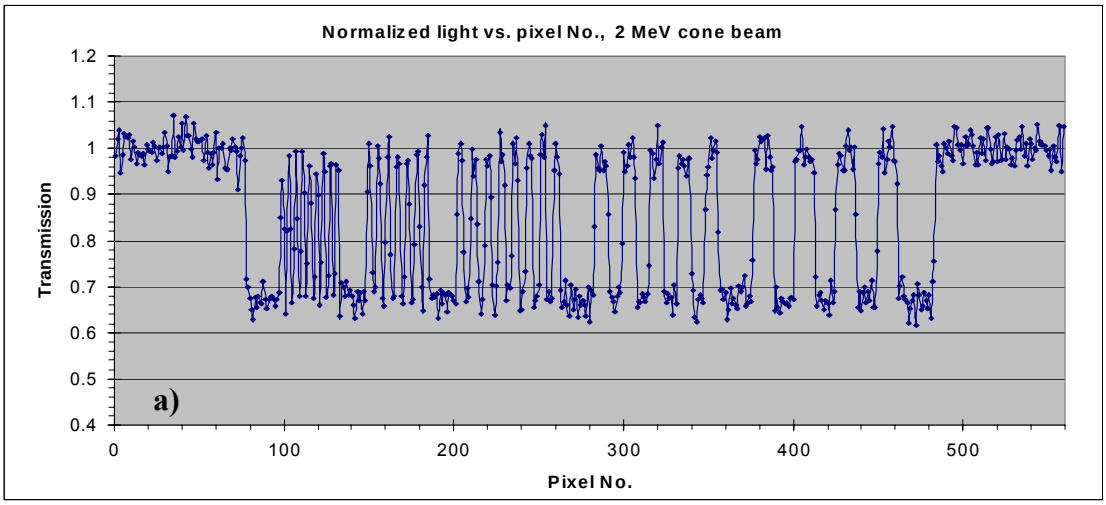

Fig. 5.3a: Profile taken over the high frequency portion of the steel mask, simulated by GEANT 3.21 for 2 MeV neutrons

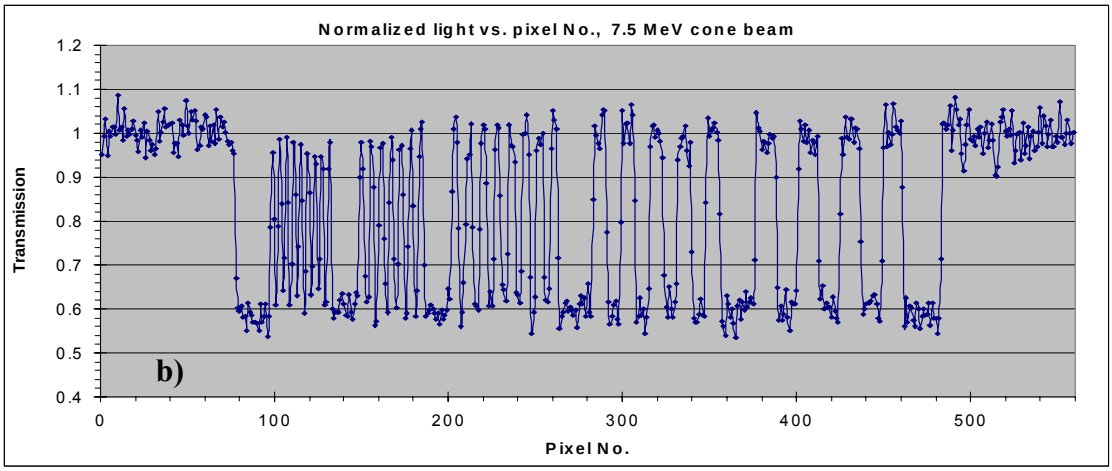

Fig. 5.3b: Profile taken over the high frequency portion of the steel mask, simulated by GEANT 3.21 for 7.5 MeV neutrons

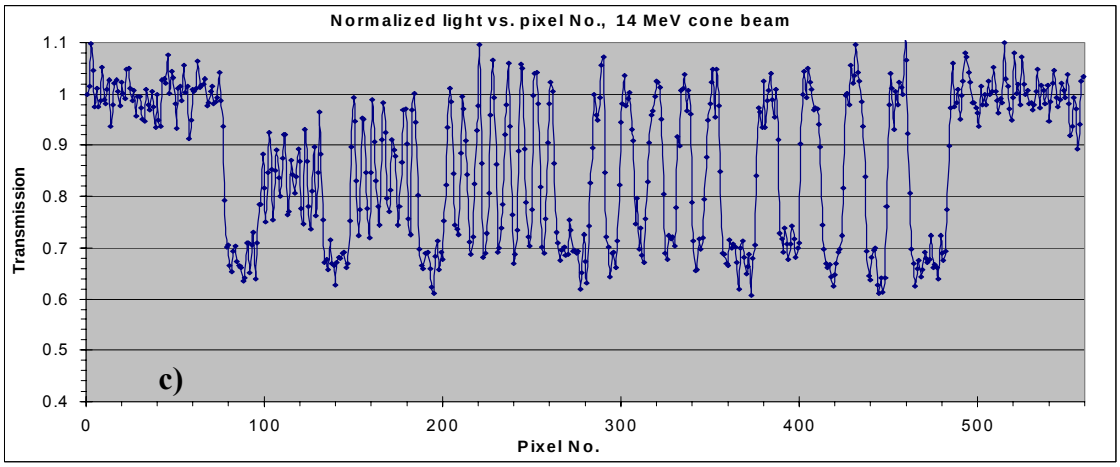

Fig. 5.3c: Profile taken over the high frequency portion of the steel mask, simulated by GEANT 3.21 for 14 MeV neutrons

The ***CTF*** was calculated for each of the above simulated profiles, as shown in fig. 5.4.

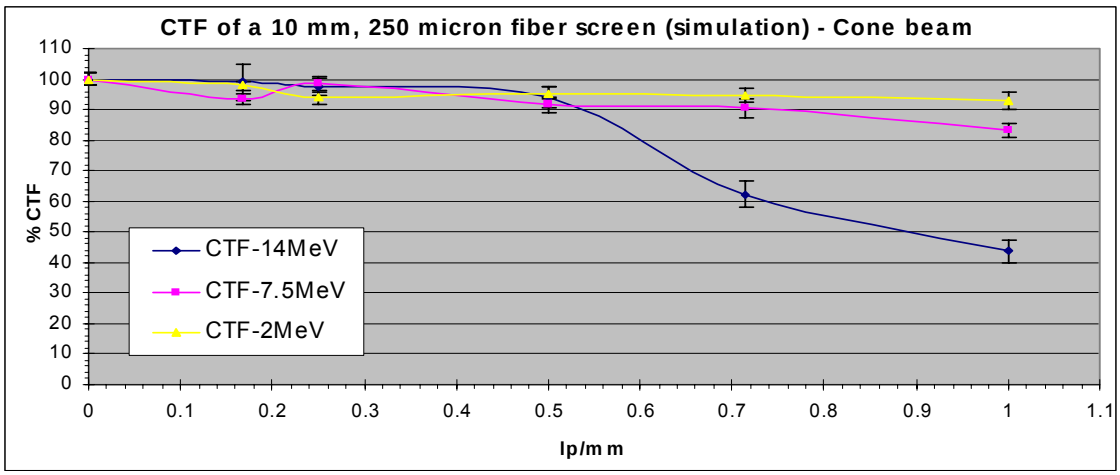

Fig. 5.4: Intrinsic *CTF* of 10 mm thick scintillating fiber screen (250 µm fiber dimension), simulated for 2, 7.5 and 14 MeV neutrons

As can be observed the ***CTF*** decreases with spatial frequency. There is a slight difference between the ***CTFs*** related to the 2 and 7.5 MeV neutrons. The range of 1 MeV and 3.75 MeV protons (average proton energy) is 22 and 203 µm, respectively [77]. Thus it is smaller than the size of a 250 µm fiber. For 14 MeV neutrons, the range of a 7 MeV proton is 608 µm [77], causing a significant deterioration of ***CTF*** at frequencies higher than 0.5 lp/mm.

In order to obtain the ***CTF*** for 500 µm fibers, an average of two 250 µm fibers was taken. The result of this averaging, seen in fig. 5.5, clearly displays that the resolution of the 500 µm fiber screen is inferior to that of its 250 µm counterpart.

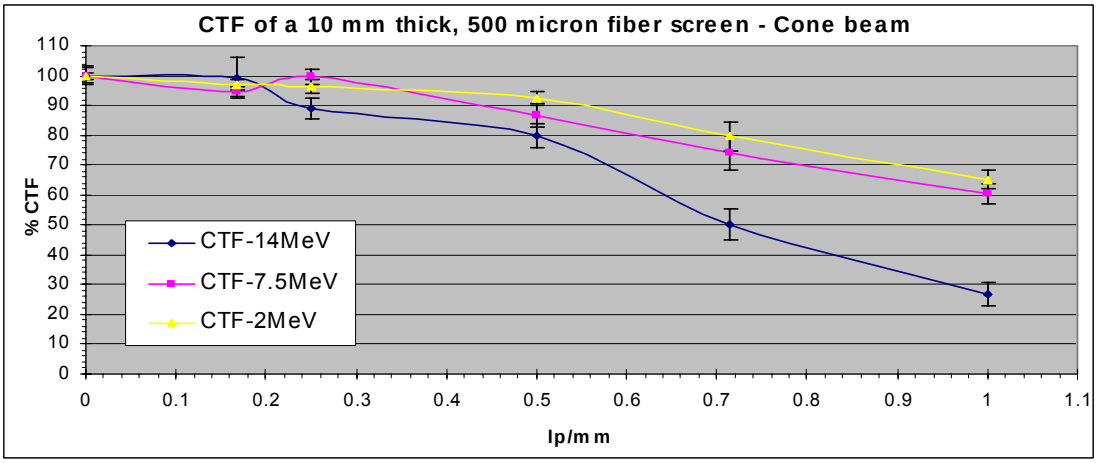

Fig. 5.5: Intrinsic *CTF* of 10 mm thick scintillating fiber screen (500 µm fiber dimension), simulated for 2, 7.5 and 14 MeV neutrons

5.3.2 Optical resolution

In order to examine the purely optical performance of the TRION imaging system, excluding neutron influence, a spatial resolution mask (see fig. 5.2) was imaged in two fashions:

- With image intensifier
- Without image intensifier

An electroluminescent (EL) sheet manufactured by Pacel electronics, coupled to a polyethylene light diffuser (seen in fig. 5.6), was used as a uniform light source to transmission-illuminate the pattern shown in fig. 5.2.

Images were taken the with image intensifier present and with the image intensifier removed.

The latter required repositioning the CCD camera and the 200 mm lens, such that the 200 mm lens is focused on the image created by the 120 mm F#0.95 lens.

Fig. 5.6: EL sheet used as uniform light source

Figs. 5.7a and 5.7b show images taken without and with image intensifier, respectively. In all experiments the amount of photons emitted from the lamp was such that the signal was much higher than the I-I and CCD noises.

The CTF was calculated for each image using data extracted from image profiles.

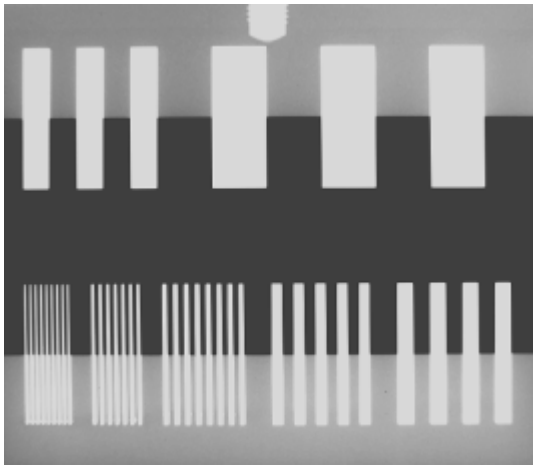

Fig. 5.7a: Optical image taken without the I-I

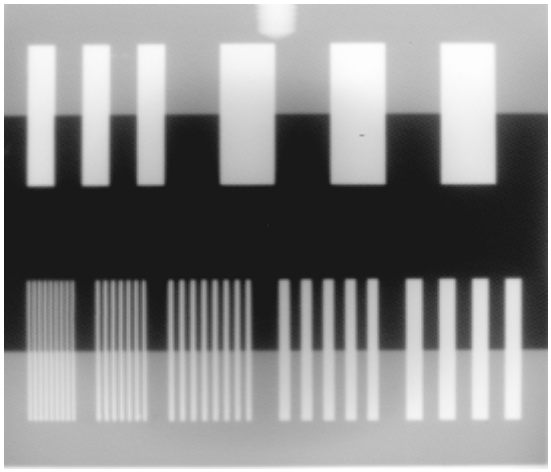

Fig. 5.7b: Optical image taken with the I-I

Visual inspection of the images leads to the conclusion that the image taken **without** the image intensifier is superior. This conclusion is supported by the ***CTF*** plots, shown in fig. 5.8.

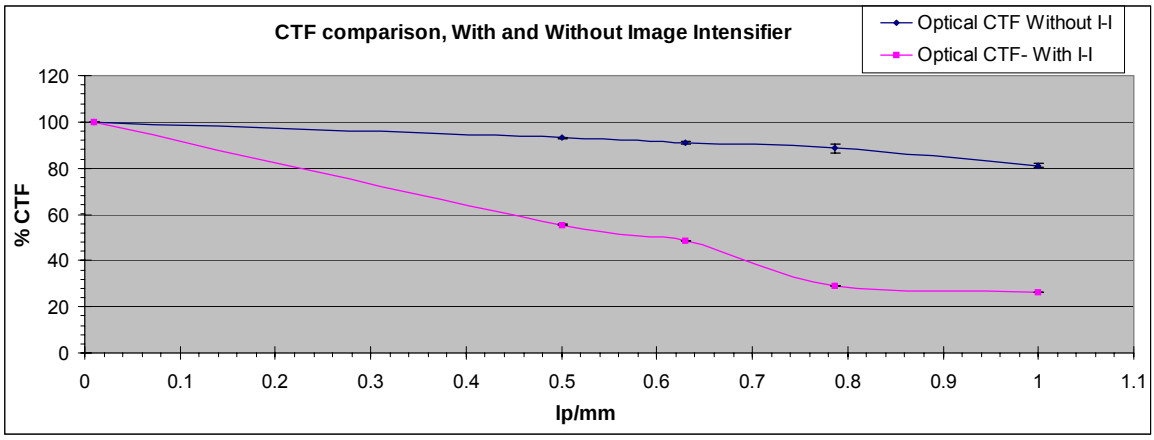

Fig. 5.8: *CTF* comparison between images taken with image intensifier and without

Clearly, the image intensifier significantly degrades the spatial resolution. The manufacturer of the I-I claims a limiting resolution of 20 lp/mm, which translates to 4 lp/mm at the object plane (with a de-magnification factor of 5). At present this high degradation of ***CTF*** by the I-I is not yet explained.

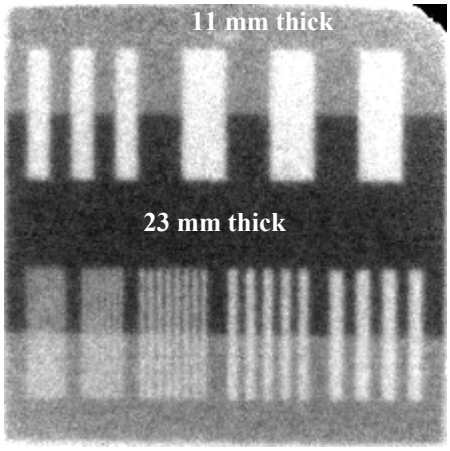

Fig. 5.9: Radiography image of the steel mask taken with a 10 mm thick fiber scintillator screen

5.3.3 Overall response to neutrons

The calculation of the overall spatial resolution of the TRION imaging system was accomplished by the analysis of radiography images, shown in fig. 5.9, of a 10×10 cm^2 steel patterned test mask, portrayed in fig. 5.2.

This radiograph was obtained by integrating the entire spectrum (see fig. 4.7) of neutrons (referred to as **All-E** images).

Fig. 5.10 shows a comparison between the ***CTF*** of the radiography image (taken with a 10 mm thick fiber scintillator screen) and the ***CTF*** of the optical images. It can be clearly seen that neutron-related effects further degrade image quality.

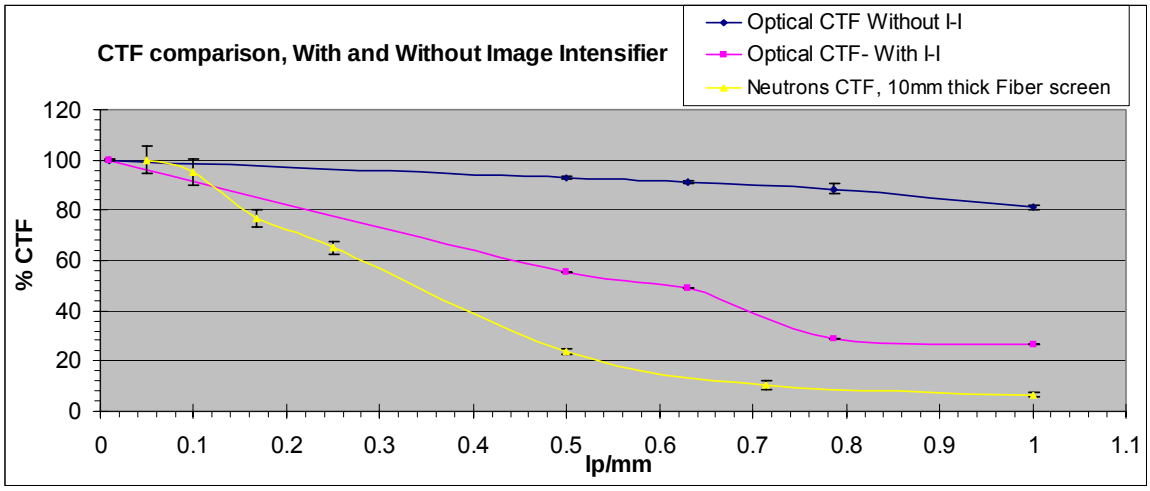

Fig. 5.10: Comparison of *CTF* received at different acquisition modes: pure optical without image intensifier, pure optical with image intensifier and neutron radiography image with 10 mm thick fiber screen

5.3.4 Image intensifier and CCD-related noise

The Signal to Noise Ratio (SNR) of TRION is predominantly affected by: *neutron shot noise*, *photon shot noise*, *image intensifier thermal noise* and *CCD noise*. The first two are related to the neutron signal and light conversion efficiency. The other two sources of noise introduce background that must be minimized or subtracted. Here we shall concern ourselves with the latter two sources.

5.3.4.1 Image-intensifier related noise sources

The main source of background in our I-I is Equivalent Background Illumination (EBI) [75,78]. EBI is an inherent background noise of an image intensifier which sets the lower detection limit. It is normally specified as the input illuminance required to produce a luminous emittance from the phosphor screen equal to that obtained when the input illuminance is zero. The noise is almost entirely due to thermal electrons emitted by the photocathode and is therefore highly dependent on photocathode material and temperature. EBI can be reduced by keeping the image-intensifier in darkness (for over an hour) and cooling the photocathode. At extremely low illumination levels the EBI adds some haze to the image.

5.3.4.2 CCD-related noise sources

The noise components accompanying the signal generated in a CCD system (see appendix 4) are *photon shot noise*, *photo-response non-uniformity, quantization noise, dark noise and readout noise.* The *photon shot* and *dark noises* contributions can be reduced by averaging over longer collection times. The *dark noise* can be lowered significantly by

cooling the CCD chip. In general, high-performance CCD chips exhibit a one-half reduction in dark current for every 5 to 9 ^{o}C of cooling below room temperature [79], a characteristic referred to as the "*doubling temperature*". Typically, this rate of improvement continues down to a temperature of approximately 5 to 10 ^{o}C below zero, beyond which the reduction in dark current becomes less pronounced.

Figs. 5.11 & 5.12 describe dark current as function of temperature measured with the Chroma C3 CCD. It was measured by taking an average and standard deviation (STD) of net (without readout noise) dark image values in a selected image area. As can be seen, the dark current and its STD decrease as CCD sensor temperature decreases.

Under low illumination level conditions (assuming dark noise is essentially eliminated by CCD cooling), I-I noise and readout variance are greater than that of the photon shot noise [79], hence the image signal is limited by noise from other sources. The camera exposure time can be increased to collect more photons and increase SNR, until a point is reached at which photon noise variance exceeds that of both readout noise and dark noise. Above this exposure time, the image is said to be *quantum-noise limited.*

Image exposure time is limited by CCD dynamic range which depends on full well capacity (FWC) and noise floor. Thus, in order to improve image statistics, several radiography images taken consecutively are averaged after background subtraction and normalization by flat image.

In order to ascertain whether TRION images are quantum noise limited, a set of repeated 24 images acquired at the PTB 2004 experiment was selected to be analyzed. The image was taken with a large time window of 80 ns at a time-delay corresponding to an average neutron energy of ~3.5 MeV, resulting in an energy window ranging between 2.9 - 4.2 MeV. Exposure time per image was 200 s and accelerator current was 3 μA. The 10 mm thick fiber screen was employed.

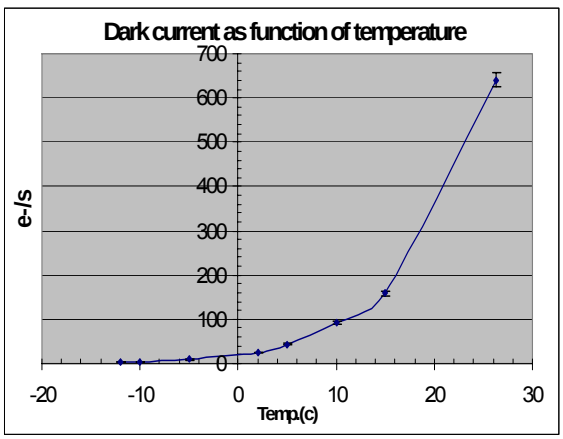

Fig. 5.11: Dark current as function of CCD temperature

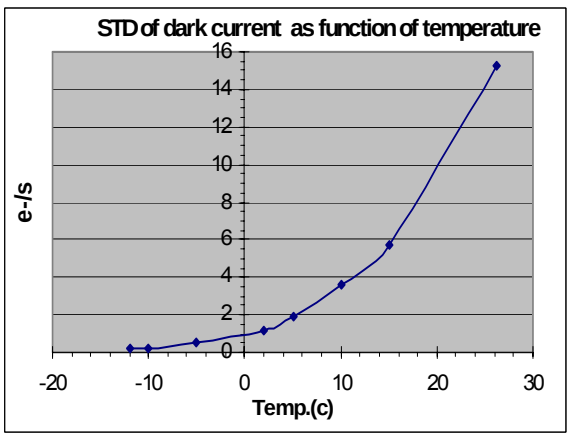

Fig. 5.12: Standard deviation of the dark current as function of CCD temperature

Averaging of images was performed in increments, such that n=1 indicates no averaging, n=2 indicates averaging of 2 images, and so on. The analysis was performed on net normalized images as defined in section 5.1.

For the purpose of image analysis, a window containing 8833 pixels was specified and mean and standard deviation (STD) of the grey levels were calculated. Analysis results (summarized in table 5-2) show that image statistics improves as the number of averaged images increases. This is to be expected since image averaging effectively prolongs image exposure duration, resulting in improved event statistics and correspondingly reduced variability.

Table 5-2: Analysis of averaged images. n indicates the number of images averaged

n images	1/n	Mean	STD	Variance	STD/mean
1	1.000	1.037	0.151	0.0228	0.1456
3	0.333	1.035	0.095	0.0090	0.0918
5	0.200	1.033	0.08	0.0064	0.0774
7	0.143	1.034	0.071	0.0050	0.0687
9	0.111	1.035	0.067	0.0045	0.0647
12	0.083	1.029	0.062	0.0038	0.0603
14	0.071	1.02	0.061	0.0037	0.0598
26	0.038	1.024	0.055	0.0030	0.0537

Based on the results summarized in table 5-2, this work assumes that the TRION system obeys the following behaviour of variance/pixel:

$$Var_m = Var_{\text{int}} + \frac{1}{n} Var_n \qquad [5\text{-}10]$$

Where n is the number of averaged images, Var_m is the measured variance, Var_n is the variance due to quantum noise in a single image and Var_{int} is an intrinsic variance due to the CCD and image-intensifier related sources of noise discussed in previous sections.

The variance results (seen in table 5-2) were plotted as function of the inverse number of images (as shown in fig 5.13) and linearly fitted according to eq. 5-9:

$$Var_m = 0.00217 + \frac{1}{n} 0.02062 \qquad [5\text{-}11]$$

Eq. 5-10 leads to:

$\sigma_n = 0.1436$ $\sigma_{int} = 0.0466$

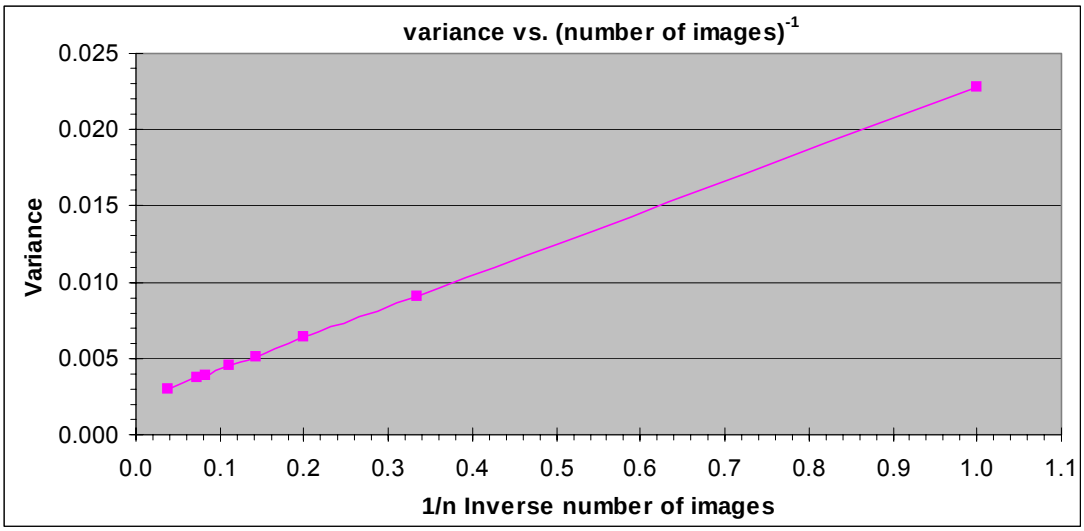

Fig 5.13: Variance vs. inverse number of images

Thus, the relative quantum noise is 14.3% while the relative intrinsic noise contributes only 4.6% to the total relative error; hence, the image is predominantly quantum-noise-limited.

It is interesting to compare this result with the expected neutron statistics. Taking the neutron flux at the detector to be **1.8×10^4 n/s·cm^2 per µA** (see chapter 4) and accelerator current of 3 µA. The fraction of neutrons arriving at the detector during the gating-window of 80 ns was **0.29**, detection efficiency of the 10 mm fiber screen (250 micron pixel diameter) at 3.5 MeV is **9%,** leading to the expected neutron count rate per pixel of **0.69 counts/s**. In 200 s we shall thus accumulate **138 counts/pixel**.

A relative standard deviation of this counting statistics is **8.5%**, i.e., significantly better than the **14.3%** estimated experimentally. This increase in error is due to the limited number of photoelectrons per incident neutron produced in the photocathode of the I-I. This effect increases the relative statistical error in neutron counting by a factor of $(1+1/n_e)^{1/2}$ [80], where n_e is the average number of photoelectrons/neutron. Using the above expression and the 1.68 factor increase in quantum noise we estimate n_e to be **0.54** photoelectrons/neutron. This figure corresponds very well to an estimate of **0.53** photoelectrons/neutron calculated by using the following ab-initio values: **2930** light photons/n created in a scintillator for a 3.6 MeV neutron, lens collection efficiency

g=**0.016**, fraction of light emitted from fiber (max **8.8**% using a reflecting mirror) and I-I quantum efficiency of **13%**.

5.4 Dependence of image quality on screen type and thickness

In these experiments we compared the uniformity, light output and ***CTF*** for fiber screen and plain scintillating slabs of different thickness. All radiographs were taken using the entire spectrum of neutrons (**All-E** images). The radiography of the steel patterned mask was repeated several times, employing the following different screens:

a. 3 mm thick slab

b. 10 mm thick slab

c. 20 mm thick slab

d. 10 mm thick fiber screen (0.25×0.25 mm^2 fiber)

e. 30 mm thick fiber screen (0.5×0.5 mm^2 fiber)

Fig. 5.14 shows a flat image (full transmission image) of the 30 mm thick fiber screen (left) and 3 mm thick slab screen (right). The fiber screen, made of polystyrene, is assembled of 10×10 mm^2 square bundles of 0.5×0.5 mm^2 scintillating fibers. Each fiber is coated with white paint (Extra Mural Absorber-EMA) to prevent light cross-talk. The plain slab screens were manufactured by EL-JEN from polyvinyltoluene (EJ-200).

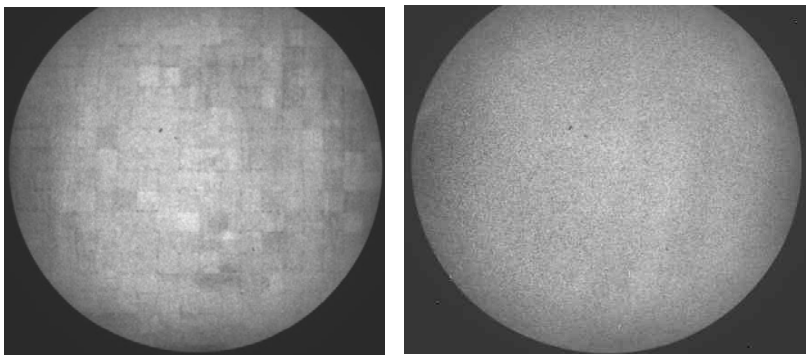

Fig. 5.14: Flat image of 30 mm thick fiber screen (left) and 3 mm thick plain slab (right)

The flat image obtained with the fiber screen is considerably non-uniform, indicating the necessity of image normalization via a high-quality flat image.

The net light output for the 30 mm polystyrene fiber screen was **55.5±4.8 u/s** (u represents CCD signal units). The 3 mm polyvinyltoluene (EJ-200) yielded **13.9±1.6 u/s**. Thus the ratio of light output for these two screens is ~ **4**.

Taking into account the lower H/C stoichiometric ratio (0.99 in polystyrene vs. 1.11 in polyvinyltoluene) we calculate the detection efficiency of the 30 mm fiber screen to be **8**

times higher than that of the 3 mm slab. However, Polystyrene has **20%** lower light output than polyvinyltoluene. So the expected calculated ratio is **6.4** or **60%** higher. The EMA may reduce the light output by as much as by a factor of 2, but we did employ a reflecting mirror coupled to the fiber screen, which should compensate for it. In summary, the topic of light output dependence on screen type requires further systematic investigation.

Fig. 5.15 show radiography images of the steel patterned mask using 10 mm fiber scintillator screen (left) and 10 mm plain slab scintillator (right).

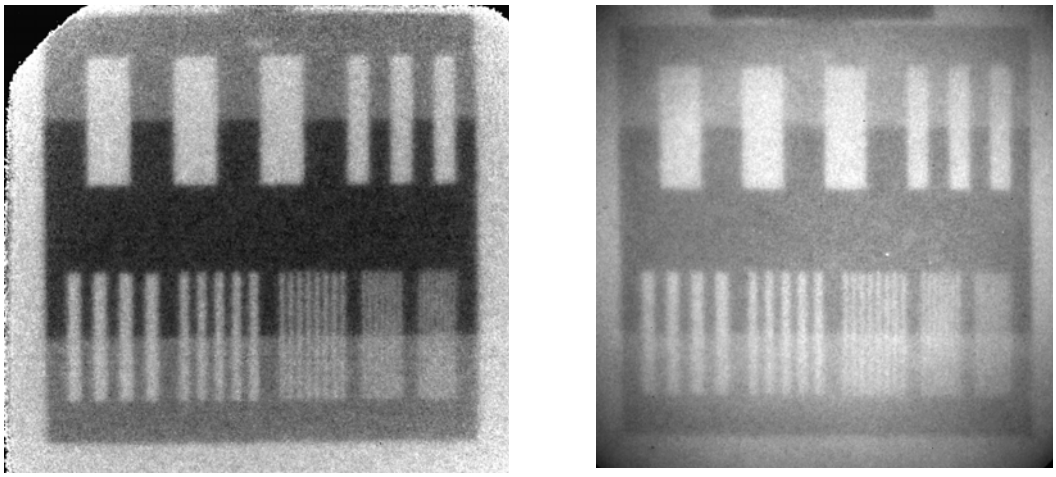

Fig. 5.15: Radiography images of the steel patterned mask using a 10 mm fiber scintillator screen (left) and a 10 mm plain slab scintillator (right)

Fig. 5.16 shows the result of the CTF comparison. As can be seen, the CTF related to the fiber scintillator is superior to that obtained with the plain scintillator slab. This result is to be expected due to the fact that the fiber screen maintains spatial resolution independent of the depth-of-field effect.

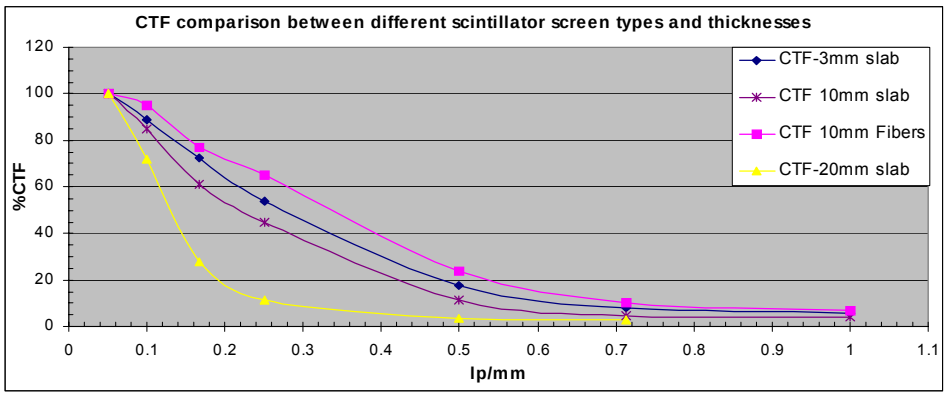

Fig. 5.16: CTF comparison between different scintillator screen types and thickness

5.5 CTF as function of neutron energy

For the purpose of determining TRION's spatial resolution dependence on neutron energy, several radiography images of the steel patterned mask were acquired at different neutron

energies, as can be seen in fig. 5.17. Minimal acquisition time per pulse was determined by the pulser narrowest gate width which was ~12 ns. Images were taken for the following neutron energies: 2, 7.5 and 14 MeV, employing the 30 mm thick fiber screen.

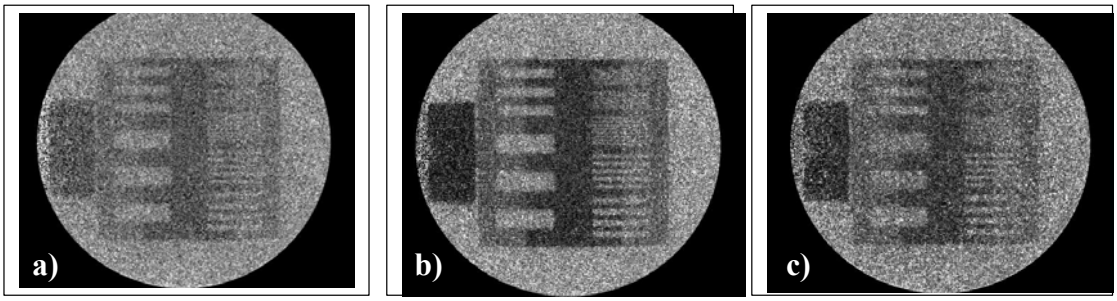

Fig. 5.17: Radiography images taken with different neutron energies: a) 2 MeV b) 7.5 MeV and c) 14 MeV

As can be seen in fig. 5.15, image quality is relatively poor due to low neutron statistics. This is reflected also in the ***CTF*** comparison, seen in fig. 5.18, in the sense that it follows only partially the conclusions based on the GEANT simulations mentioned earlier (see fig. 5.4).

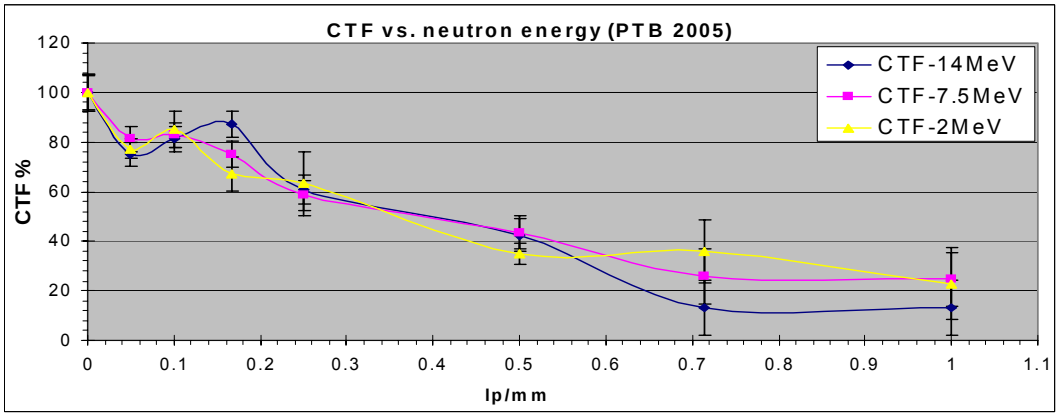

Fig. 5.18: *CTF* calculated for different neutron energies: 2, 7.5 and 14 MeV

One of the useful mathematical properties of the ***CTF*** is that the overall ***CTF*** of imaging-system components is equal to the product of the individual components ***CTF's*** [81]. Thus, the above experimental ***CTF*** results from the multiplication of the pure optical ***CTF*** by the pure neutron-induced ***CTF*** (as obtained by the GEANT simulations, section 5.3.1).

Fig. 5.19 shows a comparison between the calculated ***CTF's***, resulting from the multiplication of the pure optical ***CTF*** by the pure neutron-induced ***CTF***, and the experimental ***CTF***. As can be seen, there is a reasonable consistency, considering the appreciable noisiness of the experimental images and the uncertainty in the neutron energy due to the ~12 ns I-I gate width.

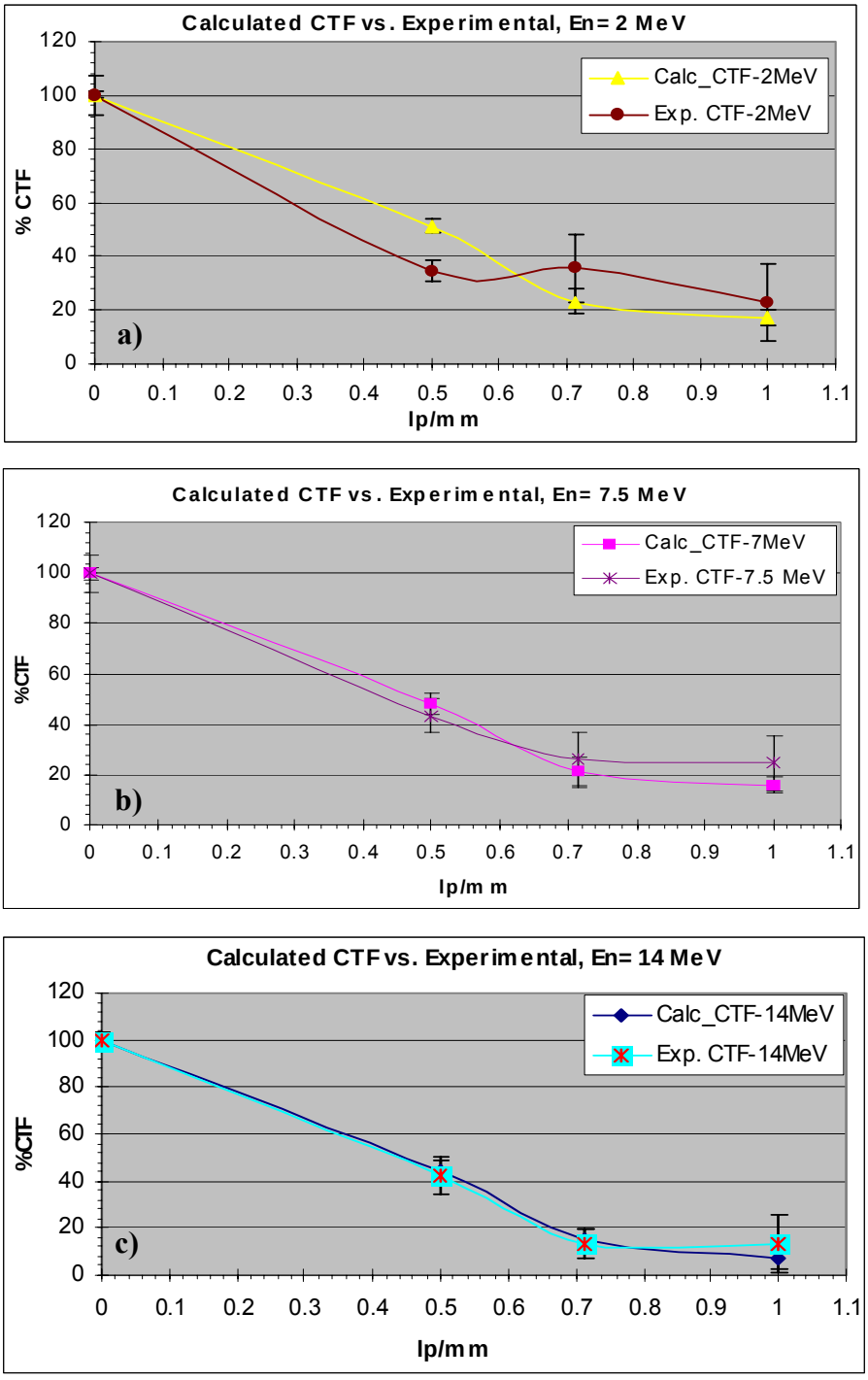

Fig. 5.19: Comparison between calculated CTF and experimental CTF for neutrons of energies: a) 2 MeV; b) 7.5 MeV and c) 14 MeV (right)

5.6 Fast-neutron radiography images

For the purpose of demonstrating the quality of spatial resolution provided by the TRION imaging system, different phantoms were imaged (see figs. 5.18 – 5.20). For each pulse, the I-I gating window was set to be opened for a time duration enough to capture neutrons of all energies.

Fig. 5.20a & b show the fast-neutron radiograph of a phantom and the actual phantom, respectively. The phantom consists of: a plastic toy gun, trumpet mouthpiece, two vials containing water and acetone mixtures (numerical markings on the vials indicate water volume percentage), two regular AA batteries wrapped with an electrical wire.

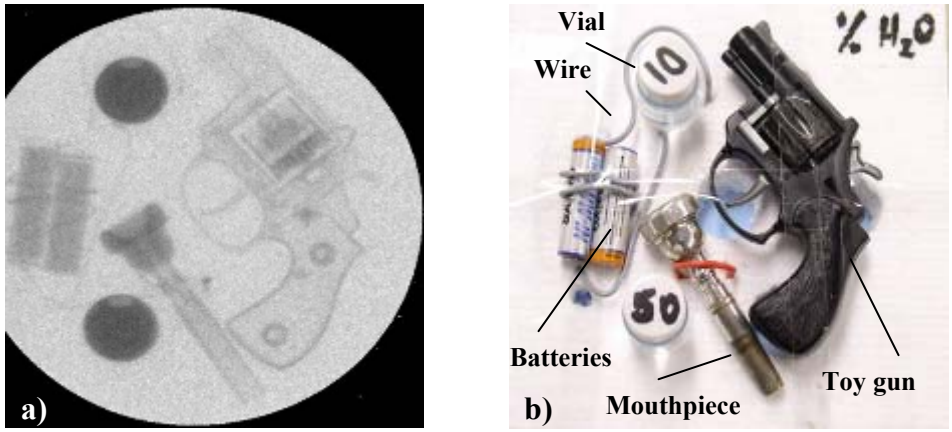

Fig. 5.20: a) Radiography image of a phantom containing plastic toy gun, trombone mouthpiece, vials containing water and acetone mixture, batteries wrapped with an electrical wire b) An image of the actual phantom

The dimensions of the vials were: 25 mm in diameter, 55 mm in length.

The phantom seen in figs. 5.21a & b contains: three melamine samples (of different thicknesses), steel pliers, a shaped tungsten object, a vial containing acetone and a vial containing water.

The dimensions of the vials were: 25 mm in diameter and 106 mm in length. The melamine samples shown in the radiography image are numbered from 1 to 3 in order to distinguish among them according to their dimensions. The samples are in compacted powder form (density ~1 gr/cm^3) encased within 3 mm thick perspex sheets.

The thicknesses of melamine samples 1, 2 and to 3 are: 50 mm, 50 mm and 5 mm, respectively.

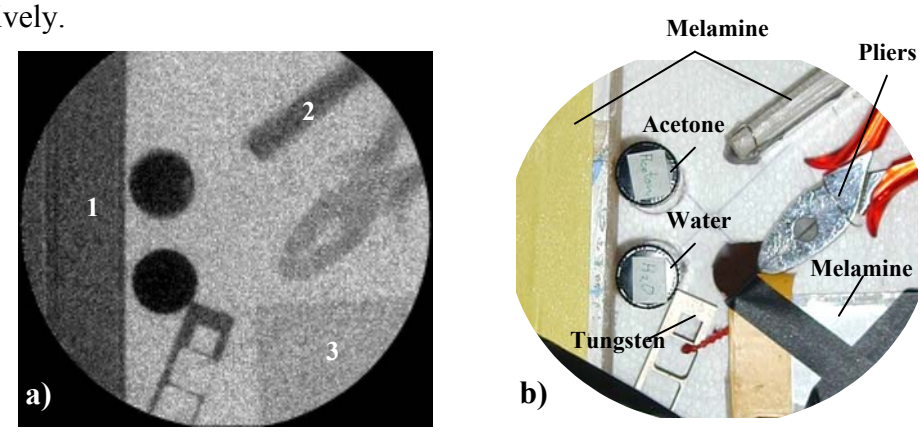

Fig. 5.21: a) Radiography image of a phantom containing three melamine samples, steel pliers, tungsten hollow block, vial containing acetone and an additional vial containing water; b) An image of the actual phantom

Figs. 5.22a – c display a phantom consisting of a plastic toy gun, hollow tungsten block, two vials containing water and acetone mixture (partial water volume in the vials is 50% and 10%), melamine powder and a BNC connector. To study image quality when the phantom is obscured by a dense material, this phantom was placed behind 1" thick lead bricks and radiographed.

Vial dimensions were: 25 mm in diameter, 55 mm in length and melamine sample thickness was 50 mm.

As can be seen, the spatial resolution appears to be unaffected by the presence of the lead bricks.

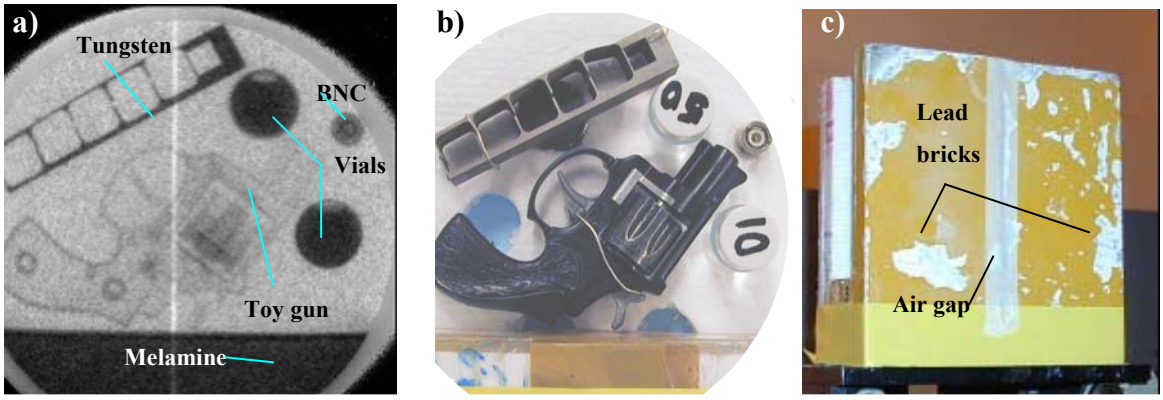

Fig. 5.22: a) Radiography image of a phantom containing plastic toy gun, tungsten hollow block, vials containing water and acetone mixture and a melamine sample; b) An image of the actual phantom; c) An image of the lead bricks that obscure the phantom. The gap between them is seen in (a) as a white vertical line

These images show that TRION can provide high resolution fast-neutron radiography images that can provide the means for visual identification of suspicious items within inspected luggage.

5.7 Temporal resolution

As described in chapter 2, the PFNTS method employs a ns-pulsed broad energy spectrum neutron beam. As opposed to the conventional event-counting variant of the TOF method, in which the arrival time of an individual neutron is recorded, TRION captures a cumulative image at a fixed time t_{TOF} relative to each beam burst, which corresponds to a selected energy window around E_n determined by Δt (see fig. 5.23).

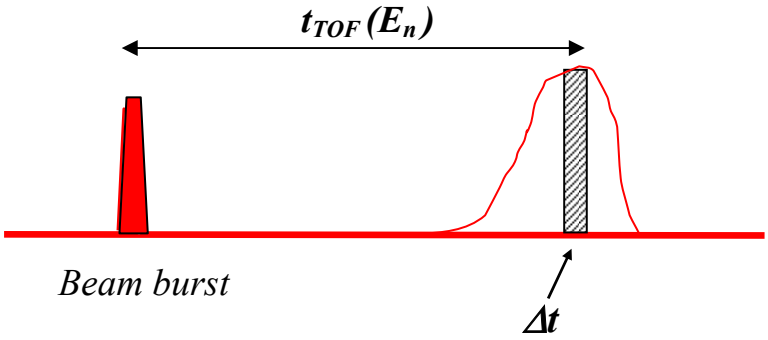

Fig. 5.23: TRION image acquisition regime per beam burst: the image is acquired after time t_{TOF} corresponding to neutron energy E_n

Thus, in order to register scintillation light related exclusively to neutrons of a specific energy, TRION's image intensifier has to be time-gated. The temporal resolution directly affects the contrast ratio between "on-resonance" neutrons (neutrons of energy corresponding to a peak in the total cross-section for the element of interest) and "off-resonance" ones.

The temporal resolution of TRION is governed by the following factors:

- The minimal achievable I-I gate width
- Scintillation decay time.

Long decay times will generate a memory-effect from light created by faster neutrons, which reach the detector earlier than the neutrons of interest. There are additional factors which affect the temporal resolution, such as accelerator beam burst duration and target-to-detector distance, but they are not detector related and must be addressed on a separate footing.

5.7.1 Scintillator decay time

In contrast to the event counting variant of the TOF method (see above), the decay time constant of scintillation light does affect the timing resolution and resonant contrast in the integrative detector TOF measurements. As mentioned in chapter 3, when performing TOF measurements the decay time-constant of the scintillation light (wavelength of ~420 nm) must be as short as possible, in order to provide accurate timing.

For the purpose of determining the effect of the scintillator light decay duration on image contrast, an event counting TOF spectrum obtained with the NE102 plastic scintillator/photo-multiplier (see section 4.1) was convolved with its light decay curve (fig. 3.7 in chapter 3).

Fig. 5.24 shows event-counting TOF spectrum following transmission through 10 cm thick graphite as obtained by the NE102 scintillator/photo-multiplier (blue line), and the same spectrum after convolution (pink line) with the NE102 light decay curve of fig. 3.7. As can be observed, the finite decay of the light reduces the contrast, especially for narrow resonances. The contrast was defined as the difference between the peak and the dip, normalized to the sum of these values. The reduction in contrast due to the finite decay time of the scintillator was **11%**, **57%** and **41%** for the time (energy) intervals indicated by **a**, **b** and **c** respectively.

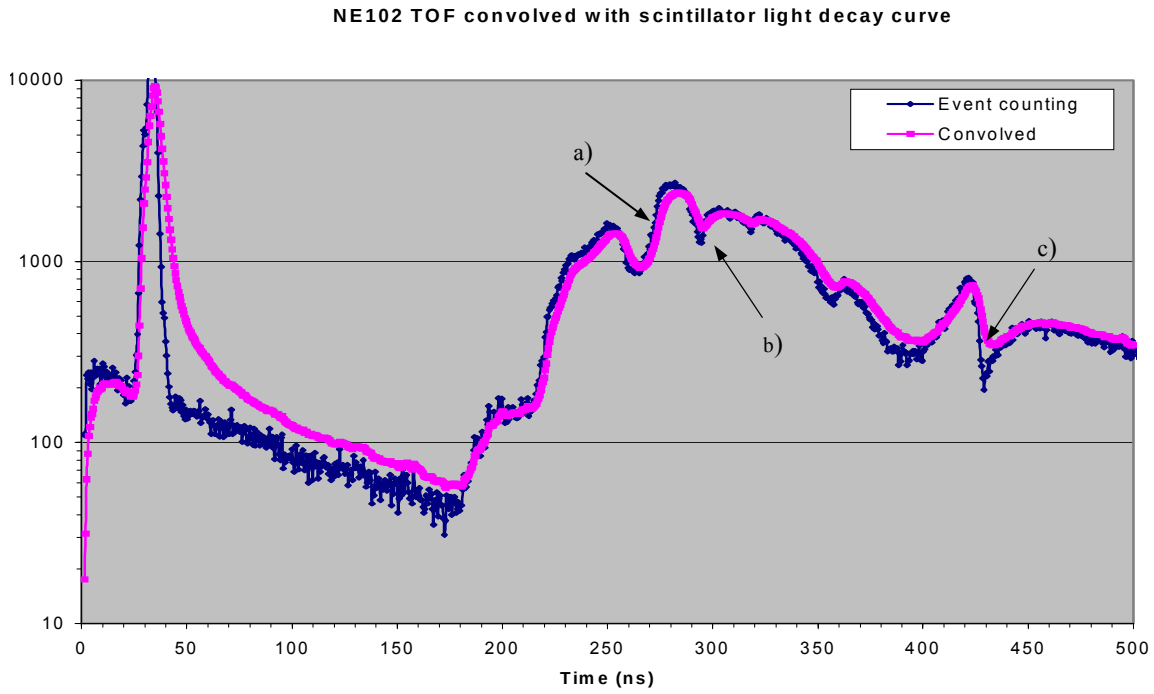

Fig. 5.24: Event counting TOF (blue) and its convolution with the decay curve of NE102 (pink) for a 10 cm thick graphite absorber

5.7.2 Minimal achieved I-I gate width

As stated previously, temporal resolution is principally determined by the image intensifier gate-width. The shorter the gating time, the better the TOF resolution. As the diameter of the I-I photocathode increases, its capacitance and inductance increase and it becomes increasingly more difficult to gate it for short time-intervals. During the 2004 experiments we used a 20 ns gating window for the TOF measurements. This is a long gating time which caused appreciable loss of contrast in elemental imaging. Nevertheless we were able to obtain good separation between different elements, as will be demonstrated in the following sections.During the 2005 experiments the PTB group succeeded in shortening the I-I gating window to about 10-12 ns. The effective gating window of the I-I was

determined by finding the minimal High Voltage (HV) gate width that allowed the I-I to be fully opened.

As the direct HV gate signal at the I-I photocathode was not accessible for oscilloscope measurement, the gamma peak, which has a FWHM of 1.7 ns (as measured with a Cerenkov detector) was scanned in 1 ns steps with gates of different widths provided by the gate and delay generator (G&DG). This scan generates a curve that represents a convolution of the gamma-ray burst width with the actual opening time of the I-I.

Fig. 5.25 shows the scans for different G&DG gate widths. By measuring the FWHM of the curves and taking into account the beam burst FWHM, it is possible to determine the effective opening time of the I-I.

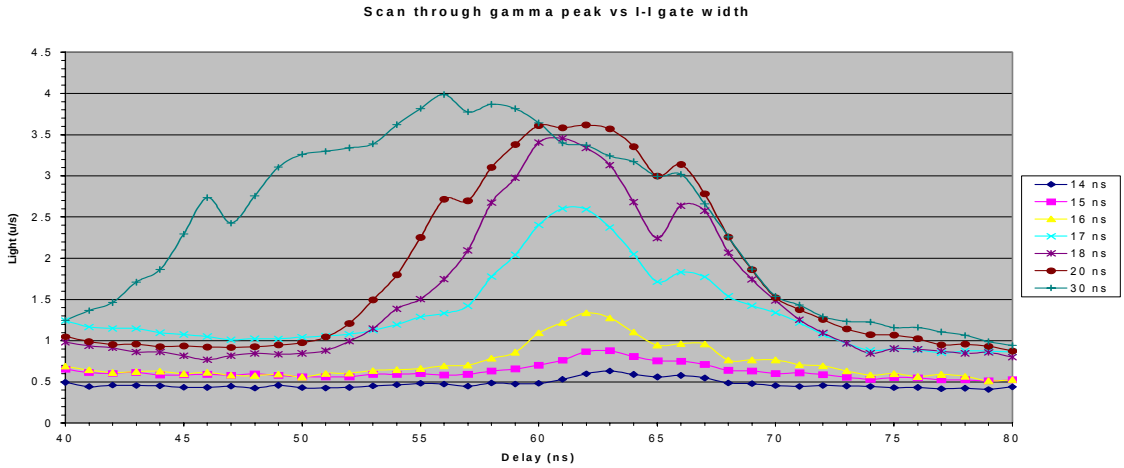

Fig. 5.25: Gamma peak scanned in 1 ns steps in order to determine the minimal HV gate width

As can be observed from the scan, the I-I does not open completely at short gate widths. The I-I starts to open efficiently at a G&DG gate width of 18 ns. The minimal G&DG gate width in the 2005 run was set at **19 ns**.

Table 5-3 shows the effective opening time of the I-I vs. G&DG gate width.

Table 5-3: Effective duration of the I-I opening time vs. GDG gate width

GDG gate width (ns)	Scan FWHM (ns)	I-I FWHM (ns)
14	6	5.7
15	7	6.8
16	8	7.8
17	10	9.9
18	11	10.9
20	13	13
30	22	22

For the 19 ns GDG gate width the effective opening time of the I-I is ~ **12 ns**.

5.7.3 The effect of I-I gate width

In order to evaluate the influence of the I-I gate width on contrast, the event-counting spectrum described in previous sections was averaged using a 10 ns and 20 ns time window (corresponding to the gate-width at which the TRION system was operated in the two runs). The result of this averaging, seen in fig. 5.26, shows that for the 10 ns window the contrast reduction was **3%**, **58%** and **25%** for the above intervals. The 20 ns gate caused a much larger contrast reduction: **31%**, **89%** and **52%** respectively.

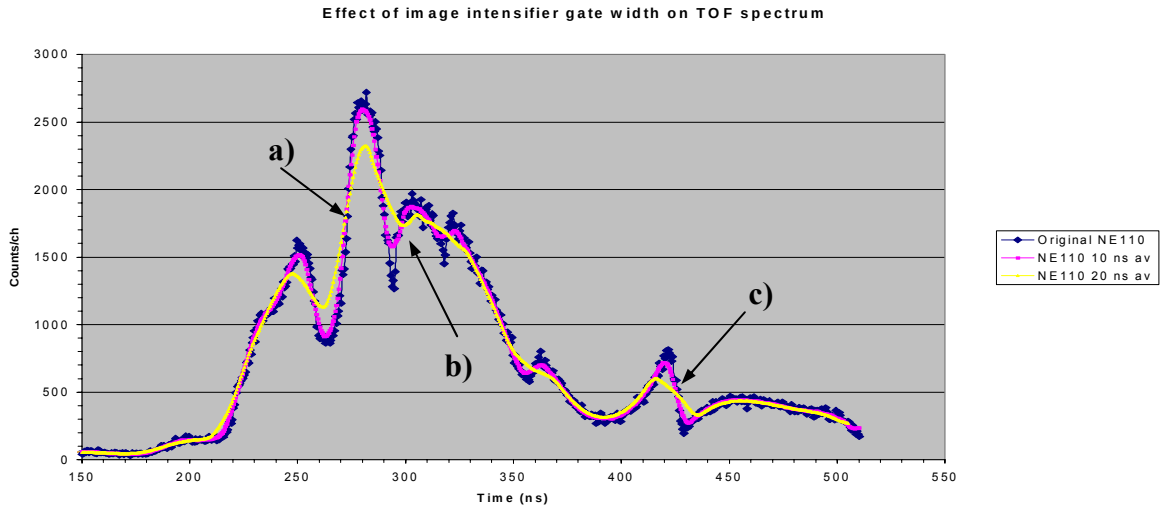

Fig. 5.26: Effect of I-I gate width on TOF spectrum. Measured event-counting spectrum averaged using a 10 ns and 20 ns time window

It would appear that scintillation decay time has a greater influence on contrast than the 10 ns gate width, but it is the 20 ns gate width that causes the most serious loss in contrast.

5.7.4 Experimental evaluation of TRION TOF spectrometry

The signal obtained with TRION, for a given energy (or TOF) can be expressed as:

$$S(TOF)_{TRION} = N(TOF) \times \varepsilon(TOF) \times L(TOF) \qquad [5\text{-}12]$$

Where ***N(TOF)*** is the number of neutrons reaching the detector after a certain ***TOF***, ***ε(TOF)*** is the detection efficiency for these neutrons and ***L(TOF)*** is the average number of light per neutron generated by neutrons with energy corresponding to this ***TOF***.

Fig. 5.27 shows experimental TOF spectra obtained with the TRION system in two scenarios: full transmission and transmission through a 10 cm thick graphite block. In this experiment our setup was positioned at 25° to the deuteron beam.

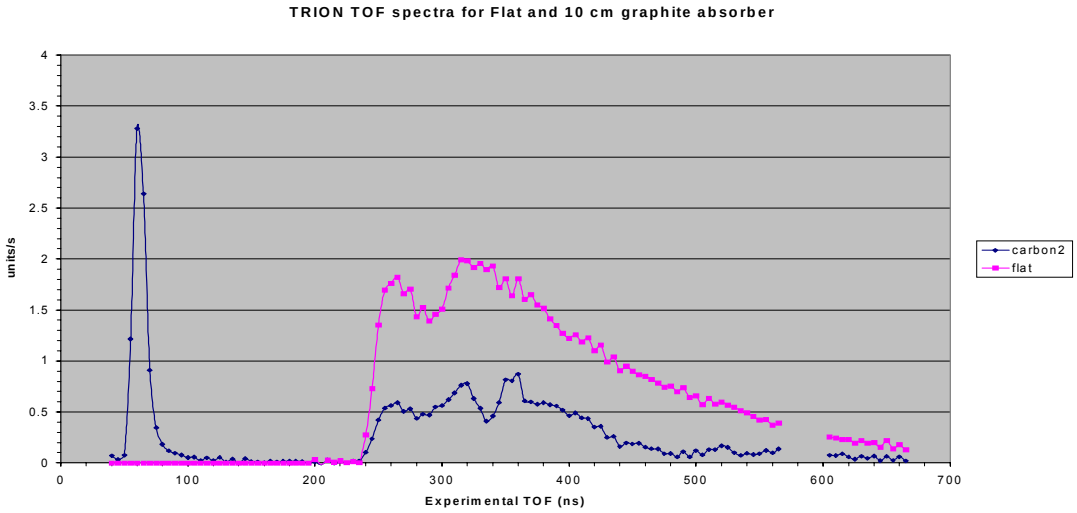

Fig. 5.27: TOF spectra of full transmission and transmission through 10 cm thick graphite block, obtained with TRION

Since **L(TOF)** is a non-linear function of neutron energy, the shape of the measured **TOF** spectrum of TRION is expected to differ from that of an event-counting TOF system, where the signal is the number of counts, as follows:

$$S(TOF) = N(TOF) \times \varepsilon(TOF) \qquad [5\text{-}13]$$

For purposes of comparison between the two methods, the measured TOF spectra must be normalized by a full-transmission (flat) TOF spectrum. The result is pure attenuation, free of the influence of detector light output, efficiency and incident flux.

Fig. 5.28 compares the transmission spectrum through 10 cm thick graphite obtained by TRION and by a NE102 plastic scintillator/PMT operating in event-counting mode. The spectra were corrected for the different distances of the two detectors. The G&DG gate width was 19 ns (I-I opening time window of 12 ns).

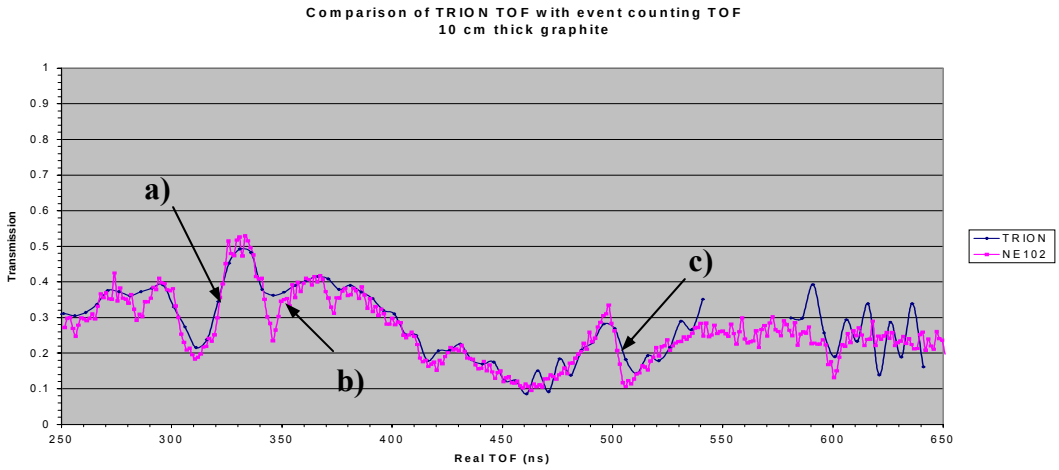

Fig. 5.28: Comparison between TRION transmission spectrum to event counting spectrum

The measured reduction in contrast of the 3 regions previously described was **18%**, **75%** and **38%,** respectively**.** The combined effect of scintillation decay time and 12 ns gate width is larger than that of each of them separately for energy regions **a** & **b**. There was no effect of gate width on the contrast for energy region **c**. This is probably due to large statistical errors originating from the relatively low neutron flux in this energy region.

5.7.5 Elemental imaging

The purpose of the TRION system is to perform element sensitive imaging. The preliminary demonstration of carbon imaging is described in this section.

A phantom consisting of a steel wrench, melamine block and 6 graphite rods of various dimensions (see fig. 5.29) was radiographed at different neutron energies (PTB 2004). The energies of interest were selected to coincide with a peak (7.7 MeV, see fig. 5.31a) or a dip (6.8 MeV, see fig. 5.31b) in the total interaction cross-section of carbon.

Fig. 5.30 displays the TOF spectrum of d-Be fast neutrons transmitted through a block of graphite, obtained with the TRION imaging system.
When dividing figs. 5.31a by 5.31b, all non-carbon features disappear (melamine contains approx. 20% carbon), as can be seen in fig. 5.31c. Thus, the ratio of the two images provides an enhanced projected image of the carbon areal-density map.
As can be observed by the circled area in fig. 5.29, only part of the phantom was in the TRION field-of-view. This was due to the small size (12×12 cm^2) of the fiber screen available at the time of the experiment (PTB, 2004).
The dimensions of the radiographed graphite rods, in accordance to their index number, seen in fig. 5.29, are:
Rod 1: 60 mm thick, 30 mm in diameter
Rod 2: 40 mm thick, 30 mm in diameter
Rod 3: 40 mm thick, 20 mm in diameter
Rod 4: 20 mm thick, 30 mm in diameter

Fig. 5.29: Phantom used for TOF elemental imaging. The phantom consists of carbon rods, a steel wrench and a melamine block

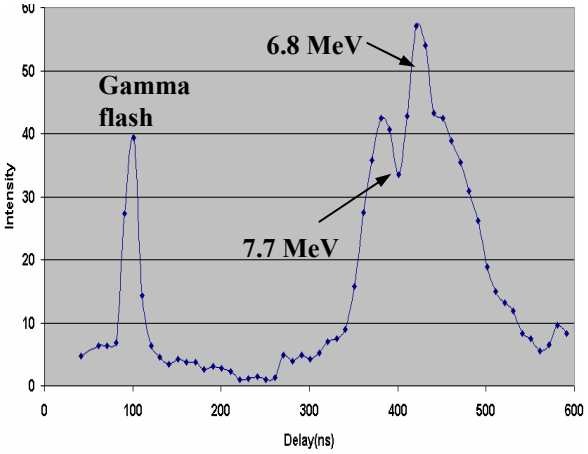

Fig. 5.30: TOF spectra of d-Be fast neutrons transmitted through a block of graphite, obtained with the TRION imaging system

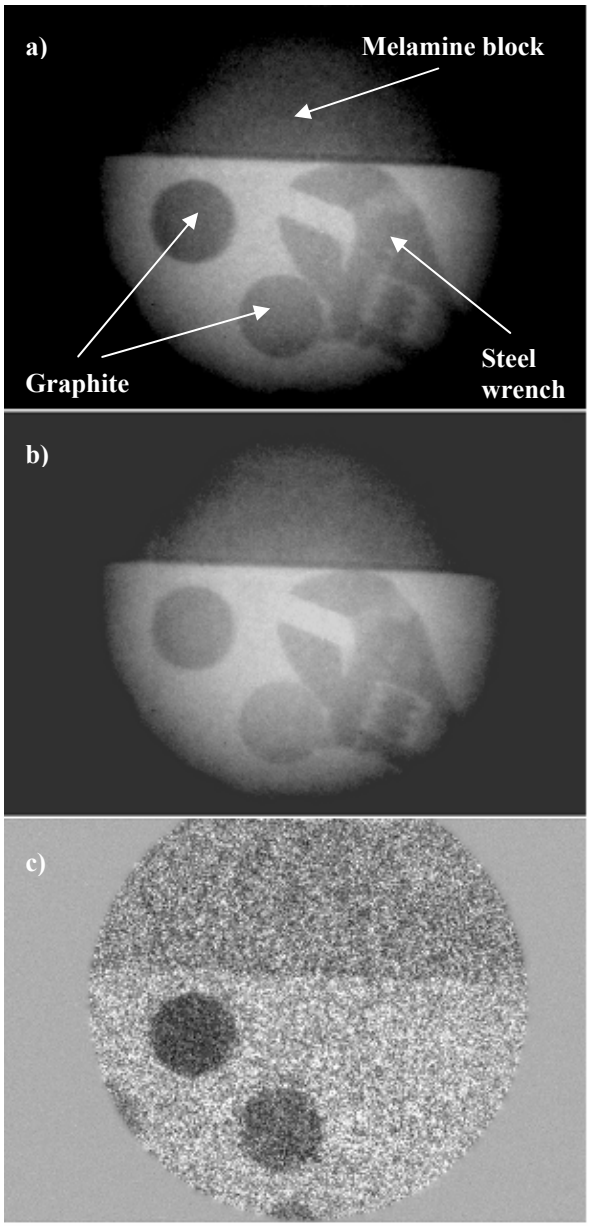

Fig. 5.31: TOF images of the phantom taken with: a) neutrons of about 7.7 MeV; b) neutrons of ~6.8 MeV and c) the pixel-by-pixel ratio of image (a) to (b). As is clearly seen, the steel wrench disappears, leaving only the graphite and melamine blocks present in the picture (Melamine contains approx. 20% carbon)

Chapter 6

6.1 Summary and conclusions

PFNTS holds promise for detecting a broad range of conventional and improvised explosives, by determining the identity and density distribution of light elements such as C, N, and O within the inspected object.

The TRION system, described in this work, can be considered as a next-generation PFNTS detector. It is an efficient, large-area fast-neutron detector that incorporates the combined capabilities of sub-mm spatial imaging and TOF spectrometry and is also designed for loss-free operation in mixed, high-intensity neutron-gamma fields. Thus, it fulfills all the requirements of a PFNTS detector, as outlined in chapter 3.

The main part of this work dealt with the determination of the factors that govern the spatial and timing resolution of TRION. More specifically:
The spatial resolution is determined by the screen type, response of the optical system and the various sources of noise that the system is susceptible to.
Among others, we have demonstrated that fiber scintillator screens are favorable over plain slab scintillators, due to the fact that they provide independence of spatial resolution from scintillator thickness (which translates to detection efficiency). Indeed, the spatial resolution of a slab screen deteriorates rapidly with screen thickness due to the *depth-of-field* effect. For example, a 10 mm thick fiber screen provided better quality images than a 3 mm thick slab screen. Fiber dimensions are dictated by the range of the knock-on protons and should be of the order of the maximal proton range within the scintillator, i.e., several hundred microns (on average) in the relevant neutron energy range.
It was found that the light output per neutron of the fiber screen was lower than that of the slab. The reason for that could be the fact that there is a significant dead layer between the fibers, due to the EMA paint and misalignment of the fibers. This aspect of screen properties will require further investigation.

6.1.1 Spatial resolution

The principal source that degrades the spatial resolution in TRION is the image intensifier. Although its manufacturer claims a limiting resolution of 20 lp/mm, which translates to 4

lp/mm at the object plane (de-magnification of factor 5), the results obtained here indicated considerably poorer performance of the I-I. At present, this high degradation of CTF by the I-I is not yet explained.

Spatial resolution is also affected by various noise sources. The predominant sources affecting SNR are: *neutron shot noise*, *photon shot noise*, *image intensifier thermal noise* and *CCD noise*. Of these, the *photon shot noise* and *I-I thermal noise* are the dominant factors. The *photon shot noise* results from the low light output of the scintillator screen and the relatively low light collection by the large aperture lens (F#=0.95). This is especially true at low neutron energies, where the average number of photoelectrons produced in the I-I per neutron is less than 1. This can be improved by using a larger diameter I-I, thereby reducing the demagnification factor.

The second most important source of background is the *I-I noise*, which is almost all due to thermal electrons emitted by the photocathode and is therefore highly dependent on photocathode temperature. This noise can be reduced by cooling the photocathode.

6.1.2 Temporal resolution

Working in conjunction with a pulsed beam, TRION captures an image at a well-defined TOF that corresponds to a pre-selectable energy. Thus, in order to register scintillation light related only to neutrons of a specific energy, TRION's image intensifier must be gated. The temporal resolution (which translates to energetic resolution) directly affects the contrast ratio between "on-resonance" neutrons and "off-resonance" ones.

The temporal resolution of TRION is limited by the following factors:

- The minimal achievable I-I gate width
- Scintillation decay time

Currently, the minimal effective opening time of the I-I is ~**12 ns**. In the future, it may prove possible to shorten it by a more efficient coupling of the HV pulser to the photocathode of the I-I, or by reducing the RC time constant of the photocathode.

It has also been shown that the scintillation decay time of our plastic scintillator screen has a greater influence on the elemental-imaging contrast than the 12 ns gate width.

The light decay time constant is a property of the scintillator and its effect on timing resolution may be reduced by choosing a scintillating material with less intensity in the

long component. Certain liquid scintillators with severely quenched long components could prove attractive candidates for a scintillating screen.
An alternate way to recover the loss of contrast is to de-convolve the influence of these two factors from the measured TOF spectra. The feasibility of doing this hinges on the fact that TRION's response to a sharp (delta) time signal can be determined from a scan of the gamma-ray peak. Thus, the shape of the latter can be used as a kernel for the deconvolution function.

Regardless of the above limitations, excellent quality fast-neutron radiography images of various phantoms were obtained. The unprecedented quality of these fast neutron images is approaching that obtainable with conventional X-ray inspection systems and can certainly be used by the operator for visual inspection of the content of the analyzed object, in addition to the automatic elemental detection of PFNTS. A demonstration of high quality imaging of objects shielded by 1" thick lead was also performed.

In summary, compared to the event counting detectors used by the University of Oregon and Tensor Technology, TRION imaging system, representing the next generation of PFNTS detectors, provides superior (sub mm) position resolution combined with loss-free operation at very high neutron-flux intensities. At present TRION TOF resolution is inferior to that of the event counting method, but partial recovery of the resolution by deconvolution appears feasible.

Recommendations for future work
1. As the total cross-section for C, N and O exhibits several peaks and dips at different fast-neutron energies, it is necessary to select from them a minimal number that will ensure a reliable elemental reconstruction.
2. Currently, TOF imaging by TRION is performed in a serial fashion, i.e., each image acquisition relates to a single peak or dip, or in other words, the I-I is triggered to capture just one energy interval per accelerator pulse. Thus, in order to progress towards a real-time operational system, it is necessary to acquire several energy regions for each accelerator pulse.
This can be achieved by employing several ns-triggered CCD cameras, such that each camera acquires a different energy region per accelerator pulse. The number of cameras

will be determined according to the minimal number of cross-section peaks and dips, as specified in the previous paragraph.

3. As was outlined in section 5.3.4, intrinsic noise levels are non-negligible and must be reduced. A major contributor to this noise is the I-I. Hence, by finding a way of cooling the I-I effectively, this noise can be reduced.

4. The improvement of the temporal resolution should be investigated, either by deconvolution techniques or by replacing the scintillator screen with a faster scintillating material and operating with short gate widths.

5. Further simulations are required to determine the influence of thermal neutron-capture gamma-rays background on the contrast. A simulation of TRION's behavior in a more realistic PFNTS inspection geometry should be also carried out.

Bibliography

1. Breznier J. S., Berger H., Gibbs K.M., Mengers P., Stebbings C.T., Polansky D., Rogerson D. J., “Development of a New Electronic Neutron Imaging System“, Nucl. Instr. and Meth. A 424(1999) pp. 9-14
2. Kim K. H., Klann R. T., Raju B. B., “Fast Neutron Radiography for Composite Materials evaluation and Testing”, Nucl. Instr. and Meth. A 422(1999) pp. 929-932
3. Vonotobel P., Frei G., Brunner J., Gildemeister A. E., Engelhardt M., "Dynamic Imaging with a triggered and Intensified CCD Camera System in a High-Intensity Neutron Beam", Nucl. Instr. and Meth. A 542(2005) pp. 148-153
4. Haan V. O de., Hagen T. H. J. J. van der, Fedorov A., Veen A. van, Leege P. F. A. de, “Conceptual Design of a Novel High-Frame-Rate Fast-Neutron Radiography Facility”, Nucl. Instr. and Meth. A 539(2005) pp. 321-334
5. Overley J. C., "Determination of H, C, N, O Content of bulk materials from neutron-Attenuation measurements", Int. J. Appl. Radiat. Isot. Vol. 36, No. 3(1985), pp. 185-191
6. Overley, J.C., "Element-Sensitive Computed Tomography with Fast Neutrons", Nucl. Instr. and Meth. B 24/25 (1987) pp. 1058-1062
7. Overley, J.C., "Explosives detection through Fast-Neutron Time-of-Flight Attenuation Measurements", Nucl. Instr. and Meth. B 99 (1995) pp. 728-732
8. Lefevre H.W., Chmelik M.S., Rasmussen R.J., Schofield R.M.S., Sieger G.E., and Overley J.C., "Using a Fast-Neutron Spectrometer System to Candle Luggage for Hidden Explosives. Can it be Made Practical for First-Line Airport Use? http://darkwing.uoregon.edu/~lefevre/Atcity.html
9. Overley J.C., Chmelik M.S., Rasmussen R.J., Sieger G.E, Lefevre H.W, " Results of Blind Tests for Explosives in Luggage Using Fast-Neutron Transmission Spectroscopy (FNTS)", http://darkwing.uoregon.edu/~lefevre/faatalk1.html
10. http://www.tensor-technology.com/Papers-public/High%20Speed%20Data%20Acquisition%20for%20Contraband%20Detection.doc
11. National Materials Advisory Board Report, "The Practicality of Pulsed Fast Neutron Transmission Spectroscopy for Aviation Security", NNMAB-482-6 Washington, D.C. 1999, http://www.nap.edu/books/030906449X/html/R1.html

12. Tensor Technology., "Multi-dimensional neutron radiometer ("MDNR")", private communication
13. Dangendorf V., Laczko G., Reginatto M., Vartsky D., Goldberg M., Mor I., Breskin A., Chechik R., "Detectors for Time-of-Flight Fast-Neutron Radiography 1. Neutron-Counting Gas Detector", Nucl. Instr. and Meth. A 542(2005) pp. 197-205
14. Dangendorf V., Kersten C., Laczko G., Vartsky D., Mor I., Goldberg M. B., Feldman G., Jaguztky O., Spillman U., Breskin A., Chechik R., "Detectors for Energy Resolved Fast Neutron Imaging", Nucl. Instr. and Meth. A 535(2004) pp. 93-97
15. Dangendorf V., Kersten C., Laczko G., Vartsky D., Mor I., Goldberg M. B., Feldman G., Jaguztky O., Spillman U., Breskin A., Chechik R., "Time Resolved Fast Neutron Imaging: Simulation of Detector Performance", Nucl. Instr. and Meth. A 542(2005) pp. 206-212
16. Jagutzki O., Lapington J. S., Worth L. B. C., Spillmann U., Mergel V., Schmidt-Böcking H., "Position sensitive anodes for MCP read-out using induced charge measurement", Nucl. Instr. and Meth. A 477(2002) pp. 256-261
17. Knoll G. F., "Radiation Detection and Measurement", John Wiley and Sons
18. Matsubayashi M., Soyama K., "Preliminary examination f a CCD camera with a scintillator coated fiber optic plate for neutron imaging", Nucl. Instr. and Meth. A 529 (2004) pp. 384-388
19. Bogolubov E., Bugaenko O., Kuzin S., Mikerov V., Monitch E., Monitch A. and Pertsov A., " CCD detectors for fast neutron radiography and tomography with a cone beam", Nucl. Instr. and Meth. A 542 1-3 (2005) pp. 187-191
20. Watterson J. I.., Ambrosi R. M., "Some fundamental considerations in resonance imaging using fast neutrons", Nucl. Instr. and Meth. A 513 (2003) pp. 367-373
21. Lehmann E. H., Vontobel P., Frei G., Bronnimann C., "Neutron imaging-detector options and practical results", Nucl. Instr. and Meth. A 531 (2004) 228–237
22. Ambrosi R. M., Fraser G. W., Feller B., Street R., Watterson J. I. W., White P., Downing G., "Large area microchannel plate detector with amorphous silicon pixel array readout for fast neutron radiography", Nucl. Instr. and Meth. A 500 (2003) 351–361
23. Ambrosi R. M., Fraser G. W., Street R., Watterson J. I. W., Lanza R. C., Dowson J., Abbey A. F., Feller B., Downing G., W., White P., Stevenson T, "Design of a

prototype microchannel plate detector with cooled amorphous silicon array readout for neutron radiography", Nucl. Instr. and Meth. A 542 (2005) 271–278

24. J. I. W., Ambrosi R. M., "Some fundamental considerations in resonance imaging using fast neutrons", Nucl. Instr. and Meth. A 513 (2003) 367–373
25. Brede H. J., Dietze G., Kudo K., Schrewe U. K., Tancu F., Wen C., "Neutron Yields from thick Be targets bombarded with deuterons or protons", Nucl. Instr. and Meth. A 274 (1989) 332–344
26. Dangendorf V., Kersten C., Laczko G., Jaguztky O., Spillman U., "Fast Neutron Resonance Radiography in a Pulsed Neutron Beam", http://arxiv.org/abs/nucl-ex/0301001
27. Leung K. N., Reijonen J., Gicquel F., hahto S., Lou T. P., "Compact Neutron Generator Development and Applications", http://www.ndt.net/article/wcndt2004/pdf/radiography/706_leung.pdf
28. Lou T. P., " Compact D-D/D-T Neutron Generators and Their Applications", http://repositories.cdlib.org/lbnl/LBNL-52766
29. Brzosko J. S., Robouch B. V., Ingrosso L., Bortolotti A., Nardi V., ”Advantages and Limits of 14-MeV Neutron Radiography”, Nucl. Instr. and Meth. B 72(1992) pp. 119-131
30. Buffler A., “Contraband Detection with Fast Neutrons”, Rad. Phys. and Chem. 71(2004) pp. 853-861
31. Shea P., Gozani T., "A TNA explosives detection system", Nucl. Instr. and Meth. A 299 (1990) 444–448
32. Gozani T., Elsalim M., Ingle M, Phillips E., "Gamma ray spectroscopy features for detection of small explosives", Nucl. Instr. and Meth. A 505 (2003) 482–485
33. Gozani T., Sawa Z. P., Shea P., "Apparatus and method of detecting contraband using fast neutron activation", US patent no.: 5,098,640, March 199
34. Gozani T., "Understanding the physics limitations of PFNA — the nanosecond pulsed fast neutron analysis", Nucl. Instr. and Meth. B 99 (1995) 743–747
35. National Materials Advisory Board, "Assessment of the Practicality of Pulsed Fast Neutron Analysis for Aviation Security", http://www.nap.edu/openbook/NI000414/html/2.html
36. National Materials Advisory Board Report, "Assessment of the Practicality of Pulsed Fast Neutron Analysis for Aviation Security", National academy press -482-6 Washington, D.C. 1999 http://www.nap.edu/openbook/NI000414/html/index.html

37. Rynes J., Bendahan J., Gozani T, Loveman E., Stevenson J., Bell C., "Gamma-ray and neutron radiography as part of a pulsed fast neutron analysis inspection system", Nucl. Instr. and Meth. A 422 (1999) 895–899
38. Hai-feng S., Fu-li W., Lin-mao L., Hai-jun S., "Novel applications of fast neutron interrogation methods", Nucl. Instr. and Meth. B 239 (2005) 202–208
39. Western Kentucky University, "PFTNA", http://www.wku.edu/API/research/pftna/pftna.htm
40. Vourvopoulos G., Womble P. C., "Pulsed fast thermal neutron analysis: a technique for explosives detection", Talanta 54(2001), 459-468, http://www.wku.edu/API/publications/Talanta2001PELAN.pdf
41. Womble P. C., Campbell C., Vourvopoulos G., Paschal J., Gacsi z., Hui S., "Detection of explosives with the PELAN system", Appl. of Accel. in Res. and Ind.-Sixteenth Int'l. Conf., American Institute of Physics 0-7354-0015 (2001), http://www.wku.edu/API/publications/CAARI2001PELAN.pdf
42. Buffler A., Brooks F. D., Allie M. S., Bharuth-ram K., Nchodu M. R., "Material classification by fast neutron scattering", Nucl. Instr. and Meth. B 173 (2001) 483–502
43. Brooks F. D., Buffler A., Allie M. S., Bharuth-ram K., Nchodu M. R., Simpson B. R. S., "Determination of HCNO concentrations by fast neutron scattering analysis", Nucl. Instr. and Meth. A 410 (1998) 319–328
44. Baffler A., "Contraband detection using neutrons", http://www.phy.uct.ac.za/people/buffler/FNSA.pdf
45. Chen G., Lanza R. C., "Fast Neutron Resonance Radiography for Elemental Imaging: Theory and Applications", IEEE TRANSACTIONS ON NUCLEAR SCIENCE, VOL. 49, NO. 4, AUGUST 2002 http://edwards1.phy.ohiou.edu/~inpp/nuclear_lunch/lanza-ieee-2002.pdf
46. Chen G., Lanza R. C., "Fast neutron resonance radiography for elemental mapping", United States patent 6,693,281, February 2004, Appl. No.: 039487
47. De Beers Cons mines LTD, Tapper U. A. S., Over G. W., "Neutron detection apparatus", Patent no.: WO0029873, May 2000
48. University of Witwatersand, Johannesburg, "Schonland research institute for nuclear sciences three year report", 1998-2000, http://www.src.wits.ac.za/pages/pub/AnnRep-98-99.doc

49. Van-staagen P. K., " High Speed Data Acquisition for Contraband Identification Using Neutron Transmission", ICAARI96, 1996, http://www.tensor-technology.com/Presentations-public/High%20Speed%20Data%20Acquisition%20for%20Contraband%20Identification%20Using%20Neutron%20Transmission.PPT
50. http://www.pma.caltech.edu/~ph77/labs/exp13.pdf
51. Nuclear Data Evaluation Lab., Korea Atomic Energy Research Institute, ENDFPLOT 2.0,ENDFB-VI http://atom.kaeri.re.kr
52. Eljen Technology, "EJ-200 plastic Scintillator", http://www.apace-science.com/eljen/ej-200.htm
53. Saint-Gobain crystals and detectors, "Scintillating optical fibers brochure", http://www.detectors.saint-gobain.com
54. Kirkbride J., Yates E. C., Crandall D. G., "Measurement of the decay times of organic scintillators", Nucl. Instr. and Meth. 52 (1967) 293-297
55. Yates E. C., Crandall D. G., "Decay times of commercial organic scintillators", IEEE Trans. Nucl. Sci. NS-13, no. 3 (1966) 153-158
56. GEANT 3.21, detector description and simulation tool, CERN program library long writeupW5013, CERN, Geneva, 1993
57. Fiberoptics Technology Incorporated, "Numerical aperture", http://www.fiberoptix.com/technical/numerical-aperature.html
58. Saint-Gobain crystals and detectors, "Scintillating optical fibers brochure", http://www.detectors.saint-gobain.com
59. Praezions Glas & Optik , SHD, dielectric front surface mirror, http://www.pgo-online.com/intl/katalog/shd.html
60. Photek limited, "MCP240 specification sheet", private communication
61. Andor Technology, ”ICCD detectors, course notes”, Nov.2003, http://www.lot-oriel.com/site/site_down/cc_notesiccd_deen.pdf
62. Dangendorf V., Weiergans M., "Trigger unit for image intensifier", private communication, PTB 2005
63. Dangendorf V., "Technical specification of components for high speed photocathode pulsing system", private communication, Sep. 2004
64. PCO computer optics, "Optiche Abbildung mit Einzel-und Tandemobjectiven", private communication

65. Photonics, "Vignetting", http://www.photonics.com/dictionary/lookup/XQ/ASP/url.lookup/entrynum.5594/letter.v/pu./QX/lookup.htm
66. http://www.usaerialphotos.com/default2.asp?show=glossary
67. Optics Bench Appelet, http://www.hazelwood.k12.mo.us/~grichert/optics/intro.html
68. Eastman Kodak company, "KAF-1600 Full Frame CCD Image Sensor Performance Specification", Rev. 2, 2005, WWW.kodak.com/go/imagers
69. Eastman Kodak company, "KAF Series Full-Frame CCD Sensors Binning Mode Operation", WWW.kodak.com/go/CCD
70. DTA Scientific Instruments, "CCD camera performance test (v 1.4)", private communication, Pisa 2003
71. Masschaele B., Dierick M., Hoorebeke L. V., Jacobs P., Vlassenbroeck J., Cnudde V., "Neutron CT enhancement by iterative de-blurring of neutron transmission images", Nucl. Instr. and Meth. A 542 (2005) 361–366
72. Saito Y., Mishima K., Matsubayashi M., Lim I. C., Cha J. E., Sim C. H., "Development of high-resolution high frame-rate neutron radiography", Nucl. Instr. and Meth. A 542 (2005) 309–315
73. Fischer R.E., Tadic-Galeb B., "Optical Systems Design", Mcgraw-Hill, pp.193-194
74. Nikon, microscopyU,"Modulation Transfer Function", http://www.microscopyu.com/articles/optics/mtfintro.html
75. Delft Electronic Products B.V.," Tube performance that matters", http://213.210.6.54/dvsmil/perfdata/DEP-XD4-Tube-performance-2.pdf
76. Logory L. M., Farley D. R., Conder A. D., Belli E. A., Bell P. M., miller P.L., "Characterization of an X-ray framing camera utilizing a charge coupled device or film as recording media", Review of scientific instruments 69(1998)
77. Janni J. F., "Proton range-energy tables, 1 keV-10 GeV", Atomic data and Nuclear data tables Vol. 27 (1982) 304-305
78. Andor Technology, "Ultra-fast spectroscopy and imaging with ICCD detectors", http://www.lot-oriel.com/site/site_down/cc_workshopiccd_deen.pdf
79. http://www.microscopyu.com/tutorials/java/digitalimaging/signaltonoise/index.html
80. Mandel L., "Image fluctuations in cascade intensifiers", British Journal of Applied Physics vol. 10, 233-234
81. MITRE Corp., "Modulation Transfer Function (MTF) Method", http://www.mitre.org/tech/mtf/

82. Roper Scientific, “Introduction to Image Intensifiers for Scientific Imagining”, http://www.princetoninstruments.com/pdfs/technotes/intensifiers.pdf
83. Proxitronic, “High performance image intensifiers”, http://www.proxitronic.de/dnload/ebv.pdf
84. Harmer S. W., Townsend P. D., “Absorption of Optical Power in an S-20 Photocathode”, www.iop.org/EJ/article/0022-3727/36/13/308/d31308.pdf
85. http://www.photek.com/Datasheets/Phosphors.pdf
86. http://internal.physics.uwa.edu.au/~andrew/MyThesis.pdf
87. Vista 1.73 imaging program main Help file by DTA S.R.L, http://www.dta.it/support/manuals/cx3_3p.pdf
88. http://micro.magnet.fsu.edu/primer/digitalimaging/concepts/ccdsnr.html
89. http://www.kodak.com/global/plugins/acrobat/en/digital/ccd/applicationNotes/noiseSources.pdf
90. http://www.pco.de/download/?url=%2Fdata%2Ffilemanager%2Fpco_kb_noise_general_0902.pdf
91. http://www.ph.tn.tudelft.nl/Courses/FIP/noframes/fip-Contents.html
92. Trondsen T., "High spatial and temporal auroral imaging", university of Tromso, http://www.phys.ucalgary.ca/~trondsen/Trondsen_Dissertation_1998/Trondsen_Dissertation_1998.pdf
93. http://www.ccd.com/ccd108.html
94. http://solar.physics.montana.edu/YPOP/Nuggets/2000/001201/001201.html
95. http://micro.magnet.fsu.edu/primer/digitalimaging/concepts/dynamicrange.html

Appendix

Appendix 1 - Description of the optical alignment procedure

The optical alignment procedure is used to align all detector components along the same optical axis and to center the detector on the axis of the accelerator beam. For this purpose, a laser beam and two variable-aperture irises are employed, as can be seen in fig. A-1.

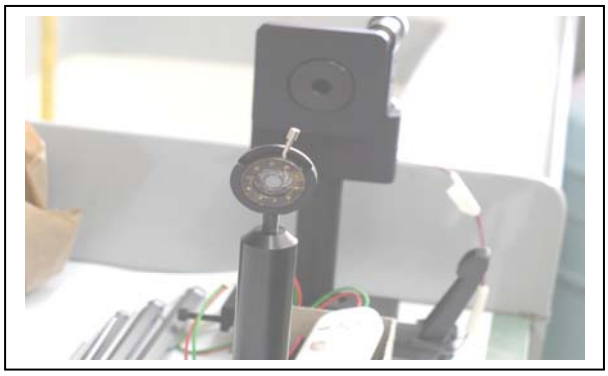

Fig. A-1: The laser mount and variable aperture iris

Fig. A-2 & A-3 show an illustration of the TRION imaging system and alignment geometry, respectively. All optical components are positioned on a rail and also have some mechanical degrees of freedom for accurate alignment.

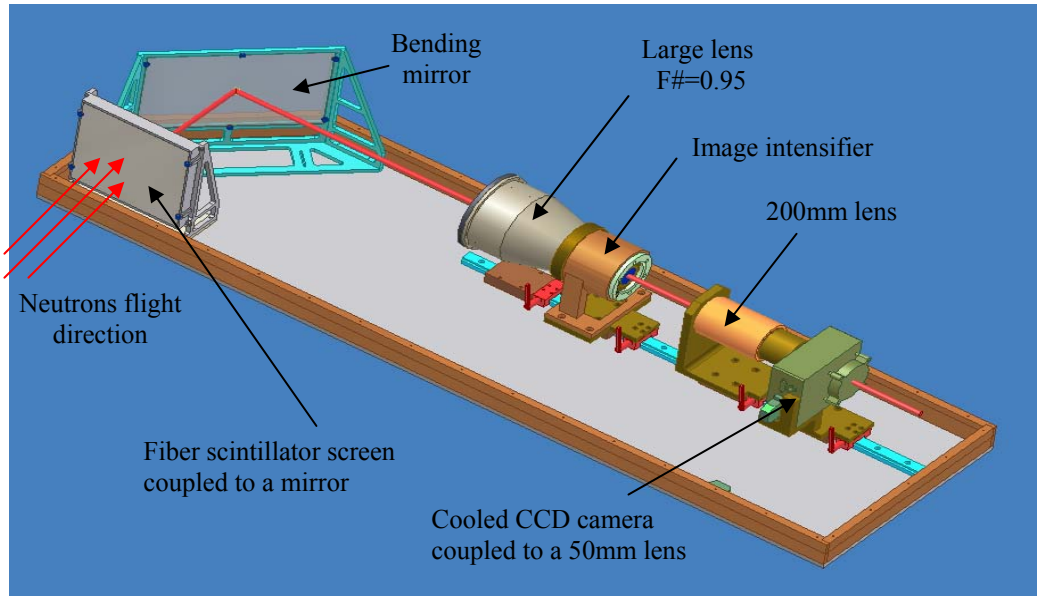

Fig. A-2: An illustration of the TRION detection system

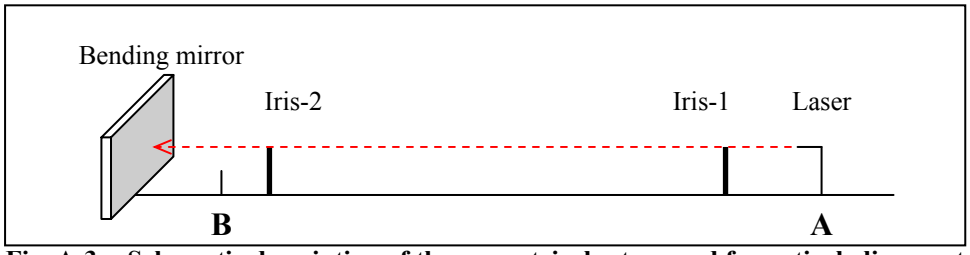

Fig. A-3: Schematic description of the geometrical setup used for optical alignment (not to scale)

The alignment procedure begins with all components removed, except for the laser and two irises.

The following provides a step-by-step description of the optical alignment procedure:

1) The laser mount (oriented towards the bending mirror) is manipulated until the laser beam passes through the exact center of both irises which are closed to a minimal aperture at a height that is determined with high precision. The two irises thus define the optical axis.
2) The bending mirror, oriented at 45^{o} relative to the neutron beam flight path, is then mounted. Upon activation of the laser, the mirror is manipulated to the point that the laser beam hits the center of a mirror placed instead of the scintillator screen (henceforth referred to as the scint.-mirror).
3) The alignment of the scint.-mirror is carried out such that the reflection of the incident laser beam is directed to the center of iris-2, as illustrated in fig. A-3.
4) The laser is moved to position B, pointing at iris-1. The laser beam should pass through the centers of both irises. The location of the incident beam spot is marked at a large distance from iris-2 for future reference.
5) The large lens (120 mm F#=0.95) is mounted and aligned, such that the laser spot is coincides with the previously marked reference point.
6) The 200 mm (F#=2.8) lens is then mounted. The procedure described in step 5 is repeated.
7) Finally, the CCD camera coupled to the 50 mm (F#=1.2) lens is mounted. The laser spot is captured by the CCD (for a very short exposure duration) and its location is verified by examination of its coordinates in the image reference system. If required, the camera position can be adjusted.
8) The detector assembly is positioned on a table of adjustable height. The scintillating screen is replaced with a mirror which is mounted with the reflective surface facing the accelerator. The detector is positioned such that a laser spot, representing the accelerator beam axis, is in the center of the mirror and its reflection is also on the laser axis. The axis of the accelerator beam is known from prior usage of this laser beam for the alignment of the accelerator beam.

Appendix 2 - Description of image intensifier

An image intensifier is a vacuum tube device comprised of a photo-cathode input, multi-channel plate (MCP) or more and a phosphor screen.

The photo-cathode input is a coating of multi-alkali or semi-conductor layer on the inside of the input window. The phosphor screen is a fluorescent phosphor coating on the inside of the output window and the MCP is a complex electron-multiplying micro-channel plate

When the photocathode is biased more positively than the MCP, electrons will not enter the MCP and the MCP is gated off. If the photocathode is negatively biased, electrons will be accelerated into the MCP and the intensifier is gated on.

The image intensifier employed in TRION is 40 mm in diameter, capable of amplification of up to 1E6 W/W at 500 nm at 1600V MCP, containing double MCP's, a low noise S20 (Na_2-K-Sb(Cs)) photocathode, a P43 (Gd_2O_2S:Tb) anode.

Image intensifier mode of operation

As illustrated in fig. A-4, a portion of the incident light photons striking the photocathode causes the release of electrons via the photoelectric effect*. These electrons are then accelerated (by a voltage of –150 V) towards the MCPs, where they are multiplied and accelerated again (under a voltage of +3900 V) toward the phosphor screen.

These electrons strike the phosphor screen and cause the emission of fluorescence photons. Thus, for every photon releasing an electron from the photocathode, large number of photons (by several orders of magnitude) are emitted from the phosphor screen.

At very low illumination levels there is no continuous illumination but a 'hail like' bombardment by single photons. Consequently, the noise component in the image increases to the extent that small details will not be distinguishable from the background; the resolution will be dependent on the light level. This regime is called the *'low light level'* or *'shot noise limited'* regime [75]. If there is enough light, the noise level will decrease, image quality will improve and will no longer depend on the illumination intensity.

* The photoelectric effect represents the emission or ejection of an electron from the surface (the photocathode in this case) in response to an incident photon of sufficient energy to overcome the binding energy of the electron

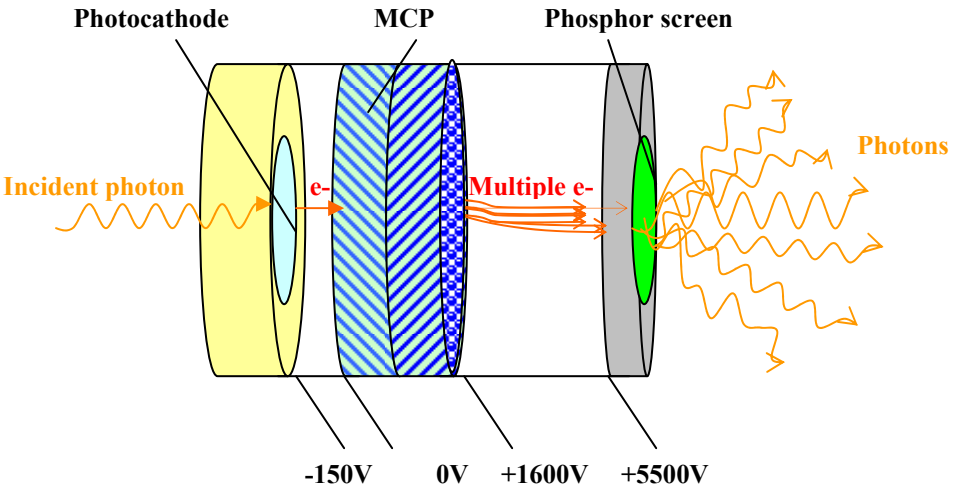

Fig. A-4: Schematic description of an image intensifier (not to scale). An incident light photon striking the photocathode causes the release of an electron via the photoelectric effect. This electron is accelerated towards the MCP, where it is multiplied and accelerated again toward the phosphor screen. These electrons strike the phosphor screen, causing the emission of fluorescence photons.

Fig. A-5 shows that the limiting resolution at low light levels is dependent on the illumination, while at higher levels it is constant.

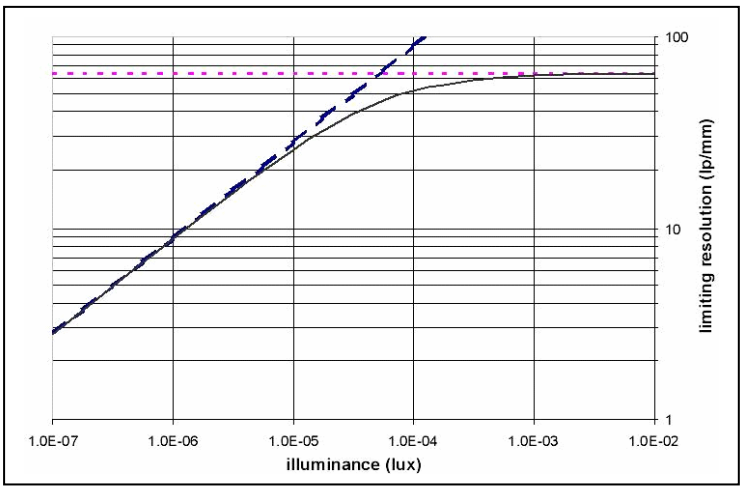

Fig. A-5: The limiting resolution as a function of illuminance [60]

Image intensifier principal components:

The Photocathode:

The photocathode [82] is the first major component in an image intensifier. The photocathode coating converts a portion of the incident light photons into electrons. Photons not captured by the photocathode do not contribute to the final signal. Therefore

the quantum efficiency (***QE***), defined as the percentage of incident photons converted to electrons, is very important for image intensifiers.

The ***QE*** may be calculated [83] from the spectral sensitivity ***S*** and the wavelength ***λ***, as follows:

$$QE[\%] = S[mA/W]\frac{124}{\lambda[nm]} \qquad \text{[A-1]}$$

The S-20 photocathode is highly absorbing [84] at short wavelengths (350–500 nm), but as displayed in the spectral response of the LNS20 (see fig. A-6), the sensitivity rapidly decreases for light of longer wavelength. In fact, at a wavelength of 900 nm the S-20 photocathode is practically transparent.

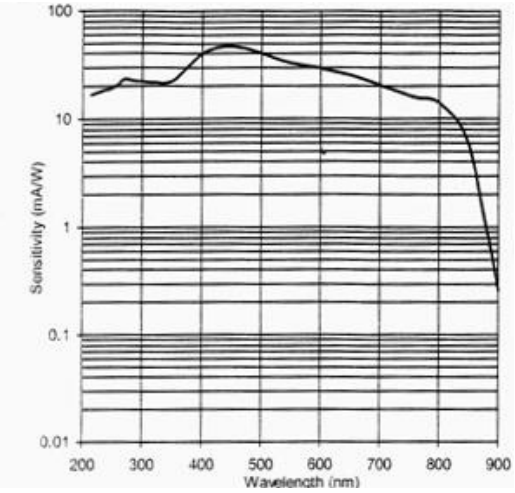

Fig. A-6: Spectral response of the LNS20 photocathode present in the TRION system

The Multi-Channel Plate (MCP) [82]:

The MCP is the second and most sophisticated component of an II. It is a slightly conductive glass substrate with millions of parallel traversing channels. These channels contain a secondary electron emitter (such as CsI, CuI) and are arranged in a hexagonal pattern with 6-15 μm center-to-center spacing.

Electrons generated at the photocathode are driven through the channels by a constant electric field resulting from a voltage of 1.6 kV applied on the MCP. A portion of these electrons strike the walls of the channel and cause the formation of many additional electrons. A single electron may undergo multiple collisions producing many thousands of electrons which leave the plate, as illustrated by fig. A-7.

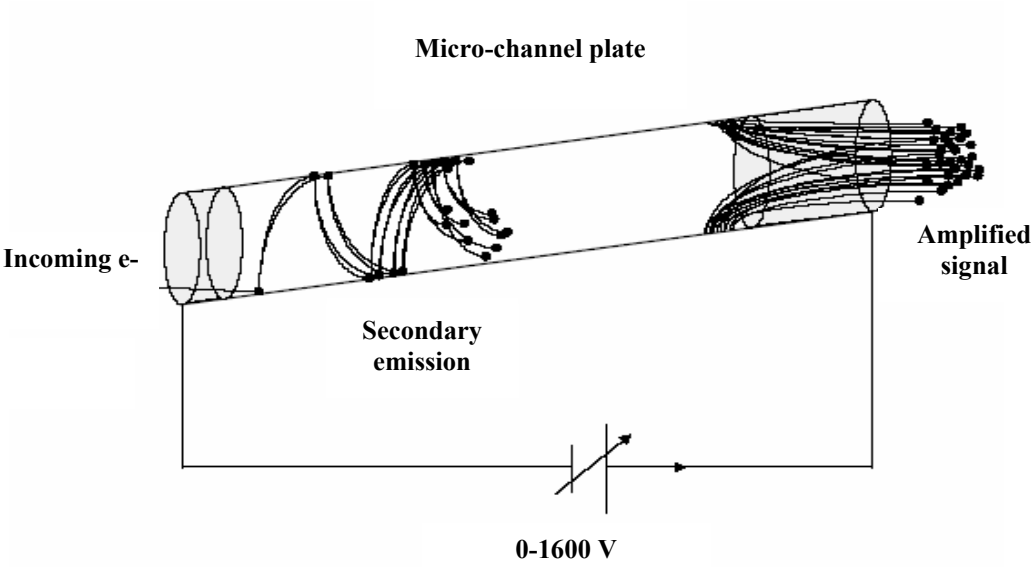

Fig. A-7: An electron passing through the channels strike the walls and cause the formation of many additional electrons. A single incident electron may undergo multiple collisions producing many thousands of electrons which leave the plate towards the phosphor screen

The MCP web-like entrance surface is generally coated with Ni-Cr which has a low secondary electron emission coefficient. Consequently, electrons missing the channels and striking the entrance surface (comprising close to 55% of the MCP surface area) create secondary electrons, some of which are then pulled into nearby channels by electrostatic forces. This allows the recovery of electronic charge that would otherwise be lost by electrons missing channel apertures. In essence, each MCP acts analogously to a standard photomultiplier device, but it also possesses imaging capabilities due to the fact that position information is maintained.

Phosphor screen:

The third major component of an II is the phosphor screen, which is a phosphor coating on the inside of a fiber-optic exit window. Electrons exiting the MCP are accelerated (under voltage of +3900V) toward the phosphor screen, where they are converted back into light photons to be registered by the CCD.

Phosphors usually emit green light and are made of rare earth oxides or halides (e.g. Gd, Ln, Tb) with decay times ranging from a few hundred nano-seconds to a few milliseconds. An example can be seen in fig. A-8, which displays a phosphor

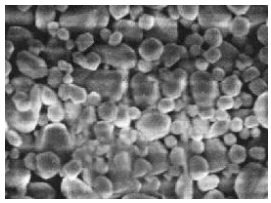

Fig. A-8: Gd oxysulphide crystals shown at × 10,000 magnification [51]

composed of Gd-oxysulphide crystals at ×10,000 magnification.

Selected properties of P43 (Gd_2O_2S:Tb) phosphor [85], which is a constituent of the image intensifier utilized by the TRION system, are presented in table A-1 and in figs. A-9 & A-10.

Table A-1: P43 phosphor properties [85]

Type, Colour	Efficiency %, Optical Watts/Electrical Watts	Peak wavelength (nm)	Photons/Electrons @ 6kV	Decay characteristics
P43, Green	8.7	548	240	1.2 ms/decade, true exponential

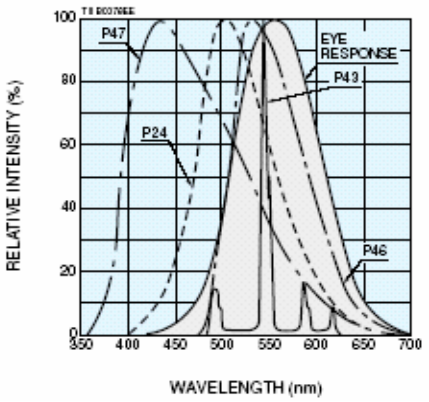

Fig. A-9: Typical phosphor spectral emission characteristics [55]

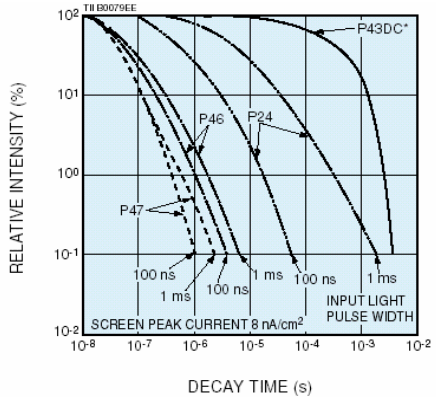

Fig. A-10: Typical phosphor decay characteristics [55] * P43 decay time obtained following removal of the continuous input light source

Appendix 3 - Charge Coupled Device - CCD camera

CCDs are very sensitive light imaging detectors, providing dynamic range and sensitivity far greater than photographic emulsions [86].

A CCD is basically composed of three layers: a substrate of p-type silicon overlaid with an insulating layer of silicon oxide and an electrode pattern over the silicon oxide.

As can be seen in fig. A-11, insulating strips are doped into the silicon, forming a grid of conductive channels in the substrate at right angles to the electrode strips on the surface. During the collection of an image, some of the electrodes on the surface are raised to a potential of ~ +10 V while the rest remain at ~0 V. No current flows to the substrate because of

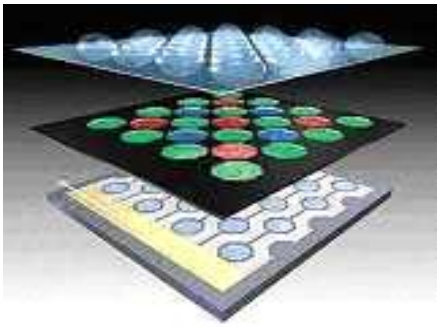

Fig A-11: An outline of CCD layers. The bottom layer is made of silicon doped with insulating strips. The middle layer is made of silicon oxide and the top is an electrode pattern

the insulating oxide layer. However, the electric field creates a depletion region under the charged electrode, because the dominant charge carriers in the p-type substrate ('holes') are positively charged.

As described in fig. A-12, when a photon is absorbed in the substrate, it creates an electron-hole pair. If the absorption occurred in the depletion region, the original electron and hole separate. The photo-electrons drift towards the surface of the CCD and collect at the positively charged electrodes. Lateral motion is prevented by the insulating strips doped into the substrate at right angles to the electrodes.

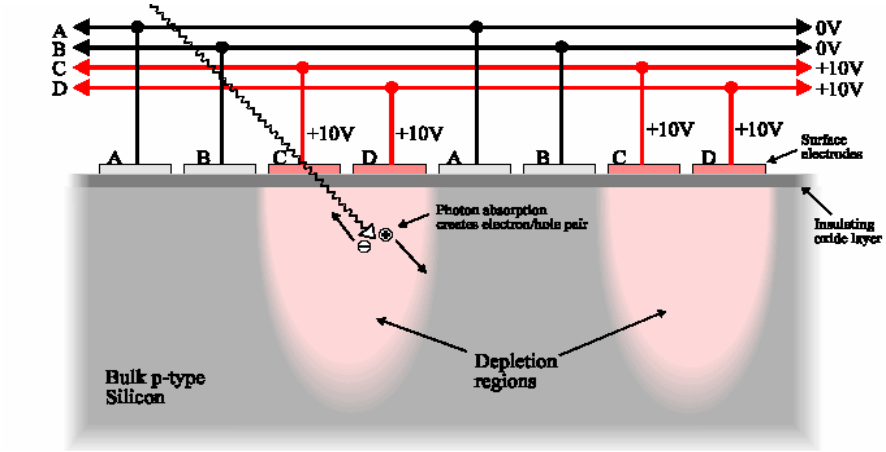

Fig. A-12: shows a simplified cross-section of a typical CCD. An array of transparent electrodes on the surface is wired to four output pins (A, B, C, D). During image capture, two of these pins are held at +10V, causing a series of isolated depletion regions. Photon capture in the bulk silicon creates electron-hole pairs, with the electrons diffusing towards the depletion region, and the holes moving away.

The maximum amount of electrons that a pixel can contain is termed *Full-Well Capacity* (*FWC*). When a pixel reaches its limit, a state referred to as "*saturation*", the excess charges overflow to the adjacent pixels producing a *blooming effect*.

Fig. A-13 provides a schematic description of the charge transport process in a CCD. The integrated charge from each pixel is transported to the output using a two-step process. When operating in a normal or non-binning mode, each line (row) of charge is first transported from the vertical CCD's to the horizontal CCD register using two register clocks. The line of charge is then serially shifted to the floating diffusion output node, pixel by pixel. The charge of each pixel is converted into a voltage and sensed off chip.

The CCD sensor used in our imaging system is a KAF 1602E [68-69] having 1524 (H) × 1536 (V) photoactive pixels of 9 μm × 9 μm, photosensitive area of 13.8 mm (H) × 9.2 mm

(V), FWC of 100,000 e-. When operating at room temperature a 74 dB dynamic range can be obtained.

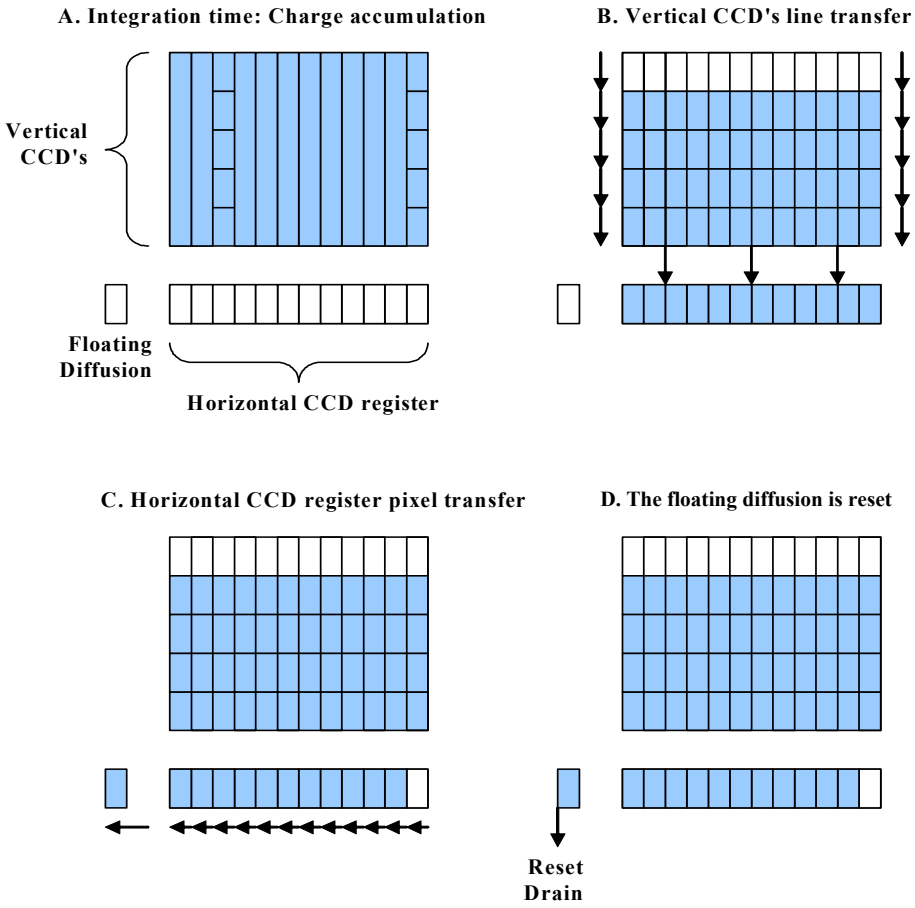

Fig. A-13: Schematic description of charge transport process: A) Charge is accumulating in the vertical CCD's during exposure. B) Vertical CCD line is transferred to the horizontal CCD register. C) First CCD horizontal pixel is transferred to the floating diffusion. D) The floating diffusion is reset

CCD quantum efficiency (QE)

Quantum efficiency [87] is of high importance for a CCD sensor, as it expresses its efficiency, i.e., the capacity to capture the incoming photons and convert them to photo-electrons that determine the outgoing signal. It is expressed in percent for a given wavelength. For instance, a value of 40% means that, of 100 photons striking the sensor, 40 will be captured and converted to photo-electrons.

Fig. A-14 displays the spectral response for the Kodak KAF 1602E CCD sensor, used by the TRION system. The image intensifier phosphor emits photons of 548 nm which translates to ~38% CCD quantum efficiency.

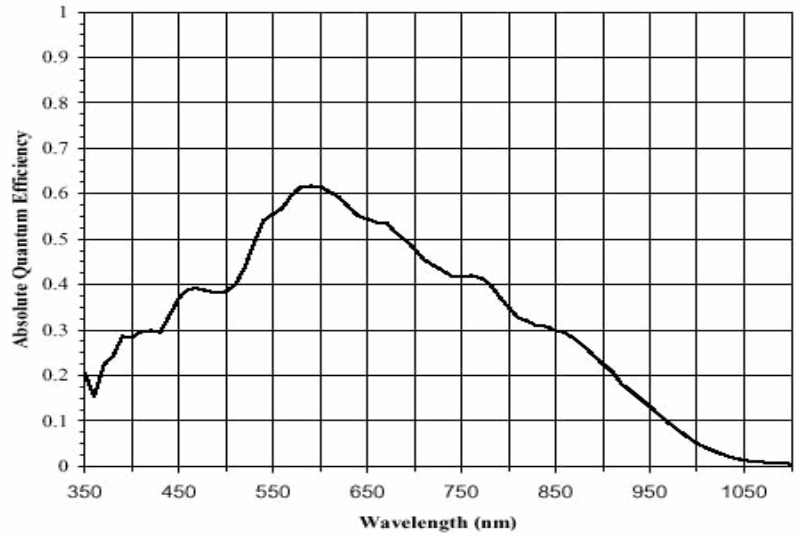

Fig. A-14: Spectral response of the KAF 1602E CCD sensor

Appendix 4 - Various noise sources affecting image quality

Noise is an undesired signal, which is either contained in the relevant light signal or added to it by the imaging process. The presence of noise degrades image quality by limiting the accuracy of read signals. The following provides a description of dominant noises present in each of the images taken by the TRION imaging system.

When examining noise generation, the Signal to Noise Ratio (SNR) of the digital radiographic system is predominantly affected by the neutron source, CCD camera and the image intensifier.

The main noise sources governing image-quality are: *neutron shot noise*, *photon shot noise*, *image intensifier thermal noise* and *CCD noise*.

CCD noise sources

A detailed engineering consideration of noise contributions in charge-coupled devices includes many sources that are normally handled by combining them into more general categories or which are not significant except at low signal.

The three primary components of noise in a CCD system are *photon shot noise*, *dark noise* and *read-out noise*, all of which must be considered in a calculation of the signal-to-noise ratio (SNR).

Noise sources can be also classified by their domains [88]: *temporal* or *spatial*. By definition, *temporal* noise varies with time and can be reduced by frame averaging,

whereas *spatial* noise cannot. *Spatial* noise can be partially removed by various frame subtraction algorithms.
The *temporal* noise category includes: *photon shot noise* and *dark current noise*.
The *spatial* noise category includes: *photo response non-uniformity* and *dark current non-uniformity*, which are both sources that produce non-uniformity in the pixel output.

During image acquisition with electronic sensors, including CCDs, noise superimposed on the signal is manifested as apparent random fluctuations in signal intensity. As the noise magnitude increases, the uncertainty in the measured signal becomes greater.
Signal-to-noise ratio (SNR) is typically evaluated in terms of the three primary noise categories mentioned above, each category encompassing several contributing noise mechanisms (discussed in following sections).
The CCD imaging signal depends upon the *photon flux* incident on the CCD photodiodes (expressed in [photons/pixel/sec]), the *Quantum Efficiency* (*QE*) of the device and the image integration time. The product of these three variables determines the signal portion (numerator) which should be weighed against all noise sources (contributing to the denominator) that degrade the image quality.

The following section will provide a description of the primary CCD noise sources as well as noise sources of lesser significance.

Photon shot noise (n_{shot})
Photon shot noise [89-92] is intrinsic to the "steady" emission of photons. This stochastic process is governed by Poisson statistics. Thus, the uncertainty in the number of photons collected during a given period of time (termed *photon shot noise*) is directly proportional to the number of photons arriving at the detector N during the same time interval, according to the Poisson distribution:

$$P(N) = \frac{\overline{N}^{N}}{N!} e^{-N^{\overline{N}}} \qquad \text{[A-2]}$$

The Poisson distribution has a variance equal to its mean $\overline{N}$.

While the number of photons arriving at the detector is governed by Poisson statistics, the conversion of photons into photoelectrons in a photosensitive medium follows the

Bernoulli distribution [92]. The Bernoulli distribution mean is η, representing the probability that a photon is successfully converted into a photoelectron, better known as the detector *Quantum Efficiency* (*QE*).

The Poisson statistics of the incoming photons is transferred to the photoelectrons, resulting in a photoelectron distribution with a mean of $\eta \overline{N}$.

Photo Response Non-Uniformity (PRNU)

Not all pixels demonstrate the same sensitivity to light due to production process variations or non-uniform illumination caused by imperfect optics (vignetting, etc.). The result at the individual pixel-to-pixel level is a faint checkerboard pattern seen when examining a flat-field image (an image of a uniformly lit screen). Usually this variation is of the order of one or two percent of the average signal [88-89], and is linear with the average signal.

The pattern caused by the sensitivity variation can be removed by *'flat-fielding'*, a process which involves the normalization of an image by a flat-field image, resulting in the correction of the pixel-to-pixel non-uniformity [88-89].

Readout noise (RN)

Readout noise [21,79,88-89] is a combination of system noise components inherent to the process of converting CCD charge carriers into a voltage signal for quantification, subsequent processing and analog-to-digital (A/D) conversion.

This noise, added uniformly to every image pixel and described by the number of electrons per pixel, is independent of exposure time. A typical readout noise distribution present in each of the images acquired by the Chroma C3 CCD camera can be seen in fig. A-15.

The major contribution to the readout noise usually originates from the on-chip preamplifier.

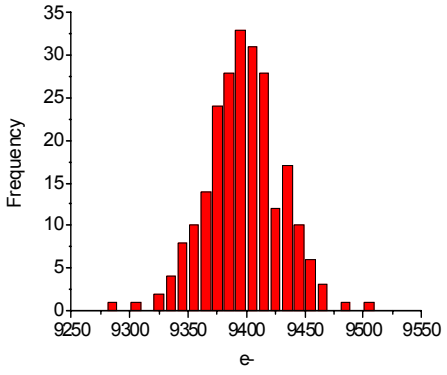

Fig. A-15: Readout noise distribution, in electrons (e-), obtained with the Chroma C3 CCD camera

Readout noise can be isolated and removed from a CCD image via the subtraction of a bias frame - the signal acquired by the camera in an exposure of zero duration without having been exposed to light. In this manner, thermal noise produced by the heat generated by the electronics of the camera is at a minimum, thereby isolating the

effect of readout noise. Since the readout noise varies from pixel to pixel and readout to readout, a number of such bias images should be recorded and then averaged together.

Quantization noise

The conversion of charge carriers into a voltage signal and the translation of the sensor output voltage into a sequence of digital numbers suitable for being processed by a computer, require an analog-to-digital converter (ADC). This processing chain produces *Quantization Noise* [89] which is uniformly added to the image.

The analog-to-digital converter performs a rounding off, dividing the signal into grayscale levels: 256 levels for 8 bits, 16384 for 14 bits and 65536 for 16 bits. As the number of levels increases, the introduced uncertainty decreases. The *quantization noise* (*QN*) can be described by [87]:

$$QN = FWC / (2^n * 3.464101515) \qquad \text{[A-3]}$$

Where ***FWC*** is the full well capacity for every single pixel (in number of electrons) and ***n*** is the number of bits provided by the ADC.

Dark noise

The generation of dark noise [88-89,93] is a thermal process wherein electrons use thermal energy to hop to an intermediate state, from which they are emitted into the conduction band. The generation rate of thermal electrons at a given CCD temperature is referred to as *dark current. Dark current* is the result of imperfections or impurities in sites such as depleted bulk silicon or at the silicon dioxide interface. These sites introduce electronic states in the forbidden gap which act as steps between the valence and conduction bands, providing a path for valence electrons to be promoted into the conduction band, adding to the signal measured in the pixel.

Dark current generates two types of noise: *dark current non-uniformity* and *dark current shot noise.*

Dark current non-uniformity [89,93]: Noise resulting from pixel-to-pixel variation of dark current, due to the fact that each pixel has slightly different dark current generation rates. This noise can be reduced or eliminated by cooling the CCD and subtracting a dark reference frame from each image. The dark reference frame should be taken at the same conditions (temperature, integration time) as the image.

Dark current Shot noise [88-89]: The shot noise component ($\sigma_{dark\ shot}$) is governed by Poisson statistics and is equal to the square root of the number of thermal electrons generated during image integration time, i.e. dark signal D_C:

$$\sigma_{dark\_shot} = \sqrt{D_C} \qquad \text{[A-4]}$$

Although the dark signal can be subtracted out, the shot noise associated with this signal cannot. The only option for reducing or eliminating dark current shot noise is cooling the CCD.

Shorted pixels

Shorted pixels continuously leak charge [94]. They give rise to a bright column of pixels extending over the entire length of the CCD.

Dynamic range

The dynamic range [95] of a Charge-Coupled Device (CCD) is typically specified as the maximum achievable signal divided by the camera noise, where the signal strength is determined by the full-well capacity (***FWC***), and the noise is the sum of dark and read noises. As the dynamic range of a device is increased, the ability to quantitatively measure the faintest intensities in an image is improved. The dynamic range ***DR*** is represented by the following [95]:

$$DR = 20 \times Log(FWC/N_{noise}) \qquad \text{[A-5]}$$

Where ***FWC*** is the full well capacity and N_{noise} is the sum of all noise contributions, both expressed in electrons.

Bit depth refers to the binary range of possible grayscale values utilized by the A/D converter to translate analog image information into discrete digital values capable of being read and analyzed by a computer. For example, 8-bit A/D converters have a binary range of 2^8 or 256 possible values while a 12-bit converter has a range of 2^{12} or 4,096 values, and a 16-bit converter has 2^{16}, or 65,536 possible values. The bit depth of the A/D converter determines the magnitude of the gray scale increments, with higher bit depths corresponding to a greater range of useful image information obtainable from the camera.

CCD noises summary

As mentioned previously, the three major sources of noise in a CCD system are *photon shot noise*, *dark noise* and *read-out noise*, all of which must be considered in the calculation of the signal-to-noise ratio. The less significant among them can be regarded as contributing to readout noise and dark noise

Due to the fact that photon noise is an inherent property of CCD signal detection, which cannot be reduced by camera design factors, it essentially represents a "noise floor" that is the minimum achievable noise level, diminishing in relative effect as photon flux increases. Consequently, it is desirable to operate an imaging system under conditions that are limited by photon noise, with other noise components being reduced to relative insignificance.

Under low illumination level conditions (assuming dark noise is essentially eliminated by CCD cooling), *readout noise* variance dominates over *photon shot noise* variance and the image signal is said to be *read-noise limited* [79]. The camera exposure time can be increased to collect more photons and increase SNR, until a point is reached, at which *shot noise* variance exceeds that of both *readout noise* and *dark noise*. At even longer exposure times, the image is said to be *photon-noise limited.*

Because of the square-root relationship of photon noise to signal, the demarcation line between the two regions (*photon noise* limited and *readout noise* limited) occurs at an exposure time for which the total detected signal per pixel is approximately the square of the readout noise value. For example, with a readout noise specification of 5 electrons RMS per pixel, photon noise becomes the dominant noise source when the exposure time is sufficient to result in more than 25 detected photons per pixel at the existing incident photon flux.

According to the above, the CCD SNR [79] can be described by:

$$SNR = \frac{\Phi_{ph} \cdot QE \cdot t}{\left(\Phi_{ph} \cdot QE \cdot t + D_C \cdot t + RN^2\right)^{\frac{1}{2}}} \qquad \text{[A-6]}$$

Where Φ_{ph} is the incident photon flux (photons/pixel/sec), QE represents the CCD quantum efficiency, t is the integration time (sec), D_C is the dark current value (electrons/pixel/sec) and RN represents readout noise (electrons rms/pixel).

Examination indicates that the above equation is simply structured as a ratio of total signal generated during the exposure time divided by the combined noise attributable to the three noise components described previously. The latter are not correlated, and the denominator incorporates appropriate values for each noise component: the square-root of the signal accounts for the *photon noise*, *dark noise* is equivalent to the square-root of the product of dark current and integration time.

Image intensifier noise sources at low light level

In a low light regime, the information density is mainly determined by the amount of noise present in the image. In addition to CCD noises, the image-intensifier constitutes a source of noise that cannot be neglected.

Noise performance of an image intensifier is affected by several factors [75]:

- Amount of available light: The noisiness is an inverse square root function of the light level (*photon shot noise*).
- Photocathode sensitivity: Not every incoming photon is converted into an electron. The quantum efficiency of photocathodes is in the range of 10% - 30%. A photon which is not converted into an electron does not contribute to the image, thus increases the noisiness above its theoretical minimum value.
- e- Trapping: The MCP adds to the noisiness of the image by trapping photoelectrons. These trapped electrons will not be amplified. This process gives rise to a substantial reduction in effective photocathode sensitivity.
- Gain: A higher gain of the image intensifier will not make the picture less noisy, it will only increase the intensity of the noise. Above a certain level, increase of gain will not help to improve performance.
- Equivalent Background Illumination (EBI) [75,78]: EBI is an inherent background noise of an image intensifier which sets the lower detection limit. It is normally specified as the input illuminance required to produce a luminous emittance from the phosphor screen equal to that obtained when the input illuminance is zero. The noise is almost entirely due to thermal electrons emitted by the photocathode and is therefore strongly dependent on photocathode temperature. EBI can be reduced by keeping the image-intensifier in darkness (for over an hour) and cooling the photocathode. At extremely low illumination levels the EBI adds haze to the image.

תקציר

PFNTS (Pulsed Fast Neutron Transmission Spectroscopy) הינה טכניקת רדיוגרפיה אשר מנצלת שינויים אנרגטיים אופייניים בחתך-הפעולה למטרת דימות מרחבי ספציפי ליסודות מסויימים. בשיטה זו, אלומת נויטרונים-מהירים בעלת ספקטרום אנרגטי רחב (0.8-10 MeV) העוברת דרך החפץ הנבדק, משתנה בהתאם לתנודות- בחתך הפעולה ("רזוננסים") עבור יסודות קלים כגון, C, N, ו- O, המצויים בו. בעזרת שיטת זמן-מעוף ((time-of-flight (TOF) נמדד ספקטרום הנויטרונים המועבר ע"י גלאי נויטרונים בעל רגישות למיקום ונקבעת ההנחתה המתאימה למרווחי זמן (חלונות אנרגיית נויטרונים) אשר נבחרו מראש.

לפיכך, PFNTS טומנת בחובה פוטנציאל לגילוי טווח רחב של חומרי נפץ קונבנציונליים ומאולתרים.

עד כה, גלאי PFNTS אשר פותחו ע"י אוניברסיטת Oregon וחברת Tensor Technology פעלו בשיטת מניית מאורעות בודדים (event counting) והגדירו פיקסל שגודלו לא היה קטן מ-10~ ס"מ^2. מגבלות אלו שללו אל הפעלת הגלאי בשטפים גבוהים ולא אפשרו גילוי אמין של אובייקטים קטנים מגודל הפיקסל.

מערכת TRION (Time Resolved Integrative Optical (readout for) Neutrons) המתוארת בעבודה זו, הינה גלאי יעיל בעל שטח גדול, המשמש לגילוי נויטרונים מהירים, תוך הצגת יכולות חסרות תקדים, כגון: דימות בקנה מידה תת-מילימטרי וספקטרומטריה בעזרת שיטת זמן-מעוף. בנוסף, מערכת זו מסוגלת לפעול ללא הפסדים בשדות מעורבים של נויטרונים- וקרני גאמא בעוצמות גבוהות. אי לכך, ניתן להתייחס אל מערכת זו כאל גלאי הדור הבא של גלאי PFNTS, היות והיא עדיפה על הגלאים הקודמים בכל הקריטריונים החשובים.

עבודה זו מתארת מספר סבבי פיתוח, בנייה ובדיקה של הגלאי, תוך שימוש בפולסים של נויטרונים מהירים (אשר נוצרו, בין היתר, מהתגובה ^{9}Be(d,n) עם קרן דויטרונים פועמת בפולסים של 1 ns~, ובתדר של MHz 1-2).

הנושא המרכזי של עבודה זו עסק בקביעת הגורמים המשפיעים ביותר על כושר ההפרדה המרחבית והזמנית של TRION. להלן פירוט הגורמים: סוג המסך, תגובת המערכת האופטית ומקורות הרעש השונים אשר המערכת רגישה להם. בהקשר זה, תשומת לב מיוחדת ניתנה לבדיקות הבאות:

א. נערכה השוואה בין מסך נצנץ המורכב מסיבים לבין מסכי נצנץ מונוליתיים בעוביים שונים, אשר בדקה תפוקת אור ו- *Contrast-Transfer Function* (*CTF*). בנוסף, תלות הרזולוציה המרחבית באנרגיית הנויטרון נבדקה בעזרת סימולציה וניסוי.
ב. נמדד תפקודה של TRION מההיבט האופטי הטהור, ללא השפעת נויטרונים, והושווה לתפקוד הכללי. השפעתו של ה- image intensifier (I-I) על ה- CTF בודדה ונחקרה באופן שיטתי, כולל השלכותיו על התנהגות ה- variance/pixel אשר אופיינה בעזרת מודל והושוותה לערכים מדודים.

ג. כושר ההפרדה הזמני (המגדיר את כושר ההפרדה האנרגטי של הנויטרונים) משפיע באופן ישיר על מידת הניגודיות (contrast) בין נויטרונים "רזוננטיים" ל"ללא רזוננטיים". כחלק מהניסויים אשר בוצעו לבחינת ספקטרומטריית זמן-המעוף באמצעות TRION, הראינו כי כושר ההפרדה הזמני מוגבל ע"י זמן הפתיחה המינימלי של ה-I-I וזמן הדעיכה של הנצנץ. למרות פגיעה מסויימת בכושר ההפרדה המרחבי ע"י ה- I-I ומקורות רעש דומיננטיים כגון *photon shot noise* ורעש תרמי מה-I-I, הושג כושר הפרדה מרחבי מצוין (תת-מילימטרי).

ד. כניסוי מסכם, בוצעה רדיוגרפיה של מספר מוטות גרפיט, אשר הניבה לבסוף תמונת היטל של מפת הצפיפות השטחית של פחמן, באיכות חסרת תקדים בשיטה זו.

לסיכום, השיפורים אשר הוצגו ע"י TRION, בכושר ההפרדה המרחבי, ברגישות ליסודות ספציפיים ובעבודה בקצבי מנייה גבוהים (בהשוואה לגלאים אשר פותחו ע"י Oregon ו- Tensor), טומנים בחובם פוטנציאל כי גלאי זה יענה בסופו של דבר, על כל מאפייני הפעולה הדרושים לתרחישי סריקה בטחונית.

אוניברסיטת בן-גוריון בנגב
הפקולטה למדעי ההנדסה

המחלקה להנדסה גרעינית

ספקטרומטריה ודימות של נויטרונים מהירים באמצעות שיטת קריאה אופטית ממותגת

חיבור זה מהווה חלק מהדרישות לקבלת תואר מגיסטר בהנדסה

מאת: אילן מור

מנחים: ד״ר דוד ורצקי,מכון למחקר גרעיני נחל- שורק
ד״ר איציק אוריון, אוניברסיטת בן-גוריון

חתימת המחבר..... תאריך.....

אישור המנחה/ים..... תאריך.....

..... תאריך.....

אישור יו״ר ועדת תואר שני מחלקתית..... תאריך.....

מרץ 2006